MECHANOBIOLOGICAL REGULATION OF EARLY STAGE BONE REPAIR

A Dissertation
Presented to
The Academic Faculty

by

Brett S. Klosterhoff

In Partial Fulfillment
of the Requirements for the Degree
Doctor of Philosophy in Bioengineering

Georgia Institute of Technology
August 2019

MECHANOBIOLOGICAL REGULATION OF EARLY STAGE BONE REPAIR

Approved by:

Dr. Robert E. Guldberg, Advisor
School of Mechanical Engineering
Georgia Institute of Technology

Dr. Nick J. Willett, Advisor
School of Medicine
Emory University

Dr. Jeffrey A. Weiss
School of Biomedical Engineering
University of Utah

Dr. Keat Ghee Ong
School of Biomedical Engineering
Michigan Technological University

Dr. Scott J. Hollister
School of Biomedical Engineering
Georgia Institute of Technology

Dr. Edward A. Botchwey
School of Biomedical Engineering
Georgia Institute of Technology

Date Approved: June 25, 2019

To Glenn Smith, who always told me I should learn Ohm's law.

You were right, Grandpa.

ACKNOWLEDGEMENTS

I am amazed by the number of talented, inquisitive, and kind people that my graduate experience has allowed me to learn from and work alongside. I want to express my sincere gratitude to each of you.

First, I am grateful for the mentorship I have received from my advisors, Bob Guldberg and Nick Willett, which has extended far beyond scientific research. Thank you for building an environment of intellectual freedom, and for challenging me to articulate my small contributions to the field as a whole. I thank Bob for seeing something in me that I must admit I rarely do. There were many days I left Bob's office after presenting failed experiments that I felt renewed confidence to persist in my ideas. I thank Nick for invariably reminding me that research is a non-linear phenomenon, and for always recognizing small victories, even when I did not want to. Though you both gave me complete ownership of my research, I never felt like I was working alone.

I thank each of my committee members for the expert perspective they have generously contributed to this work. I thank Keat Ghee Ong, who personally spent many late nights with me in lab teaching me the fundamentals of sensor fabrication, characterization, and most importantly, troubleshooting. This project would have never left the ground without your expertise and enthusiasm to share it. I must also thank Ghee's students and my collaborators, Brad Nelson and Salil Sidharthan Karipott, whose wireless telemetry has underpinned a great deal of this research. I also thank Jeff Weiss, Ed Botchwey, and Scott Hollister for constructively engaging with this thesis every step of the way. You have all been instrumental in improving the quality of this work.

Many thanks to all of the members of the Guldberg and Willett Labs, whose enthusiasm and friendship have made graduate school far more enjoyable. It is remarkable how many research challenges encountered along the way were eased by the shared knowledge of lab mates. In particular, I would like to thank Angela Lin, Laxmi Krishnan, and Hazel Stevens for the guidance and training you provided when I first joined the lab. In hindsight, each of you tolerated astoundingly naïve questions from me for several years without batting an eye. Thank you for making me feel like I belonged in the lab when I was struggling the hardest, and for reminding me that I was learning the most during those tough times. Thanks also to Marissa Ruehle, who navigated graduate school with me, helped with vascular perfusions, and provided mutual support during the final push to graduation. Thanks to Jarred Kaiser for partnering on finite element analyses, and to Casey Vantucci for assistance with immune characterization. I also thank everyone else who has resided in The Lair, even the notorious Andrés Garcia Lab, for making our windowless office a collaborative place.

I would also like to thank the Vertera and NuVasive teams for giving me the opportunity to work in an exhilarating environment that significantly complimented my graduate experience. In particular, I'd like to thank Chris Lee, Stephen Laffoon, Allen Chang, Mateo Garcia, Ken Gall, Dave Safranski, Kurt Jacobus, and Ryan O'Flaherty for treating me as a colleague, generously answering my questions, and entrusting me with challenging work from day one. I am especially grateful for the encouragement Stephen, Allen, Mateo, Ryan, and the rest of the development team gave me to finish my "book report."

I must also recognize the outstanding IBB staff who have helped me along the way. I thank Dr. Laura O'Farrell and Dr. Richard Noel for providing thoughtful advice while I developed the in vivo model for this project. I thank Ogeda, Altair, Andrea, Brittany, Josh, and the rest of the PRL staff for always ensuring our animals received the absolute best care, and for accommodating my extensive requests when preparing for surgeries. I also gratefully acknowledge my academic advisor, Laura Paige, who fixed each of the numerous administrative errors I made throughout graduate school.

I would also like to take this opportunity to thank my entire family, who have provided me with love, support, and the opportunities to succeed. Thanks to Mom, for teaching me the value of a deep curiosity and an absolute refusal to quit. Thanks to Dad, for teaching me that working hard on something you are passionate about is among the greatest joys in life. Thanks to Meg, for never letting me take myself too seriously. Thanks to Scott and Diane, for welcoming me into your family during this period. Thanks to Kelly, Aaron, Ryan, Lily, and Marci, for making Atlanta feel more like home.

Finally, and mostly, I thank my wife and inspiration, Kayla. You have sacrificed so much to allow me to pursue this dream. I am so grateful for your love. Your spirit moves me each day.

TABLE OF CONTENTS

LIST OF TABLES

LIST OF FIGURES

LIST OF SYMBOLS AND ABBREVIATIONS

2D	Two-dimensional
3D	Three-dimensional
ALP	Alkaline phosphatase
ANOVA	Analysis of variance
AWG	American wire gage
BLE	Bluetooth low-energy
BMP	Bone morphogenetic protein
Col I	Type I collagen
COX-2	Cyclooxygenase 2
D-PLSER	Discriminant partial least squares regression
ECM	Extracellular matrix
ERK	Extracellular signal-related kinsases
FE	Finite element
H&E	Hematoxylin & eosin
HIF-1α	Hypoxia inducible factor alpha

HP	Hydrostatic pressure
IL-1	Interleukin 1
IL-4	Interleukin 4
IL-6	Interleukin 6
LIX (CXCL5)	Lipopolysaccharide-inducible CXC chemokine (C-X-C motif chemokine 5)
LV	Latent variable
M-CSF	Macrophage colony-stimulating factor
MCU	Microcontroller unit
MEMS	Microelectromechanical systems
MSC	Mesenchymal stromal cell
NSAIDS	Non-steroidal anti-inflammatory drugs
OC	Osteocalcin
OFF	Oscillatory fluid flow
PCA	Principal component analysis
PCL	Polycaprolactone
PI3K	Phosphoinositide 3-kinase

PSU	Polysulfone
p38	p38 mitogen-activated protein kinases
RGD	Arginylglycylaspartic acid
RNA	Ribonucleic acid
SA-CAT	Stretch-activated transmembrane cation channel
TNF-α	Tumor necrosis factor alpha
RANK-L	Receptor activator of nuclear factor kappa-B ligand
RANTES (CCL5)	Regulated on activation normal T cell expressed and secreted (C-C motif ligand 5)
RUNX2	Runt-related transcription factor 2
UHMWPE	Ultra-high molecular weight polyethylene
USB	Universal serial bus
VEGF	Vascular endothelial growth factor
VIF	Variance inflation factor
VOI	Volume of interest

SUMMARY

Each year in the United States alone, several hundred thousand people suffer skeletal fractures that do not heal from the original treatment, resulting in non-union. Patients with non-unions are afflicted with prolonged disability and often undergo multiple costly surgeries. To improve patient outcomes, there is a clinical need for therapeutic strategies that mitigate non-union risk by stimulating bone repair. As the primary load-bearing tissue, the skeleton dynamically adapts its structure and composition to mechanical loads, and controlled loading via rehabilitation represents a non-pharmacologic target with the potential to stimulate endogenous bone regeneration mechanisms. Prior research has demonstrated that the adaptive response of healing tissue to mechanical cues are magnitude dependent, where moderate mechanical loading potently enhances osteogenesis, but excessive loading promotes fibrosis and non-union. However, the study of mechanobiology in vivo has largely remained qualitative and these thresholds are not well defined largely because the temporal progression of mechanical conditions during dynamic activities like walking and exercise cannot be measured accurately. This technical limitation hinders the ability of researchers to investigate skeletal mechanobiology and exploit it for therapeutic purposes.

The primary objectives of this thesis were to develop technical approaches to longitudinally monitor dynamic mechanical cues during bone healing and elucidate how specific magnitudes promote repair. Our overall hypothesis was that moderate mechanical stimulation exerted via periodic ambulatory activity could enhance bone regeneration. To test this hypothesis, we engineered a fully implantable wireless strain sensor platform that

enabled real-time non-invasive monitoring of mechanical cues in a pre-clinical model of skeletal repair. We used the sensor platform and image-based finite element analyses to quantify the progression of tissue-level mechanical cues during gait under varying degrees of load sharing. We discovered that early-stage strain magnitudes correlated with significantly improved healing outcomes, where tissue-level compressive strains of 2-7% imparted by moderate stiffness fixation tripled the defect bridging rate and enhanced bone formation by 60% relative to traditional higher stiffness fixation. Mechanical load sharing enhanced bone repair by promoting a mechanistic shift from primarily intramembranous toward endochondral ossification. Furthermore, strain magnitudes at later time points correlated with the status of healing, demonstrating feasibility of strain sensing techniques as an X-ray-free healing assessment. Remarkably, we also observed that osteogenic mechanical loading exerted substantial previously unexplored effects on early stage biological processes that precede mineralization, including immune cytokine signaling and angiogenesis. Load-shielded defects exhibited increased VEGF expression and vascular volume at intermediate healing time points, while immune cytokines associated with cellular recruitment, acute inflammation, and matrix synthesis were elevated by mechanical loading. These results suggest the immune response after skeletal injury is mechanosensitive and can be modulated by early mechanical loading to coordinate enhanced bone repair.

At the conclusion of the experiments, we attained a deeper understanding of how specific mechanical cues regulate bone repair in vivo, and established a novel sensor platform to further investigate mechanobiology. The knowledge gained by this thesis aids the development of integrative therapeutic strategies that stimulate bone repair via

functional rehabilitation. In addition, the technological outcomes of this thesis serve as foundational support for the expanded development of implantable medical sensor technologies with broad implications to enhance diagnostics, therapeutic development, and interventional surveillance.

CHAPTER 1. INTRODUCTION

Among the critical factors that modulate tissue regeneration, physical forces are transduced into chemical signals governing essential biological processes in almost all cells. In particular, skeletal development and healing processes are highly sensitive to mechanical cues imposed by functional load-bearing activity. Elucidating the complex regulatory role of mechanical stimuli is critical to understand bone development, homeostasis, and pathology, and could aid the development of new treatment strategies for pervasive skeletal injuries such as fractures.

Motivated by the mechanosensitive nature of bone, load-sharing interventions intended to augment bone formation have received significant clinical interest, including reduced stiffness implants, dynamic compression plating, and external fixator devices with actuating capabilities. However, the local biomechanical conditions permitted by such systems are rarely quantified. Furthermore, the basic regulatory role of mechanical cues at critical early time points in healing prior to the establishment of mineralized bridging or non-union is poorly understood. This lack of fundamental understanding of basic mechanobiology, along with an absence of technical capabilities to quantify in vivo mechanical cues, represent major barriers to the development of safe and efficacious mechanical therapies. The overall objective of this thesis was to address these limitations by developing a wireless implantable strain sensor platform to acquire local measurements of functional mechanical cues throughout bone repair. The hypothesis was that early mechanical stimulation regulated bone repair, and that sensor readings would provide a quantitative understanding of osteogenic tissue-level mechanical cues.

We tested this hypothesis through the following three specific aims:

1.1 Specific Aim I: Engineer an implantable, wireless sensor to remotely measure dynamic mechanical strain across a bone defect in vivo.

To remotely quantify strain across the healing tissue in real-time, we engineered a custom internal fixation plate with an integrated strain sensor for a pre-clinical rodent model of bone repair. The objective of this aim was to evaluate the capability of the device to interrogate mechanical strain across healing bone defects during functional loading. We hypothesized that the device will have sufficient sensitivity to detect functional strains during ambulation, enabling the in vivo mechanical environment to be quantified in real-time.

1.2 Specific Aim II: Longitudinally evaluate relationships between mechanical boundary conditions, tissue-level mechanical cues, and functional bone repair.

The generally accepted paradigm is that moderate mechanical loading has the potential to augment bone repair, while excessive loading can abrogate mineralization and result in fibrotic non-union, but osteogenic early-stage mechanical stimulation are not well quantified. The objective of this aim was to perturb the mechanical environment using instrumented internal fixators of varying stiffness to investigate relationships between the temporal progression of mechanical cues during rehabilitative ambulation and bone defect repair. We hypothesized that a moderate increase in ambulatory load sharing conferred by reduced stiffness fixation would increase mechanical stimuli initially, and that the elevated deformation would eventually decrease due to enhanced bone formation.

1.3 Specific Aim III: Evaluate the biological effects of mechanical boundary conditions on early stage bone repair.

Little is known regarding the early stage biological response to functional mechanical loading. In this aim, we investigated differential responses during the early stages of bone repair preceding the healing outcome of bridging or non-union. The objective of this aim was to characterize early-stage molecular, cellular, and tissue-level composition in bone defects under models utilizing protein analysis, histology, and microCT imaging of vascular formation. We hypothesized that early-stage mechanical cues alter neovascular growth and immune cytokine secretion.

IMPACT

This thesis contributed a novel sensor platform enabling non-invasive measurements of strain in vivo and enriched fundamental understanding of how mechanical cues regulate critical biological aspects of early stage bone repair.

CHAPTER 2. BACKGROUND

2.1 Fracture and Non-Union Epidemiology

Bone defects as a result of traumatic injury, tumor resection, and congenital or degenerative anatomical deformities are among the most common injuries requiring surgery faced by the global healthcare system[1]. In the United States alone, it is estimated that 12 million fractures occur each year[2]. A substantial number of these fractures require orthopaedic surgery to stabilize the injury. Of the 3.4 million orthopaedic surgical procedures reported in 2005, approximately 615,000 were undertaken to repair fractures and dislocations[1]. Bone tissue possesses remarkable intrinsic regenerative capabilities, and the majority of fracture cases are healed by standard surgical techniques, mainly to reduce and stabilize the fracture site and allow endogenous healing to restore skeletal function within 3-6 months. However, a significant number of fractures do not heal spontaneously and result in non-union. A recent epidemiological survey of 309,990 fractures occurring in 2011 reported a non-union rate of 4.9%[3]. Comorbidities and patient-specific risk factors play a key role in the development of non-union. The risk factors associated with the establishment of non-union are multi-factorial, but multiple concurrent fractures, nonsteroidal anti-inflammatory drugs (NSAIDs) plus opioid use, open fracture, anticoagulant use, and osteoarthritis with rheumatoid arthritis were all observed to increase the risk of non-union development by over 50% for 18 different bones[3]. High energy injury, smoking, and diabetes have also been implicated to hinder bone repair and increase risk of non-union, but the mechanistic basis underlying these comorbidities remains poorly understood[4].

Regardless of the specific injury circumstances, the implications once non-union is established to the patient, healthcare system, and society as a whole are debilitating[4–7]. Analyses of clinics in the United States, Canada, and United Kingdom between 1997 and 2006 have estimated that direct medical costs to treat established non-unions range between $11,000 and $36,000[7–10]. The timeline to restore function after non-union is particularly lengthy, often taking many months or even years and typically involving multiple surgeries[11–13]. Furthermore, indirect costs due to prolonged patient disability are actually estimated to exceed the direct cost of care. Assessments of productivity loss during treatment of established tibial non-unions indicate that indirect costs account for anywhere from 67-93% of total costs[6]. In consideration of the scope and severity of fracture non-unions, it is critical that new therapeutic and rehabilitative strategies are developed to improve outcomes for fracture repair, thereby reducing prolonged healthcare costs and improving patient quality of life.

2.2 Bone Repair Physiology

Bone possesses an extraordinary capacity for endogenous healing. It is typically able to recover biomechanical competence after injury through a coordinated healing response. The progression of bone regeneration is a transient and spatially heterogeneous process characterized by rapid morphogenesis of numerous tissue phenotypes over days, weeks and months after the initial insult. In the case of critically-sized defects or extensive comorbidities, the intrinsic regenerative potential of the native tissue is insufficient to completely heal the injury. Thus, effectively designed clinical interventions must leverage stages of the bone healing process to enhance either bridging of the defect or surface integration with the surrogate implant to form a mechanically competent composite

structure. This dynamic regenerative process is commonly delineated into four major phases (and associated timelines) of tissue formation: (1) inflammation and hematoma (hours and days) (2) soft callus (days and weeks) (3) immature bone (weeks and months) (4) and bone remodeling (months and years) as depicted in Figure 1[14]. However, it should be noted that spatiotemporal variability is common in the healing of large bone defects, and different phases occur simultaneously within a fracture zone as dictated by the local biophysical and biochemical conditions of the cellular niche. In this section, the characteristic physiology of bone regeneration will be reviewed, and the critical regulatory role of biomechanics on tissue differentiation, neovascularization and inflammation will be reviewed.

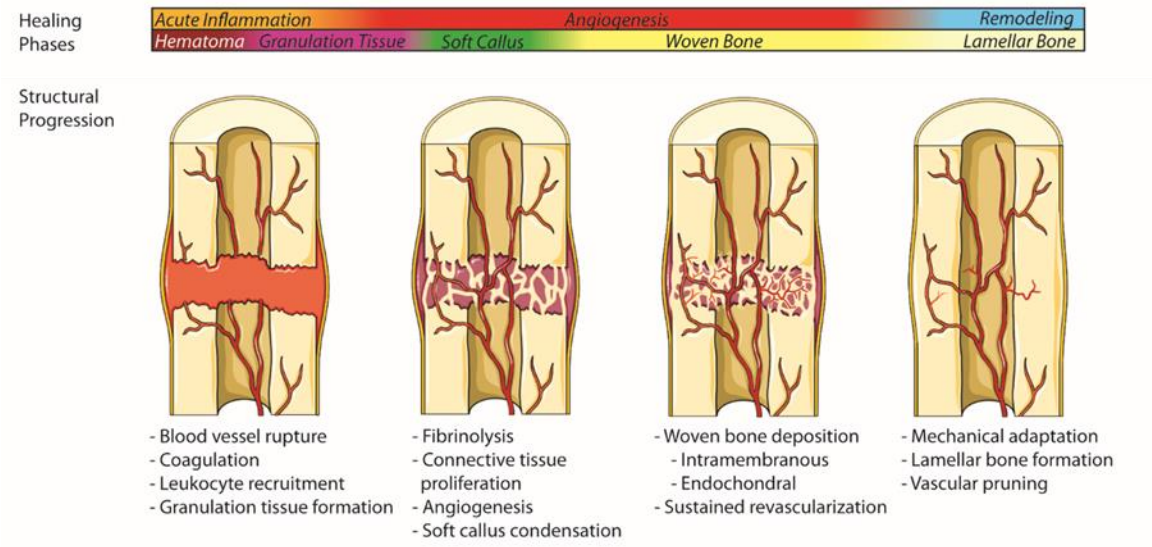

Figure 1: Phases of bone repair

2.2.1 Inflammation and Hematoma

Whether a defect is created by a controlled surgical technique or due to a traumatic injury, the fracture inflicts damage on cells of the bone, periosteum and neighboring

tissues, including rupture of surrounding vasculature. Tissue destruction initiates a cascade of acute inflammatory signals which mark the beginning of the regenerative process[15,16]. Disruption of nearby blood vessels quickly floods the defect zone with clotting blood and results in the formation of a hematoma. Interrupted circulation results in localized hypoxia, and the hematoma is characterized by low oxygen tension, acidic pH and high lactate concentration[17]. The hematoma is also rich with neutrophils, macrophages and other immune cells found in the peripheral blood supply as well as the bone marrow of long bones[16,18]. The inflammatory signals facilitate coagulation in response to hypoxia and concurrently activate this dense population of immune cells to secrete important molecular factors which mediate early stages of necrotic tissue clearance, extracellular matrix (ECM) production of granulation tissue, angiogenesis and mesenchymal stromal cell (MSC) recruitment[17]. Critical signaling molecules within the early hematoma include inflammatory cytokines like tumor necrosis factor alpha (TNF-α), interleukins 1 and 6 (IL-1 and IL-6), macrophage colony-stimulating factor (M-CSF), receptor activator of nuclear factor κB ligand (RANKL), and the enzyme cyclooxygenase-2 (COX-2)[19,20]. Expression of osteoinductive bone morphogenetic protein (BMP) family members as well as proangiogenic factors including hypoxia-inducible factor alpha (HIF-1α) and its downstream partner vascular endothelial growth factor (VEGF) are also upregulated in the fracture hematoma[17,21]. Underscoring its vital role as the foundational scaffold for fracture healing, removal of the hematoma delays fracture repair, while excision and subcutaneous implantation of the hematoma elicits ectopic bone formation[22,23].

While an initial inflammatory response is critical to successful bone regeneration, excessive or chronic inflammation counteracts the aforementioned beneficial aspects and

can attenuate healing[15]. In traumatic injuries which result in open fractures or composite tissue trauma, associated surges in systemic inflammation are thought to inhibit bone formation and increase the risk of reoperation[24]. Biomechanical conditions are also influential on the degree of magnitude and duration of inflammation in the defect zone. Relatively large magnitude mechanical strain within the hematoma as a result of poor implant stability or flexible fixation increases and prolongs the presence of cytotoxic immune cells and ultimately leads to delayed healing or nonunion[16,25,26]. The threshold delineating positive and negative levels of inflammation is multifactorial and thus difficult to define[15]. It is also important to note that the majority of available literature on early stages of bone healing is concentrated on simple transverse fractures, and the initial phase of large bone defect repair is not well characterized. Future research on the interplay between defect type, mechanical stability and patient comorbidities on early inflammation will greatly enhance the data available to develop personalized clinical strategies for healing more complex bone defect injuries.

2.2.2 Soft Callus and Neovascularization

As peripheral cells from the circulation, periosteum, surrounding tissue, and bone marrow begin to infiltrate the hematoma, a soft callus of granulation tissue is formed. The granulation tissue primarily consists of an immature fibrous matrix. Neovascularization of the granulation tissue is promoted by local diffusion of hypoxic paracrine factors. Nascent vessel formation proceeds through vasculogenesis, in which immature angioblasts form de novo primitive vessels, and angiogenesis, where the preexisting intact vasculature sprouts, branches and remodels to extend the functional vessel network[27]. Angiogenesis after injury is mediated by endothelial cells residing on intact blood vessels that degrade their

surrounding ECM and sprout in response to chemotactic gradients of angiogenic cues including VEGF, forming a motile tip extending from the vessel[28,29]. This tip cell migrates and extends into the injury site guided by paracrine biochemical and biophysical cues while adjacent stalk cells proliferate behind, forming the proximal branch of the nascent vessel[30]. Maturation of an angiogenic sprout into a functional blood vessel occurs by abluminal pericyte and vascular smooth muscle cell (VSMC) attachment to stabilize the sprout, lumen formation and perfusion, and anastomosis with surrounding tip cells[30]. Sprouts that do not stabilize or perfuse retract or undergo endothelial apoptosis[31]. Increased arterial blood flow also occurs by radial growth of intact vessels, known as arteriogenesis[32]. Functional vascularization within the hematoma is crucial to deliver oxygen and nutrients for MSC proliferation and maturation, and for waste removal. HIF-1α induced VEGF expression is the most well characterized molecular pathway stimulating angiogenesis into the defect space. Inhibition of VEGF reduced callus vascularization and impaired bone healing in the mouse, while administration of VEGF enhanced mineralized callus volume in a critically-sized rabbit defect model[33].

Unsurprisingly, new vessel growth is highly dependent on biomechanical boundary conditions imposed on the regenerating tissue in vivo. In a rodent critically-sized segmental defect model, uniaxial compressive load transfer at the onset of injury dramatically attenuated vessel ingrowth and connectivity within the defect zone, resulting in nonunion. Interestingly, compressive loading after initial stabilization of the defect by bridging with immature mineralized tissue reduced vascular connectivity but increased vascular thickness and bone volume, indicating that mechanical loading may disrupt small vessels while stimulating arteriogenesis of large vessels and deposition of new bone[34]. The specific

influences of mechanics on vascular ingrowth will be discussed in greater detail in Section 2.3.

2.2.3 Woven Bone Formation

Increases in local oxygen tension and pH buffering due to capillary infiltration within the granulation tissue-filled callus coincide with differentiation of recruited MSC's into osteogenic and chondrogenic phenotypes[35–37]. As MSC's mature, mineralization of the callus occurs primarily through two mechanisms: intramembranous (primary) or endochondral (secondary) ossification. Intramembranous ossification takes place by direct deposition and mineralization of osteoid matrix along a front propagating from peripheral intact bone. In endochondral ossification, a cartilage intermediary replaces the soft callus of granulation tissue before chondrocyte hypertrophy and mineralization occurs. Endochondral ossification proceeds over a longer time-scale than intramembranous ossification, and leverages the low oxygen demand of native cartilage better suited for avascular environments[38]. Thus, endochondral ossification is prevalent in callus regions which are slow to restore sufficient vascularization such as central portions of large bone defects[39].

The linkage of angiogenesis with osteogenesis is well demonstrated at the molecular scale, and their physiological roles cannot be decoupled[21,33]. VEGF expression and sufficient oxygen tension promotes chemotaxis of MSC's and subsequent adoption of an osteoblastic phenotype[40,41]. Likewise, BMP's -2, -4, and -6 promote differentiation of MSC's into osteoblasts, and these newly osteogenic cells simultaneously enhance secretion of VEGF in a differentiation-dependent fashion[42,43]. This osteogenic-angiogenic coupling

is hypothesized to promote paracrine signaling to nearby endothelial cells which support increased vascular capacity along newly-formed mineralization fronts.

Newly differentiated osteoblasts maintain sensitivity to local oxygen tension. Experimental evidence has demonstrated that Type I collagen (Col I) matrix synthesis, as well as osteocalcin (OC) and alkaline phosphatase (ALP) activity is suppressed in hypoxic conditions[44–46]. If deficient vascularization and hypoxia persist within the defect space, bone regeneration cannot occur regardless of the healing mechanism and nonunion will be established[33,47]. Stimulation of sufficient vascularization remains a critical obstacle to the successful treatment of large bone defects, open fractures and polytraumatic injuries[38,48].

Mechanobiological cues are known to direct the evolution of the fracture callus and ultimately the healing outcome of bone regeneration[49]. Highlighting the role of local mechanics on healing, both intramembranous and endochondral mechanisms of mineralization can occur simultaneously within a single healing defect as dictated by the mechanical conditions of the microenvironment[50]. In regions of high mechanical stability, intramembranous ossification is predominant, while larger magnitude strain typically stimulates endochondral ossification. Fibrocartilage, as well as connective and adipose tissue, is formed and tends to persist in regions of excessive strain and may lead to chronic nonunion.

2.2.4 Bone Remodeling

The transition of soft callus to immature, woven bone ensues by rapid deposition and mineralization of Type I collagen in a random, isotropic fashion[51]. This disorganized phenotype lacks the robust and spatially optimized mechanical characteristics of mature

lamellar bone, but is typically adequate to bear physiological loads due to hypertrophy of the woven bone callus. Structural homeostasis is restored by remodeling of the tissue micro- and macrostructure, which occurs over months and years after the original insult. Mechanically driven remodeling increases the alignment of the collagen matrix with principal loading directions and initiates resorption of mechanically superfluous ectopic bone[51]. In the diaphysis of long bones, reestablishment of the intramedullary canal and formation of bone marrow occurs over time.

Conversely, prolonged stress-shielding by supplementary fixation after the defect is bridged can slow mechanically driven remodeling[52,53]. In addition to fixation, the mechanical properties of any load-bearing implants (e.g. interbody fusion devices in spinal fusion procedures) are an important factor of long-term function even after defect bridging is achieved[54]. Sustained stress-shielding in very stiff implants has long been known to cause implant loosening and failure due to bone resorption at the implant-tissue interface. This effect is still an important challenge to longevity in load-bearing implants designed to remain in vivo for many years[55]. Thus, it is critical that both short and long-term mechanical conditions within the healed tissue are considered when selecting a bone defect treatment and rehabilitative approach.

2.3 Mechanobiological Considerations for Bone Repair

2.3.1 Cell-Level Mechanobiology of Bone Regeneration

Physical forces are transduced across length-scales into biochemical signals governing essential processes in almost all cells. MSC's possess a number of mechanosensory systems and their differentiation processes are exquisitely sensitive to

their micromechanical environment. Some of these critical physical factors include substrate stiffness, substrate topography, cell shape, and cell deformation resulting from interactions with the tissue matrix and surrounding fluids[56–58]. Similarly, mechanical strain and flow-induced shear is known to regulate growth and maturation of neovascular networks formed by endothelial cells[59–61]. These cellular-level phenomena have been demonstrated to correspond to tissue-level healing outcomes, as shown by numerous in vivo studies in the large bone defect and fracture healing literature investigating the role of specific mechanical signals on bone healing and maturation[34,49,62].

2.3.1.1 Cellular Mechanosensors

Mechanotransduction is the process by which cells sense and respond to physical forces exerted by their surroundings. This process is generally classified to occur in four major steps: (1) sensing of the mechanical stimulus, (2) conversion of the mechanical stimulus into a biochemical signal, (3) transmission of the biochemical signal, and (4) response of the effector cell[63]. Nearly all cells possess multiple mechanotransduction mechanisms known to regulate cell proliferation, differentiation, factor secretion and matrix synthesis. The molecular intricacies of each step in these mechanotransduction processes are beyond the scope of this text. For the purposes of this chapter, we provide a basic outline of (1) how cells sense force and (2) the functional roles of specific biophysical cues and substrate properties on cells as it pertains to skeletal repair.

To date, there are four known major mechanosensitive transmembrane components expressed in numerous cell types, including MSC's, bone cells, and endothelial cells, which alter cell function in response to physical interactions with their environment:

integrins, cadherins, stretch-activated ion channels and the primary cilia[64]. Transmembrane integrin cell adhesion receptors are the primary receptor linking type I collagen, fibronectin and laminin fibers of the local ECM to actin filaments of the cytoskeleton[65,66]. The specialized sites in the cytoskeleton at which integrin receptors form clusters are known as focal adhesion complexes. When ECM proteins bind to the integrin dimer, a subunit of the integrin within the cytoplasm undergoes a conformational change[67]. Since integrins do not have inherent enzymatic activity, the conformational change in the cytoplasmic domain transduces extracellular signals to regulate intracellular biochemical activity via kinases docked at the focal adhesion complex[68]. Mechanical stresses and strains on the ECM are also transmitted directly to the actin cytoskeleton of adhered cells via integrin binding sites. Conversely, cells exert traction forces and remodel their respective substrate via integrins[69]. In this manner, integrin complexes are the primary mechanism by which deformation and force is transferred bidirectionally between a cell and its substrate.

Cadherin receptors are the primary transmembrane component cells utilize to transmit traction forces and deformation to neighboring cells. Cell-cell connections formed at cadherin receptors are also anchored to the intracellular cytoskeleton by protein complexes including vinculin, α-catenin and β-catenin which regulate important downstream cell functions including differentiation, proliferation and apoptosis[70]. Observations of highly localized strain concentration at cadherin-linked adherens junctions between endothelial cells subjected to flow-induced shear have led researchers to hypothesize that their structure is designed to target and amplify mechanical signals on cellular interfaces, increasing communication of mechanical signals between neighboring cells[71,72].

Stretch-activated transmembrane cation channels (SA-CAT's) are gated by tension generated within the cytoskeleton acting along the plane of the cell membrane[73]. These non-selective mechanosensitive channels have been found in numerous cell types including endothelial cells and osteoblasts[74–76]. They respond to the magnitude and frequency of membrane deformation induced by changes in hydrostatic pressure by increasing channel open probability in response to larger or more frequent mechanical stimuli[74,77].

Primary cilia are immotile organelles formed by microtubules running from the centrosome and protruding 4-6 μm above the apical cell membrane surface. The cilia of osteoblasts deflect due to fluid flow-induced shear stress, and mice with bone-specific primary cilia knockouts exhibit reduced load-induced bone formation[78,79]. In human MSC's subjected to oscillatory fluid flow, removing expression of primary cilia with small-interfering RNA inhibits flow-induced osteogenic gene expression, confirming their role in flow mechanotransduction[80]. However, the precise signaling mechanisms mediating this response are not well characterized. One hypothesis cites that integrin focal adhesion complexes are known to localize at the same locations as primary cilium in several cell types including chondrocytes[81]. Thus, the cilia might signal interdependently with integrin to alter cell function and phenotype in response to fluid-mediated shear independent of cell substrate deformation[80]. Interestingly, cilia on endothelial cells are only found in regions of low or disturbed flow and they disassemble in response to laminar flow, but their role in cell function remains unclear[82,83].

Cells utilize their intrinsic mechanosensitive components to regulate their function based on feedback from the local environment, and conversely they also remodel their surroundings through these same mechanisms. This two-way mechanical communication

is a critical process underlying tissue-level growth and development during healing. Through in vitro studies, specific substrate properties and extrinsic mechanical stimuli acting at the micro- and nanoscale have been elucidated as controllers of cell migration, lineage, proliferation and protein synthesis. Physical mechanisms known to direct cell behavior include substrate stiffness, substrate topography and shape, substrate deformation, fluid flow-induced shear, and hydrostatic pressure.

2.3.1.2 Intrinsic Physical Cues

Cells in vivo inhabit a vast range of tissues, each with different degrees of elasticity and stiffnesses. Cells that adhere to an underlying substrate form focal adhesion complexes and exert contractile forces, creating tension in the actin cytoskeleton and local deformation of the bound substrate[84]. The mechanical stiffness of this substrate is known to have a direct effect on cell behaviors including migration, proliferation, apoptosis and differentiation[56]. Vincent et al. fabricated gels with stiffness gradients encompassing the majority of soft tissues (1-12 kPa) and observed that MSC's preferentially migrated to the region with the highest stiffness with a migration rate proportional to the gradient slope[85]. Increasing the stiffness of the underlying cell substrate has also been shown to promote cell proliferation and to decrease the rate of apoptosis in fibroblasts and endothelial cells[86–89].

The influence of substrate mechanical properties on stem cell differentiation is of particular importance for bone regeneration, where MSC's serve as the primary source for skeletal tissue growth and differentiation. One of the first studies to isolate the role of substrate stiffness on MSC lineage showed that cells cultured on polyacrylamide gels possessing a modulus similar to un-mineralized osteoid matrix (25-40 kPa) adopted an

osteogenic morphology and produced osteogenic gene and protein profiles, while cells seeded on more compliant substrates mimicking neurogenic and myogenic environments assumed neurogenic and myogenic phenotypes, respectively[58]. While the preceding experiment was conducted in a two-dimensional (2D) culture environment, osteogenic commitment has also been replicated by Huebsch and colleagues in three-dimensional (3D) culture with mouse MSC's encapsulated in gels of approximately 11-30 kPa[90]. However, MSC's in 3D did not exhibit the drastic change in morphology as observed in 2D monolayer conditions. Interestingly, cells encapsulated in an even stiffer gel of approximately 110 kPa showed a drop-off in the production of osteogenic markers compared to cells within the 11-30 kPa gel. They demonstrated that integrin binding and the formation of tension-generating traction forces within the actin cytoskeleton are directly proportional to the rigidity of the substrate and mediate this process of stiffness-dependent osteogenesis, as blocking cell contractility with (2,3)-butanedione-monoxime prevents lineage commitment[90].

The surface topography of a cell's substrate controls the spatial distribution of internal cytoskeletal stresses by altering the cell shape as well as the density of integrin and cadherin mediated traction forces formed with the surroundings. Consequently, intracellular mechanical signaling transmitted through the actin cytoskeleton is altered. Human endothelial cells cultured on microstructural features such as square islands and asymmetric annuluses (on the order of hundreds of μm's) created asymmetric stress distributions, and cells in regions of high local stress concentrations proliferated faster than neighboring cells in low stress regions[91]. Dalby and colleagues observed that nano-textured surfaces with equally-spaced pit features 120 nm in diameter and 100 nm deep inhibits

formation of focal adhesions and prevents osteogenic differentiation in human MSC's[92]. Interestingly, when the identical pit feature was distributed in a random pattern more representative of nanoscale disorder seen in native tissue, cells adopted osteoblastic morphology and produced early markers of osteogenic differentiation measured at 14 and 21 days[92].

In 3D microenvironments seen in vivo, there is a complex interplay between substrate architecture, cell shape and cytoskeletal stress distribution, making it difficult to elucidate their relative importance[93]. Khetan and colleagues attempted to decouple the role of cell shape and cell-mediated tractions by encapsulating human MSC's in degradable hyaluronic acid hydrogels that promoted cell spreading, formation of focal adhesions and osteogenic differentiation[94]. Secondary cross-linkers were added after one week of culture which effectively halted further degradation of the hydrogel and inhibited cell-substrate tractions while the cells were still in a spread morphology. In response, cells switched from osteogenic to adipogenic differentiation without significantly altering their shape, indicating that cell adhesion-mediated traction forces with the matrix are more potent regulators of stem cell fate than shape alone[94].

2.3.1.3 Extrinsic Physical Cues

In load-bearing organs like bones, the tissue is subjected to complex spatiotemporal patterns of force and deformation. Stress and strain of the tissue by external biomechanical loads is transferred to cells and microvasculature primarily in the form of compressive and tensile mechanical strains of the underlying matrix, interstitial fluid flow-induced shear stress and hydrostatic pressure.

Cytoskeletal tensile strain can be transmitted to a cell by stretch of the underlying ECM and is known to affect MSC phenotype. However, the role of strain in osteogenesis has not been fully elucidated, as independent studies have shown that tension can induce upregulation of bone[95–97], muscle[98] and fibrous[99,100] tissue markers in MSC's. Sumanasinghe et al. found that human MSC's cultured in 3D collagen matrices subjected to daily bouts of cyclic 10% uniaxial strain for 7 days or 14 days upregulated BMP-2 mRNA expression, while unstrained cells did not[95]. Kearney and colleagues subjected rat MSC's cultured on a type I collagen-coated silicone substrate to 2.5% uniaxial cyclic tensile strain for 14 days and observed reduced MSC proliferation and increased expression of osteogenic genes including core-biding factor alpha 1 (Cbfa1/Runx2), Col I, OC, and BMP-2[96]. Using biochemical inhibitors, they identified that SA-CAT's were required for increased Col I expression and that kinases ERK, p38 and PI3K each contribute to the observed increase in BMP-2. These findings indicate that multiple parallel signaling mechanisms mediate cellular responses to tension[96].

Tensile strain can also enhance MSC differentiation down other tissue lineages. Subramony and colleagues cultured human MSC's on poly(lactide-*co*-glycolide) nanofiber scaffolds with either aligned or unaligned fiber matrices and applied 1% cyclic tensile strain[99]. Differing from the findings of the previous studies, cells seeded on aligned matrices and subjected to tensile loading increased production of fibroblastic or tendon-related markers including Col I, Type III collagen (Col III) and tenascin-C after 14 and 28 days with no significant increases in osteogenic markers[99]. Chen et al. found that tensile strain can induce fibrogenesis or osteogenesis in human MSC's cultured on Col I-coated substrates in a strain magnitude-dependent fashion[101]. Cells exposed to 3% cyclic tensile

strain for a period of 8 hours increased expression of osteogenic genes. However, cells subjected to higher magnitude strains (10%) for 48 hours showed increased expression of tendon-related markers[101]. Jang and colleagues have also shown magnitude-dependence to tensile strain in rabbit MSC's on fibronectin-coated polydimethylsiloxane (PDMS) substrates[98]. Cells subjected to higher cyclic strains (10%) for 72 hours increased production of smooth-muscle markers while cells exposed to identical conditions but reduced (3%) strain expressed more osteogenic markers[98]. These findings support that relatively large magnitude, sustained tensile strains tend to promote fibroblastic or myogenic differentiation of MSC's, whereas lower magnitude or shorter duration tension supports osteogenic differentiation.

Compressive deformation of a 3D ECM creates a complex micromechanical environment which can result in direct strain of cells, increased hydrostatic pressure, and extracellular fluid flow[102]. The individual contribution of each type of mechanical perturbation is difficult to uncouple experimentally in 3D cultures which better replicate the in vivo niche. Nonetheless, several studies have found evidence that direct, unconfined compression of 3D hydrogels enhances chondrogenic differentiation of MSC's[103]. Huang and colleagues suspended rabbit MSC's in 2% agarose, with or without administration of the chondrogenic cytokine transforming growth factor-β1 (TGF-β1), and subjected the gels to daily sessions of 10% compressive strain[104]. They observed increased expression of chondrogenic markers collagen type II (Col II) and aggrecan in mechanically stimulated MSC's with no significant differences due to the administration of exogenous TGF-β1, indicating compressive strain is a chondrogenic stimulus independent of biochemical supplements *in vitro*[104]. Other studies of encapsulated MSC's have supported that exposure

to TGF-β1 or compressive loading are both chondrogenic, but instead have shown that TGF-β1 is a significantly more potent stimulus[105,106]. To better elucidate the intracellular mechanism facilitating compression-induced chondrogenesis, Pelaez et al. cultured human MSC's within a fibrin hydrogel with our without administration of an inhibitor of the ERK 1/2 pathway, a widely conserved signaling pathway modulated by integrin adhesion with the ECM[107,108]. Gels were dynamically compressed immediately followed by measurement of osteogenic and chondrogenic markers. They found that inhibition of the ERK 1/2 pathway abrogated the chondrogenic response observed in cells loaded without the inhibitor. Instead, blocking the ERK 1/2 pathway promoted osteogenic marker expression. Thus, it appears that dynamic compression-induced chondrogenesis or osteogenesis is in part regulated by activation of the ERK 1/2 pathway, thereby promoting cartilage formation[108]. Likewise, Steward and colleagues showed that integrin adhesion of MSC's with the ECM at least in part mediates chondrogenic differentiation in response to dynamic compression[109]. Based on these studies, it is clear that compressive stimuli regulate the differentiation profile, and particularly chondrogenesis, of MSC's.

Mechanical stretch due to hemodynamic forces have long been to known to regulate vascular structure and function[110]. Increasing evidence has also elucidated that stretch mediated by the external matrix or substrate influences the collective behavior of endothelial cells, capillaries and microvascular structures. Zheng et al. showed that rat and human endothelial cells seeded in 2D on Col I increased production of pro-angiogenic receptors in response to cyclic tensile strain[111]. Thus, mechanical stretch can increase endothelial cell sensitivity to paracrine VEGF signaling to promote vascular growth. Joung and colleagues cultured vascular endothelial cells in a 3D collagen gels subjected to cyclic

tensile stretch and observed that cord-like cellular structures formed perpendicular to the stretch direction[112].

To better understand the effect of micromechanical stimuli on multicellular structures with a 3D vascular morphology, Krishnan and colleagues cultured microvessel fragments within 3D rectangular collagen gels and subjected the constructs to four different mechanical boundary conditions: 6% static stretch, 6% cyclic stretch (1 Hz, 12 hours per day), unstretched but anchored, and free gel[60]. Each of the three anchored or stretched construct groups had significantly more vessels per construct compared to the free gel, indicating tension formed by external stretch and contraction of the gel enhanced microvascular growth. Interestingly, they found that the microvessel fragments in these same three groups preferentially oriented themselves parallel to the direction of stretch[60]. This seemingly contradictory result to cellular level studies may be due to enhanced contact guidance provided by the surrounding collagen matrix with the multicelluar microvessel fragments, since the ECM tends to align in the primary direction of stress[113]. Thus, the role of mechanical cues like matrix deformation in more geometrically complex models recapitulating in vivo tissue architecture can be drastically different than simpler systems. Strikingly little is known about the role of compressive strains on endothelial cells and the microvasculature, which is the primary stimulus induced by functional loading of bone defects. Future work to understand how compression or shear of the pericellular matrix influences neovascular growth is critical to inform novel approaches to improve vascularization in regenerative processes like bone repair.

As mentioned briefly, the application of cyclic external loads also induces oscillatory patterns of interstitial fluid flow away from regions of large compressive

deformation, like a sponge releasing water when squeezed[67]. This fluid flow exerts shear stress on the apical surface of adhered cells within the tissue, activating membrane mechanosensors like the primary cilia which in turn transduce the cytoskeleton[80]. Additionally, perfusion of the cells increases convective transport of nutrients throughout the ECM. Fluid-induced shear force on the cell surface is related to the magnitude and the velocity of the external load application, and is widely accepted as a principal extracellular stimulus regulating the maintenance and adaptation of native bone to biomechanical loads[63,70]. Fluid-flow induced shear is also a critical determinant of the function of MSC's. Meinel et al. showed that fluid flow increased calcium and ALP in human MSC's on collagen scaffolds, and that the degree of osteogenesis is dependent on the flow pattern (spinner flask or perfused reactor) and scaffold degradation rate[114]. Hoey et al. demonstrated that OFF-induced osteogenesis in MSC's is partially facilitated by the primary cilia[80]. Notably, inhibiting primary cilia formation significantly increased proliferation in the presence of flow, indicating cilia regulate the extent of cell proliferation in the presence of mechanical stimuli[80].

Similarly, external fluid shear stress is also known to effect the proliferation and migration of endothelial cells, although most research has focused on steady rather than oscillatory flow patterns. Ando and colleagues were the first to show that endothelial cell proliferation is significantly enhanced in proportion with the intensity of the applied shear stress[115]. Li et al. demonstrated that endothelial cells subjected to flow migrate in the direction of the flow stimulus by successively forming focal adhesions at the front of the cell and disassembling focal adhesions at the rear[116]. For bone tissue engineering, the benefits of fluid flow on osteogenic differentiation and endothelial proliferation and

migration is one advantage of highly interconnected porous architectures for graft substitutes[117]. OFF-induced osteogenesis has also been leveraged by in vitro scaffold preconditioning in perfusion bioreactor culture platforms[118].

Local changes in hydrostatic fluid pressure (HP) due to tissue deformation are also known to control MSC phenotype. Numerous *in vitro* studies of MSC in aggregate, pellet, and hydrogel-encapsulated cultures have established that cyclic HP enhances expression of chondrogenic genes, proteoglycans and collagen[119–121]. The mechanosensory mechanism mediating this response is unclear, though intracellular and extracellular ion transport is known to be responsive to changes in HP, suggesting a role for stretch-activated ion channels[122–125].

In vitro models have established that all cells, including MSC's and endothelial cells, are highly sensitive to physical interactions with their surroundings. These mechanobiological interactions regulate cellular processes critical to bone defect healing. The mechanical environment of a cell is primarily determined by intrinsic properties of the underlying substrate, the configuration of cell adhesions, and the external stresses and strains transmitted by the underlying substrate and interstitial fluids. During bone regeneration, devices like implants, scaffolds, and fixation equipment govern these physical factors, indicating that mechanical or architectural alterations could appreciably improve or impair healing outcomes. Thus, observations gleaned from these in vitro studies of cell mechanobiology motivate further investigation in more spatiotemporally complex, clinically relevant in vivo systems.

2.3.2 Tissue-Level Mechanobiology of Bone Regeneration

In vivo models of bone regeneration are critical to establish the relative importance of mechanical stimuli on functional healing outcomes. Numerous studies have explored the effects of different types of loading on fracture and large bone defect healing. However, the ability to experimentally measure local mechanical stresses and strains in vivo is challenging. The experimental framework to study mechanical stimulation of bone healing is not standardized, making it difficult to compare findings across different studies. Generally, researchers transfer mechanical loads through a bone defect by three methods: (1) using a defined loading protocol transmitted by an external fixation device (2) using fixation devices that allow different ranges of deformation (3) using fixation devices possessing different apparent stiffnesses[126]. The latter two techniques do not allow active control of the stress or strain exerted on the defect region, but do permit the use of internal fixation devices.

The vast majority of experimental data investigating mechanical stimulation on bone healing is for fracture, whereas the literature on large defect regeneration is more limited. The fracture healing literature has established that certain levels of early interfragmentary movement promote formation of an unmineralized callus and enhanced endochondral bone healing[50,127–130]. Increased callus formation can have a beneficial or detrimental effect on tissue growth and maturation, with a strong dependence on the magnitude, timing, and duration of the loading. Goodship and Kenwright were the first to show that controlled cyclic axial compression protocol initiated at day 0 (500 cycles/day, 33% maximum strain/360 N maximum load) in a sheep 3mm tibial osteotomy model enhanced initial callus formation, increased tibia axial stiffness at 8 in 10 weeks in vivo, and increased tibia torsional stiffness at 12 weeks ex vivo[127].

The post-operative timing of load transfer is also critical to the healing outcome. Late load transfer has been shown to enhance the rate of bone remodeling and maturation after defect bridging has occurred. Gardner observed that non-invasive cyclic compression (2 N peak load, 100 cycles per day) in a mouse tibial osteotomy from day 0 inhibited callus formation and ultimately prevented healing. Notably, a four day delay in compressive loading enhanced bone healing[131]. While these findings may appear contradictory to the prior reports of Goodship and Kenwright, an intramedullary nail with significantly reduced mechanical resistance to axial and torsional loads was used in the mouse model, highlighting the importance of fixation strategy. Multiple fracture and large bone defect models in the rat and mouse have also supported the functional healing benefit of increased load transfer at 3-4 weeks by utilizing a dynamic fixation system whose axial stiffness can be reduced at a given time point, permitting larger compressive loads through the tissue[34,52,62,132].

To elucidate the role of uniaxial compressive stimuli in a critically-sized 6 mm rodent femoral defect model, Boerckel and colleagues showed that load transfer at 4 weeks after initial mineral bridging significantly enhances bone volume at 8 weeks and torsional stiffness at 12 weeks when treated with a graft substitute consisting of an alginate hydrogel delivering 5 μg BMP-2 and a dynamic internal fixator[62]. Qualitative histological observation demonstrated that loaded defects had increased cartilage formation at 5 weeks and an isotropic collagen microstructure characteristic of woven bone at 12 weeks, demonstrating that the chondral and remodeling phases of healing is prolonged in mechanically stimulated large bone defects in a manner analogous to fracture healing. In a separate study, Boerckel et al. studied the effect of delayed mechanical loading on

neovascular growth in an 8 mm defect model and observed that compressive load transfer at 4 weeks increases the number of large diameter blood vessels exceeding 300 μm in diameter and reduces the number of small vessels less than 100 μm in diameter within and around the defect region[34]. From these data it was hypothesized that mechanical stimulation may rupture small vessels while concurrently enhancing arteriogenesis of larger vessels in and around the newly regenerated bone. Notably, immediate post-surgical load transfer in defects treated with 2.5 μg BMP-2, significantly reduced bone formation by 75% and vascular volume by 50% in defects. However, the mechanical conditions permitted by the fixator throughout the study were unknown. Nevertheless, it appears that an initial phase of tissue maturation and vascular infiltration must be achieved before relatively large magnitude biomechanical loads can be transferred to the tissue, though a quantitative understanding of what constitutes relatively large is yet to be determined.

Glatt and colleagues treated a 5 mm rodent femoral defect with a collagen sponge delivering 11 μg BMP-2 and a dynamic external fixation system[133]. Interestingly, they found that initially affixing a relatively compliant fixator then increasing its stiffness at 2 weeks enhanced maximum torque to failure of the femur at 8 weeks. The bone and callus cross-sectional area of femurs secured with the dynamic fixation scheme was significantly lower than femurs secured with either high or low stiffness fixators throughout. Qualitative examination of micro-CT images indicated that dynamic fixation produced healed defects with thicker cortical bone and less trabecular bone compared to the other fixation systems. When comparing the experimental design of the preceding rodent studies, it is important to note that Glatt and Schwarz utilized unilateral defects whereas bilateral were studied by Boerckel[34,62,133,134]. This may have affected the ambulatory load-share transferred through

the operated limb. Additionally, the transition in the apparent axial stiffness of the "stiff" to "compliant" fixation configurations in the two studies utilizing dynamic fixation were dissimilar: approximately 25 to 30 N/mm for Glatt, and 8.4 to 349.5 N/mm for Boerckel[26,135]. Therefore, the relative change in the tissue mechanical environment introduced by actuation of the fixation system was drastically different between the two studies. Hou et al. studied a critically sized femoral defect in goats secured with either a stiff or spring-loaded intramedullary rod treated with demineralized bone matrix seeded with goat MSC's[136]. The uniaxially compliant fixation system increased callus formation and blood flow at early time points and improved torsional stiffness and strength at 8 and 16 weeks when compared to the static fixation system. These studies have demonstrated that a controlled compressive loading regimen can act as an anabolic stimulus to promote repair in large bone defects treated with cells or biologics. Analysis of the mechanical boundary conditions imposed by the fixation system and scaffold over time is needed to elucidate the underlying mechanical cues modulating bone and vascular growth in disparate animal models.

The regulation of bone healing by static tension is well established by the clinical practice of distraction osteogenesis, in which incremental tensile strains are introduced into an osteotomy gap by an external fixator to promote bone lengthening[11,137,138]. The distraction technique consists of a controlled surgical osteotomy, followed by up to a week of static rest. Then, the external fixator is actuated to gradually separate the osteotomy ends 1 mm per day in four 0.25 mm increments. Distraction proceeds for 1-2 weeks or until the desired length is achieved, followed by locking the fixator to permit consolidation of the gap over 8-12 weeks[139]. The application of a small tensile strain appears to promote robust

intramembranous ossification and vascularization, while inhibiting cartilage formation[140,141]. Matsubara and colleagues demonstrated that distraction induces bone formation through cooperative secretion of angiogenic and osteogenic factors between mesenchymal cells in the defect region and vascular tissues in the surrounding muscle[141]. The healing response is highly sensitive to the mechanical environment produced by the distraction rate[142]. Increasing the distraction rate to 2 mm per day can result in fibrous non-union, bone weakening, soft tissue contracture and nerve lesions[143]. Conversely, decreasing the distraction rate can result in premature bridging of the gap[11,137]. Evidently, a relatively narrow range of small static tensile strains promotes intramembranous bone formation during distraction osteogenesis. The addition of short bouts of compression alternating with the standard distraction protocol, nicknamed the "accordion technique," has been investigated in an effort to simultaneously promote endochondral and intramembranous healing in defects with delayed callus formation[139,144]. Small clinical reports of the accordion maneuver have shown some anecdotal evidence of efficacy, but rigorous studies to elucidate any mechanistic changes in healing due to the addition of compression is lacking[145].

Bending, torsion and shear deformations generate stress distributions with significantly higher spatial complexity, and their effect remains controversial. Augut et al. compared pure shear versus compression up to 1.5 mm of a 3 mm tibial osteotomy in sheep. Shear significantly attenuated healing compared to axial motion, reducing defect bridging by 70%, callus area by 36%, and stiffness by over 60%[146]. Conversely, Bishop et al. reported improved intercortical mineralization in a 2.4 mm ovine osteotomy subjected to rotational shear compared to static or axially compressed specimens[147]. Thus, bone defects

appear highly sensitive to shear stimuli, which can dramatically attenuate healing or result in tissue failure if excessive loads are applied. To improve our understanding of how local mechanical signals regulate tissue compositional changes in vivo, specimen-specific experimental measurements of external loads and tissue composition acquired at multiple time points (or continuous local measurements) are needed.

2.4 Implantable Sensors for Orthopaedic and Regenerative Applications

Sustained technological advancements in microelectromechanical systems (MEMS) and short-range wireless communication systems have rapidly refined biomedical sensor technologies, motivating research to explore implantable sensor based approaches to investigate an array of clinical diseases[148–153]. A large body of research has demonstrated various biomedical applications of sensors, but most efforts have focused on clinical monitoring rather than preclinical applications[154,155]. Implantable sensors vary widely in their designs and fabrication techniques, but the endpoint sensing modalities include biopotential[156], electrical impedance[157], pressure[158,159], flow[160,161], strain[162], oxygen[163], pH[157] and glucose[164,165]. Clinical diagnostics have greatly benefited from implantable sensors, as they enable *in situ* monitoring of physiological metrics to track the progression of or recovery from a disease. Sensing mechanisms for implantable MEMS sensors include mechanical[158], optical[159], magnetic[166], and electrochemical detection methods[163], as well as combinations thereof, which underscore the appeal of MEMS technology; implantable MEMS can transduce a physiological input into an electrical output, oftentimes requiring only a small sample or stimulus.

Indeed, a number of sensor modalities could provide valuable insight into healing processes including pressure for intraocular, intracranial, and intravascular pathologies, pH and temperature for infections, glucose for diabetes, and even specific relevant biomarkers for inflammation, matrix production, or vascularization. Implanted as well as externally-mounted probes and sensors have been implemented in the past, but have typically been limited to large animals due to the size constraints imposed by cheaper and higher-throughput pre-clinical rodent and mouse models[50,149,167–169]. However, miniaturization coupled with novel passive and active sensor designs have now progressed to the point that sensing platforms can be readily fabricated at feasible size scales for small animal model applications.

Once deployed, microfabricated sensors can wirelessly transmit quantitative measurements in real-time, eliminating the need to anesthetize the animal or disrupt normal ambulatory activities. Thus, the frequency and duration of data acquisition is primarily limited by the power consumption of the sensor and wireless telemetry relative to the capacity of the power source (implanted battery, if active circuity is utilized). The data acquired from implanted sensors quantify the temporal profile of the parameter of interest, but there are limitations to the scale and resolution that spatially heterogeneous environmental factors can be measured due to the size of the probe since a locally positioned sensor or even a sensor array can only provide a discrete number of spatial measurement(s). To better describe spatial variations throughout a tissue, sensor measurements could also be applied as a validated time-varying boundary condition at their respective position(s) for image-based computational models of healing tissues, better capturing spatial heterogeneity. The potential of implantable sensors to longitudinally

monitor important environmental cues during regenerative processes in pre-clinical models could aid in the rational design and evaluation of novel therapeutics and advance understanding of the fundamental principles of mechanobiology[170]. Identifying the utility of biomedical sensor modalities, we concluded that the development of a wireless, implantable strain sensor would help to improve our understanding of how mechanobiological processes are regulated in vivo, and how they may be exploited to enhance bone repair.

CHAPTER 3. WIRELESS IMPLANTABLE SENSOR FOR NON-INVASIVE, LONGITUDINAL QUANTIFICATION OF AXIAL STRAIN ACROSS RODENT LONG BONE DEFECTS

3.1 Introduction

Fracture healing is a dynamic physiological process requiring rapid and highly-coordinated morphogenesis of numerous cell populations to restore functional bone tissue. While the majority of the 12 million annual fractures in the United States heal without complications, 5-10% of fractures do not heal in a timely fashion and require lengthy clinical interventions involving multiple surgeries before function is restored[2,3,11,171]. To address this unmet clinical need, much research has been devoted to understanding mechanisms of fracture non-union and to developing novel therapeutic strategies to stimulate bone repair. As the primary load bearing tissue in the human body, bone development, maintenance, and regeneration are remarkably sensitive to mechanical cues[172–174]. Numerous studies have identified the critical role of local mechanical cues in tissue differentiation, formation, and functional restoration of bone defects[34,49,50,62,126,127,130,175,176]. Due to these findings, mechanical stimulation has long been sought after as a putative target to stimulate endogenous bone healing mechanisms.

Before moving to costly and resource intensive studies in large animals, the rodent femoral defect model has emerged as a primary pre-clinical test bed to evaluate novel therapeutics—including drugs, biologics, and scaffolds—for the treatment of load-bearing bone defects[177,178]. In this model, various fixation systems have been utilized with varying

levels of load-sharing across the defect region. Ultimately, the mechanical environment experienced locally by cells in the defect milieu regulates the healing response[179]. Given the transient nature of bone repair, these tissue-level mechanical cues evolve rapidly with time after injury and are highly dependent on the specific injury model and treatment under investigation. However, the biomechanical environment in these models has rarely been analyzed and the multi-scale role of mechanical stimuli in the observed healing response remains poorly understood.

To elucidate the role of mechanical stimuli in skeletal healing, there is a need to quantify the mechanical environment experienced by the healing tissue during routine in vivo activities. However, standard techniques for quantitatively assessing the mechanical environment in pre-clinical animal models are limited to external fixation systems periodically affixed to mechanical loading instruments which impart a prescribed load stimulus to the defect[49,134,180], or computational image-based finite element (FE) simulations based on estimated mechanical boundary conditions[62]. The boundary conditions applied to such models are typically based on broad assumptions because they are challenging to measure non-invasively and change throughout the progression of healing. Consequently, neither technique directly captures loading patterns due to functional activities such as walking. Recognizing these limitations, we reasoned that the ability to directly and longitudinally measure the mechanical environment during fracture healing would enable quantification of the mechanical cues produced in specific bone defect models, and provide a more detailed understanding of mechanical stimuli that can promote or impair functional healing of skeletal injuries.

Sustained technological advancements in microelectronics and short-range wireless communication systems have rapidly refined biomedical sensor technologies, thus motivating research to explore implantable sensor based approaches to monitor an array of clinical diseases[148–151]. In particular, the introduction of small and inexpensive passive and active telemetry systems show promise for rapid deployment into pre-clinical models. The potential of implantable sensors to longitudinally monitor important environmental cues during regenerative processes in pre-clinical models could aid in the rational design and evaluation of novel therapeutics and advance understanding of the fundamental principles of mechanobiology[170]. To achieve this, we set out to engineer an implantable strain sensor—with a sufficiently small footprint to be utilized in the rodent femoral defect model—that can wirelessly transmit real time measurements of mechanical strain across a bone defect to a computer.

To obtain accurate measurements, an implantable sensing device should possess key functional characteristics including sufficient sensitivity and signal resolution to detect relevant changes in the parameter of interest (e.g. mechanical strain), limits of detection well outside the physiological dynamic range, and stable electromechanical characteristics throughout implantation under repeated functional loading and submersion in bodily fluids. In addition, telemetry must possess sufficient signal strength for wireless transmission through bodily tissues and an adequate power source for long-term data acquisition. The packaged device must be biocompatible, and preferably be compatible with longitudinal imaging techniques (e.g. radiography). Furthermore, the implant must have an adequate envelope for implantation in pre-clinical rodent models while maintaining mechanical durability to withstand surgical deployment and animal activity. Finally, a data acquisition

system requiring minimal external hardware for logging wireless measurements to a PC is desirable. These characteristics informed our approach to the design of the device and the test methods used to characterize and validate its capabilities.

The objective of this chapter was to develop and characterize an implantable strain sensor for non-invasive, real-time monitoring of axial strain across a rodent femoral defect due to functional activity. Extensive ex vivo and in vivo validations were conducted to evaluate the device to meet the aforementioned functional criteria. Herein, we present the design, characterization, and in vivo evaluation of the device's capabilities for quantitatively interrogating functional biomechanics post-fracture.

3.2 Methods

3.2.1 Strain Sensor Device Design

The implantable device consisted primarily of two components: (1) an internal fixation plate instrumented with a strain sensor and (2) a stacked board processing unit enabling sensor functionality and wireless data transmission. The modular fixation plate used to stabilize the rat femoral defect, as reported in previous studies, consists of a polysulfone segment which acts as the fixator and two stainless steel plates which interface the polysulfone segment with each end of the femur (Figure 2) [181,182]. The radiolucent polysulfone segment was modified to accommodate a single-element 350 Ω micro strain gage (Vishay PG EA-06-125BZ-350/E, Raleigh, NC) adhered into a recessed pocket on the back side by a two-component epoxy (Vishay PG M-Bond AE-10) while permitting in vivo radiographic imaging of the healing defect. Insulated lead wires running to the processing unit were soldered to the strain gage pads, cannulated through medical grade

silicone tubing, and routed into a recessed channel on the side of the plate. To protect the sensor from fluid infiltration and mechanical impingement during surgery, the wire channel and pocket containing the strain gage was potted with a biocompatible (ISO 10993) light-curing sealant (Dymax 1072-M, Torrington, CT) and shielded by thin (380µm thick) laser-cut Teflon covers.

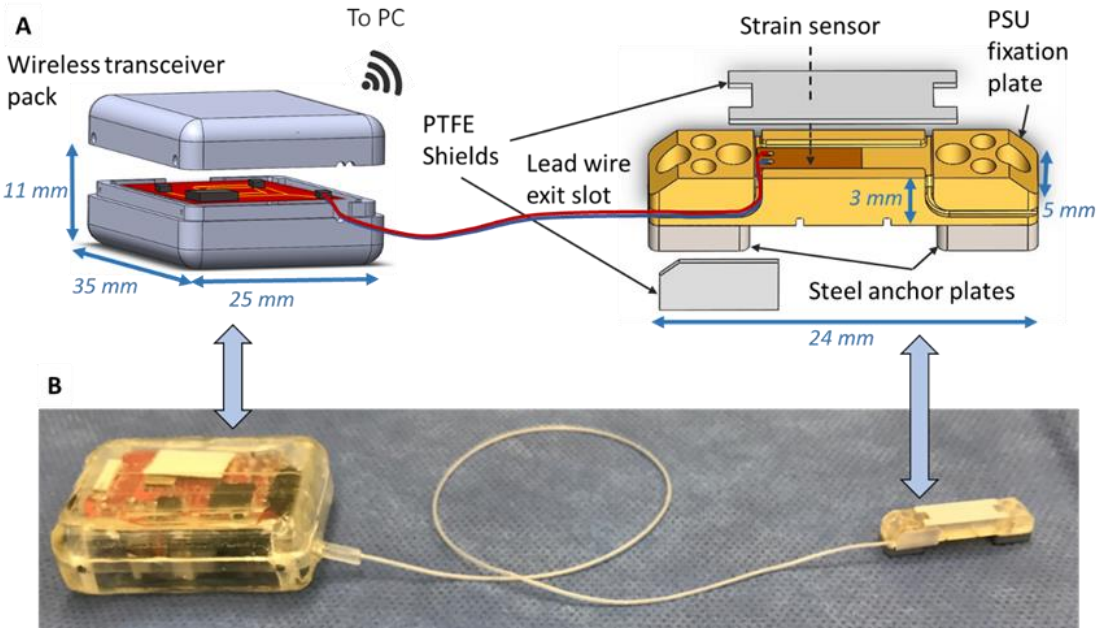

Figure 2: Implantable strain sensor (A) Exploded view schematic of instrumented internal femoral fixation plate with sensor adhered in recessed pocket on plate and lead wires routed through machined slot to the transceiver pack mounted in the abdominal cavity. Note: plate and transceiver schematics are not to same scale. **(B)** Photograph of instrumented plate before surgical implantation.

The stacked chip processing unit consisted of an active wireless network system (Texas Instruments EZ430-RF2500, Dallas, TX) featuring an ultra-low power microcontroller and 2.4 GHz RF transceiver. The network chip was interfaced with a custom signal conditioning circuit including a Wheatstone bridge, low pass filter, two-stage amplifier, voltage regulator, and 240 mAh lithium coin cell battery (Energizer CR-

2032, St. Louis, MO) permitting approximately 33 total hours of active data transmission at 7-8 Hz. After connecting the circuit to the sensor lead wires, the entire stacked chip was housed in a custom 3D printed pack (Stratsys RGD720, Eden Prairie, MN) and encapsulated with the same biocompatible sealant used for the strain sensor. Wireless sensor data were acquired in real-time via a paired transceiver and USB plug-in mounted to a remote computer using a custom MATLAB graphical user interface (Mathworks, Natick, MA).

3.2.2 Electromechanical Characterization

The electromechanical characteristics of three instrumented fixation plates were evaluated ex vivo to assess the sensor's sensitivity to detect strains due to physiological ambulatory loads and robustness to sustain long-term measurements in the in vivo environment. In order to simulate the eccentric bending loads placed on the internal fixation plates during functional loading, each end of the plates were attached to pre-drilled and tapped aluminum blocks approximating the length and cross-sectional area of the distal and proximal ends of the femur post-osteotomy using the same screws used to anchor the plate to the femur during surgery (Figure 3A). After assembly, a mechanical testing instrument (Electroforce 3220, TA Instruments, New Castle, DE) was used to apply cyclical compressive axial loads to the aluminum block-fixation plate construct. The constructs were pre-loaded to -2.5 N and tested for 25 cycles by a 0.5 Hz sinusoidal waveform to various magnitudes under displacement control, creating tensile local strains on the back surface of the fixation plate to which the strain sensor was adhered. Each test condition was repeated in triplicate for all three devices. The maximum displacement magnitude for each test was selected to achieve resultant axial load magnitudes of 16-20

N, which was the estimated peak axial force on the femur of a 250 g rat based on kinetic analysis of rodent gait[183]. In addition to testing the sensor with an empty gap between the two aluminum blocks, cylindrical defect surrogate materials of 40A polyurethane rubber and Teflon (McMaster-Carr, Douglasville, GA) were placed to fill the gap between the blocks to mimic the stiffness of the bone defect region during different stages of healing, including the proliferating soft tissue callus stage and the eventual mineralization stage (Figure 3B; Rubber: elastic modulus = 4.766 ± 0.1153 MPa, axial stiffness = 19.26 ± 0.3646 N/mm; Teflon: elastic modulus = 319.3 ± 2.100 MPa, axial stiffness = 681.3±39.11 N/mm). Throughout testing, the local axial strain along the sensor region of the fixation plate was measured by laser extensometer (LX-500, resolution = 1µm, MTS, Eden Prairie, MN) while simultaneously recording the differential voltage output of the strain sensor to validate the measurements (Figure 3C).

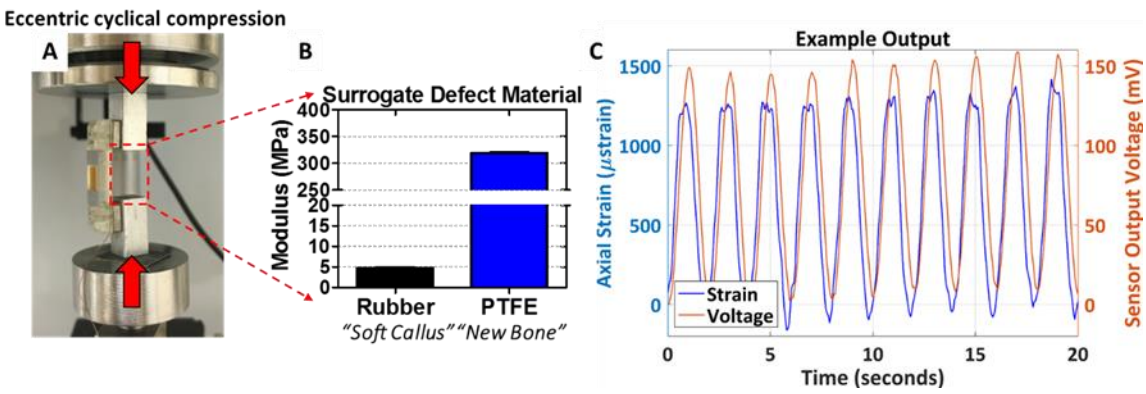

Figure 3: Eccentric cyclical compression testing (A) Experimental set-up for eccentric cyclical compression testing of instrumented fixation plates. **(B)** Elastic moduli of surrogate defect materials, which are placed in the gap between the loading blocks to simulate the progression of mechanical properties during bone defect repair. **(C)** Example output during a cyclic test, where local strain in the sensor region as measured by laser extensometer is plotted alongside the corresponding voltage signal from the sensor.

3.2.3 Fatigue Testing

In order to assess the durability of the sensor to endure repeated flexural strains due to ambulatory loading, three plates were cyclically loaded in three-point bending to achieve the maximum anticipated local axial strain on the sensor in vivo (6800 με). Loads were applied for 10,000 cycles at 1 Hz while recording the output from the sensor.

3.2.4 Biostability

To ensure the electromechanical characteristics of the sensor were stable under prolonged exposure to bodily fluids, instrumented fixation plates (n=2) were submerged in phosphate buffered saline (PBS) and placed in an oven at 37 °C for 4 weeks[184]. Prior to submersion and at weekly intervals thereafter, the sensitivity of the strain sensor was quantified by loading the fixation plate in three-point bending over a range of physiological strain magnitudes on the sensor from 300 to 6800 με.

3.2.5 Surgical Procedures

All procedures were approved by the Georgia Institute of Technology Institutional Animal Care and Use Committee (IACUC protocol A14040). After arrival, rats were single housed for 1–2 weeks after procurement for acclimatization before experimental use, with unlimited access to food and water under a 12:12 hour light:dark cycle throughout the study. Unilateral 6 mm segmental defects were surgically created in the femurs of 8 month old male retired breeder Sprague Dawley rats weighing approximately 550-650 grams (n=2, CD, Charles River Labs, Wilmington, MA) under isofluorane anesthesia (1.5-2.5%) using a modification of previously established procedures to implant the transceiver pack

in the abdominal cavity[185]. Briefly, the left femur was exposed from an anterior approach using blunt dissection. Next, the abdominal cavity was exposed by a 2 cm midline skin incision initiating 1 cm below the sternum (xiphoid) followed by an incision of the abdominal musculature (on the linea alba) and peritoneum, avoiding the sub-diaphragmatic organs. A keyhole incision was made through the abdominal wall superior to the left inguinal ligament and the fixation plate and associated wire were passed through the keyhole into the hindlimb compartment before positioning the transceiver pack into the abdominal cavity. The peritoneum and abdominal musculature were then sutured and the skin was closed with wound clips. The keyhole incision was carefully sutured with a loose loop around the traversing wire to prevent herniation while permitting translation of the wire during joint movement. The fixation plate was mounted to the anterolateral aspect of the femur using 4 screws and a critically sized 6 mm defect was created in the mid-diaphysis using an oscillating saw and left untreated. A subcutaneous injection of sustained-release buprenorphine was administered for analgesia prior to surgery.

3.2.6 Wireless Data Acquisition during Treadmill Walking and High-Speed Radiography

One week prior to surgery, animals were trained to walk on a rat treadmill (Metabolic Modular Treadmill, Columbus Instruments, Columbus, OH) at slow ambulatory speeds ranging from 0.08-0.16 m/sec. A custom radiographic imaging system consisting of bi-plane X-ray generators and X-ray image intensifiers (Imaging Systems & Service, Inc., Painesville, OH) modified with the addition of high-speed digital video cameras (Xcitex XC-2M, Woburn, MA) was utilized to obtain high-speed images of the animal's skeleton during walking periods. Three days after surgery, animals were imaged (100 frames/s; Camera 1 – 42 kV, 80 mA, 5 ms exposure; Camera 2 – 40 kV, 80 mA, 5 ms

exposure) while walking on the treadmill at 0.1 m/sec. Throughout all treadmill activities, strain sensor readings were recorded wirelessly at 7-8 Hz.

3.2.7 Statistical Analysis

All data are presented as mean ± standard deviation unless otherwise stated. Multiple group comparisons were assessed by analysis of variance (ANOVA), with pairwise comparisons analyzed using Tukey's post-hoc test (Graphpad Prism 7, San Diego, CA). A one-sample two-tailed Student's t-test was utilized to evaluate fatigue testing results. A p-value < 0.05 was defined as a statistically measurable difference.

3.3 Results

3.3.1 Electromechanical Characterization

The results of off-axis electromechanical characterization are summarized in Figure 3 and Table 1. Sensors exhibited high linearity (Table 1; $r^2=0.993 \pm 0.017$, $p<0.0001$ all tests) and distinct sensor outputs for each test condition, (Figure 4; $p<0.001$ all comparisons), demonstrating the sensor had sufficient sensitivity to detect changes in axial strain on the fixation plate under loading at different healing stages (with different stiffness surrogate defect materials). Taking into account op-amp gain and excitation voltage used for empty and rubber surrogate mechanical testing, the overall sensitivity of the device was 0.287 ± 0.035 μV/V/με. Sensitivity under Teflon surrogate test conditions could not be computed as local plate strains were at or below the resolution of the laser extensometer and could not be reliably measured.

Table 1: Eccentric cyclical compression output summary. Sensor output and linear regression results for electromechanical characterization testing.

Sensor	Surrogate Defect Material	Sensor Output (mV/N)	r^2	p-value
1	Empty	28.2	0.999	5.16E-32
2	Empty	28.1	0.999	6.02E-34
3	Empty	30.0	0.999	4.47E-38
1	Rubber	21.3	0.998	1.64E-18
2	Rubber	18.8	0.999	3.32E-26
3	Rubber	19.7	0.999	4.07E-23
1	Teflon	2.62	0.998	7.55E-15
2	Teflon	0.94	0.947	1.06E-07
3	Teflon	2.74	0.999	6.84E-17

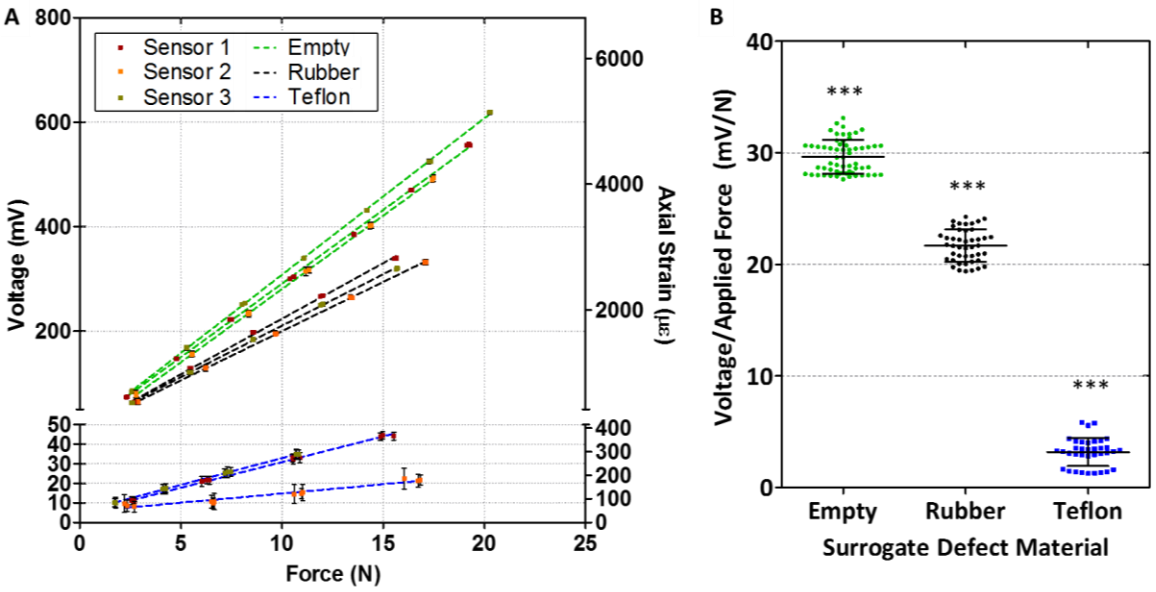

Figure 4: Strain sensor output is highly linear and sensitive to defect stiffness (A) Sensor output plots for a range of physiological load magnitudes. The color of the dot represents a different sensor and the color of the line represents a different defect surrogate material. Cyclical tests were repeated in triplicate for each loading case, and error bars depicting standard deviation are included on all data points. **(B)** Normalizing the voltage output of the sensor by applied force demonstrates the sensor is able to discern changes in the stiffness of the defect region, and therefore appears promising to detect progression of bone repair under physiological load conditions, *** $p<0.001$, ANOVA, all comparisons.

To quantify the lower limit of detection of the device, we computed the signal-to-noise ratio (SNR) of the mechanical testing output and performed linear regression as a function of axial strain on the fixation plate (Figure 5, Table 2). A limit of detection cut-off criteria of 20 dB (corresponding to a signal amplitude-to-noise ratio of 10-1) was applied and linear regression computed that 300 με was the minimum detectable strain amplitude on the fixation plate that would be utilized in analysis of in vivo testing. Strains of this magnitude were only observed in Teflon surrogate defect testing, suggesting the sensor possessed sufficient resolution to accurately characterize the strain due to functional loading until and potentially after complete and robust bridging of the entire bone defect occurred.

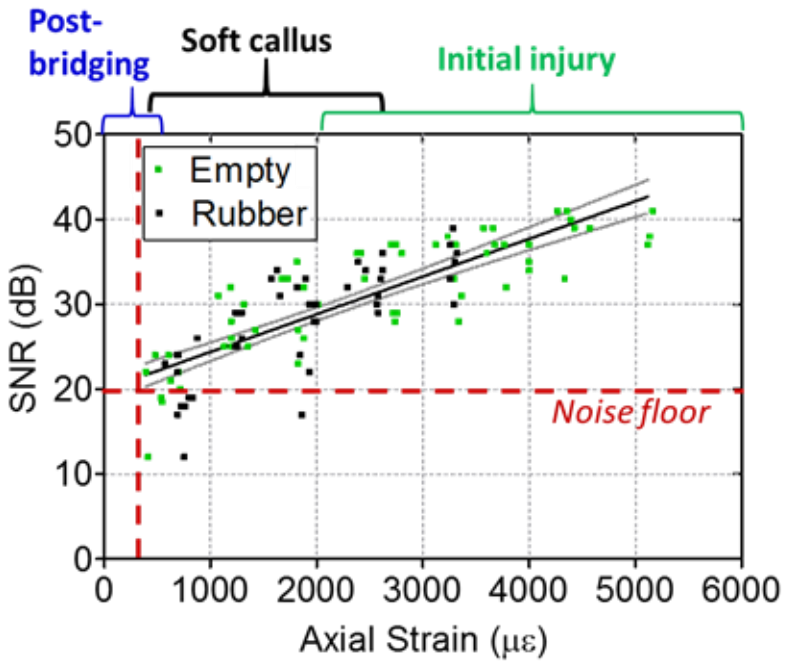

Figure 5: Limit of detection analysis Regression of signal to noise ratio (SNR) of sensor output versus the local axial strain of the sensor region as measured by laser extensometer. Employing a limit of detection cut-off criteria of 20 dB (corresponding to a signal amplitude-to-noise ratio of 10-1) demonstrates the sensor can reliably detect plate strains

as low as 300 με. These data indicated the sensor possessed sufficient resolution to obtain measurements until and potentially after robust bridging of the bone defect occurred.

Table 2: Limit of detection analysis summary

Linear Regression 95% Confidence Intervals	
Slope (dB/με)	3.8×10^{-3} to 5.1×10^{-3}
y-intercept (dB)	18.37 to 21.55
r^2	0.6618

3.3.2 Fatigue Testing

The normalized output of sensors (n=3) throughout 10,000 cycles was analyzed to determine if repeated deformation at the maximum anticipated strain in vivo would alter its sensitivity (Figure 6A). Throughout testing, the response of the sensors was stable within ± 4%. The slope of the regression lines (Table 3; $-2.32 \times 10^{-7} \pm 2.32 \times 10^{-6}$) was not significantly different from 0 (p=0.877), demonstrating the sensor was sufficiently durable to maintain a constant sensitivity under high cycle peak physiological loads.

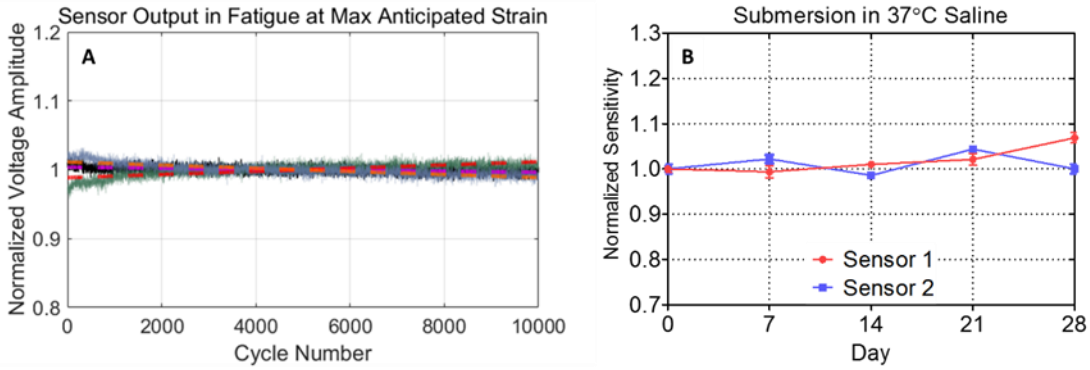

Figure 6: Fatigue and submersion testing results (A) Fatigue testing of the devices (n=3) for 10,000 cycles at maximum anticipated physiological strain. The normalized raw outputs for each device is shown, and their respective regression lines are depicted by the bright dotted lines. Throughout 10,000 cycles the outputs were stable within +/-4 percent and the resultant slope was not significantly different than zero (p=0.877). **(B)** Instrumented fixation plates were submerged in saline maintained at body temperature for 4 weeks and sensitivity was evaluated by mechanical testing at weekly intervals. The output was stable

within 7% throughout the test and sensitivity plots for all time-points remained highly linear (r^2 range = 0.9938-0.9988).

Table 3: Fatigue testing linear regression results

Sensor	Slope (cycle^{-1})	y-intercept
1	-7.32E-07	1.003
2	2.30E-06	0.989
3	-2.27E-06	1.011

3.3.3 Biostability

Throughout submersion in PBS at body temperature, the sensitivity of the sensor was stable within 7% of the value measured prior to submersion (Figure 6B). High linearity was maintained throughout testing trials (r^2 range = 0.9938-0.9988). These data indicate that the sensor can sustainably provide precise measurements under long term physiological conditions.

3.3.4 Wireless Strain Data Acquisition and Radiographic Imaging of Rodent Gait after Surgical Implantation and Creation of Femoral Defect

After implantation of two devices in untreated 6 mm femoral defects, strain data were recorded wirelessly by a nearby laptop. Stable wireless acquisition was maintained up to a distance of approximately 20 feet, with further increasing distance resulting in lost data packets and thereby reducing sampling frequency. The presence of metal tables or objects in the transmitter line-of-sight was determined to reduce the transmission range to as low as 5 feet, depending on the spatial configuration. Three days after surgery, the rats were walked on a treadmill at a slow speed of 0.1 m/sec. The belt speed was selected to

produce a gait cycle of about 1-1.3 Hz, which was sufficiently slow to mitigate the risk of severe aliasing the gait cycle while recording strain data at 7-8 Hz. The logged sensor data were synchronized to 6 second videos of the animal recorded by high-speed radiographic videos from two different angles. The synchronized videos demonstrated the sensor signal coincides with the phase and frequency of the operated limb gait cycle, with lower strains being measured when the leg is lifted and rapid increases in strain observed when the leg is planted.

Absolute strains on each plate were computed from the in vivo voltage signal based on the calibrated sensitivity determined by electromechanical characterization of each device prior to implantation. To account for changes in the zero strain set-point which occur while surgically anchoring the fixation plate to the femur, the voltage corresponding to zero static strain was estimated by the median voltage signal while the animal sat in its cage prior to the treadmill walking period, which was nearly constant due to the minimal motion of the animal. During the videos, peak strains of up to 3290 με were observed during loading phases, whereas strain reversal relaxed the static flexural strain on the plate up to -3140 με while the leg was lifted (Figure 7).

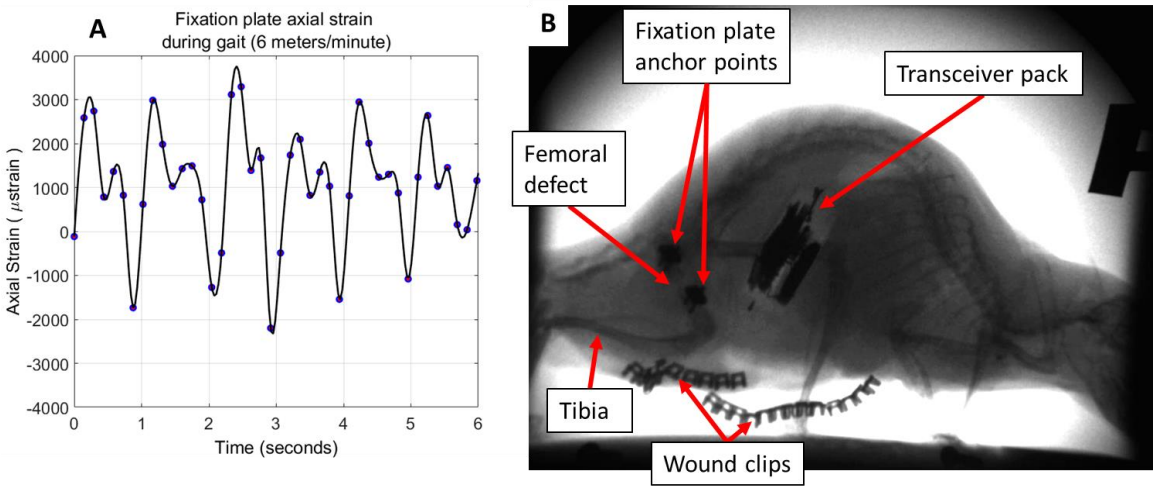

Figure 7: Real-time data collection synchronized with high-speed X-ray (A) Representative *in vivo* strain versus time measurement recorded wirelessly during ambulation on a treadmill three days after the creation of a 6 mm segmental femoral defect. Actual data points are depicted as circles with a spline curve-fit illustrated by the black line. **(B)** During data acquisition, high-speed radiographic videos were acquired by two x-ray cameras mounted at different angles. The videos were synchronized with the recorded sensor output to validate the ability of the sensor to non-invasively quantify functional strains in real-time. Radiopaque objects including the stainless steel components which anchor the femoral fixation plate, the abdominally implanted transceiver circuit pack, and the incision wound clips are labelled.

3.3.5 Fixation Plate Strain Analysis

The distribution of dynamic strain cycles experienced by the fixation plate during the entire treadmill walking period for both animals were quantified using a peak analysis to compute strain amplitudes between adjacent local minima and maxima in the recorded sensor signals (MATLAB). The load history revealed a number of similarities between the two animals. Histograms of the strain amplitudes indicate a skewed distribution with approximately 35% of the total strain cycles falling in relatively low strains between 300 to 1000 με (Figure 8). The incidence of strain cycles between 1000 to 5000 με were observed to be nearly constant for both implants. The median and 95th percentile strain

amplitude were computed to be 1929 με and 5543 με, and 1889 με and 6041 με for each implant respectively.

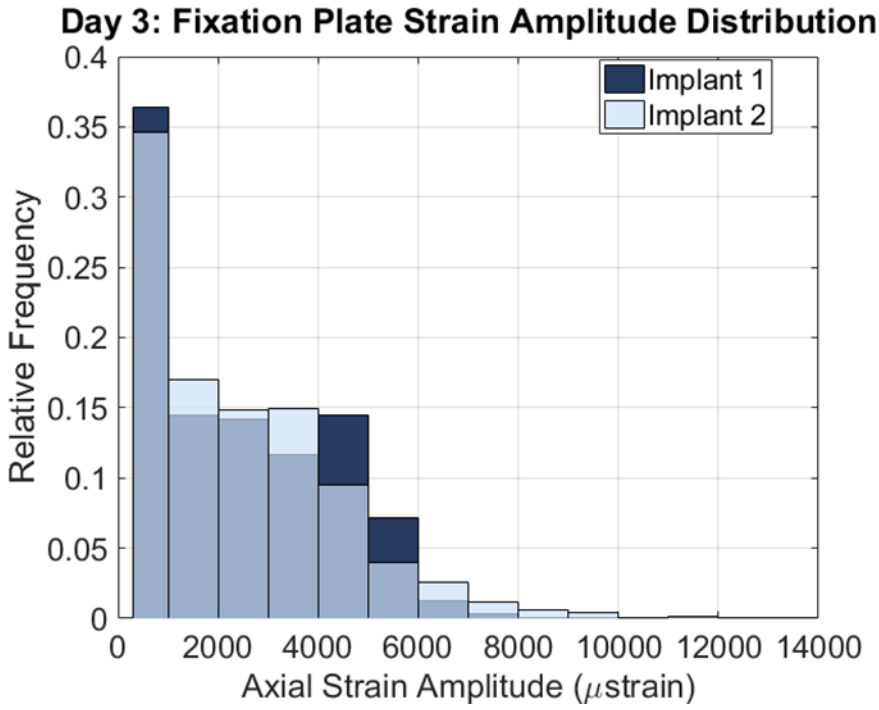

Figure 8: Strain amplitude distributions during ambulation. Median and 95th percentile strain amplitude were computed 1929 με and 5543 με, and 1889 με and 6041 με for each implant respectively.

3.4 Discussion

The mechanical environment within healing tissue evolves rapidly with time and is challenging to quantify longitudinally in a non-invasive fashion. The aim of this study was to develop, characterize and evaluate the ability of an internal fixation plate with an integrated wireless strain sensor to non-invasively quantify dynamic axial strains across a rodent bone defect during functional activity. Key technical criteria were defined and evaluated through ex vivo and in vivo experiments. In summary, the data indicate the sensor possesses sufficient sensitivity to detect progressive changes in physiological strain

as healing occurs. Additionally, the lower limit of detection was sufficient to obtain strain measurements until robust bridging of the entire defect occurs. The sensor was proven to withstand 10,000 cycles at the maximum in vivo strain with no change in sensitivity, indicating the dynamic range of the sensor encompasses the relevant physiological range. Submersion testing demonstrated the sensor is packaged and sealed in a manner which maintains electromechanical stability for sustained physiological measurements. In vivo implantation demonstrated the device could be surgically implanted into a rat femoral segmental defect model and successfully transmit data wirelessly to a nearby computer. Animals tolerated the abdominal implant well throughout the study. Strain measurements were acquired in real-time while animals walked on a treadmill and the data were validated by synchronizing to high-speed radiographic videos recorded simultaneously. High-speed x-ray imaging was a desirable validation technique for the sensor because it allowed for direct and accurate visualization of the position of the long bones during the gait cycle, overcoming movement artifacts caused by the large amount of soft tissue mass surrounding the hindlimb which limits the accuracy of standard optical imaging techniques[186].

The primary contribution of the reported device is the capability to longitudinally acquire quantitative measurements describing the in vivo evolution of the mechanical environment during bone healing. Perren et al. were the first to develop a predictive theory of mechanical boundary conditions that determine the differentiation of skeletal tissues after fracture[130]. Since then, many studies have utilized a variety of experimental and computational techniques to elucidate tissue-level mechanical conditions that enhance or impair bone repair[34,49,50,62,126,127,175,176]. While these studies have refined our understanding of the mechanobiological regulation of fracture healing, the majority of the studies rely on

non-physiological mechanical stimuli[49,134,176,180] or assumed boundary conditions for computational analysis that are not determined from the specific model under investigation[62]. A key limitation in the field is the technical challenge of longitudinally and non-invasively measuring mechanical conditions in in vivo models of skeletal healing[168,187]. By incorporating a wireless sensor, the mechanical boundary conditions of the defect can be quantified during physiological activities without disrupting the normal activity of the animal to obtain the measurement. The non-destructive measurement approach maximizes the amount of data acquired from a single animal, thereby reducing the number of animals needed to fully characterize the healing process and enabling specimen-specific analyses over multiple time points. Here we report a wireless device that has the capability to facilitate flexible, long-term data acquisition at discrete time points. The fully digital telemetry approach with an integrated ultra-low-power (50 μA) sleep mode permits the 33 hours of total power budget for active data transmission to be allocated over extended periods of time by programming the microcontroller for intermittent transmission. In our initial validation study, we selected a measurement protocol to obtain the majority of in vivo data within the first 72 hours post-surgery. In future studies, the measurement periods can be reprogrammed to extend the device over weeks and months.

The device also has some limitations. First, the single-element strain sensor is only capable of quantifying mechanical strain in one direction; in the configuration reported here it was along the axis of the femur. Wehner and colleagues performed kinetic analysis of rodent gait to demonstrate this direction is the primary load trajectory during ambulation[183]. In their analysis, bending moments in the mid-diaphysis were also observed in all anatomical planes. Based on this analysis and our own observations in the eccentric

loading tests, the sensor was positioned in the optimal region to detect the primary mode of deformation. In the segmental defect model, the addition of the fixation plate naturally produces an eccentric axial load on the plate and out-of-plane bending, resulting in peak local tensile strains on the sensor while the defect zone undergoes compression. The plate cross-section is designed so the bending moment of inertia is threefold higher to in-plane bending that cannot be detected by the sensor, so its contribution to the overall mechanical environment is less significant. Second, the single-element design is sensitive to temperature differences between the hindlimb and abdomen. However, the in vivo conditions are essentially isothermal between the two regions as confirmed experimentally by the negligible drift in the baseline voltage of the sensor throughout implantation. Future improvements to address the aforementioned limitations could include a sensor digital rheostat to provide remote control of baseline voltage. For the purposes of this study, a circuit sampling frequency of 7-8 Hz was selected as a compromise between battery life and sufficient sampling to avoid drastic aliasing of the gait cycle, which was approximately 1-1.3 Hz. Ideally, a higher sampling frequency (in the range of 25-30 Hz) for in vivo gait analysis would be desirable to ensure that peaks in strain are not aliased. In the following chapters, refinements to the transceiver design will be implemented to address these limitations.

To conclude, we report the characterization and initial in vivo data obtained by a novel implantable wireless strain sensor in a pre-clinical model of bone repair. The device is capable of measuring axial mechanical strain during physiological activities and met key technical criteria outlined in the introduction. The technological underpinnings are broadly applicable to the mechanical characterization of therapeutics in diaphyseal fracture or

defect models. This sensor platform is a promising approach to longitudinally characterize tissue mechanics in a specimen specific manner, enabling more detailed investigations into the role of the mechanical environment in bone repair.

CHAPTER 4. REAL-TIME MONITORING OF MECHANICAL CUES IN THE REGENERATIVE NICHE REVEALS DYNAMIC STRAIN MAGNITUDES THAT ENHANCE BONE REPAIR

4.1 Introduction

In CHAPTER 3, the implantable strain sensor system was validated through ex vivo and in vivo design validation testing. In this chapter, the strain sensor platform was implemented in a longitudinal study to characterize the temporal progression of mechanical signals in a regenerating orthotopic site, and to quantitatively evaluate the biomechanical and therapeutic effects of a load sharing-inspired approach on bone regeneration.

Tissue regeneration requires dynamic and spatially coordinated cellular activity involving bidirectional interactions between the healing niche and surrounding environment. Characterizing the progression of early-stage environmental cues in the regenerative niche and their contribution to divergent healing outcomes is a critical and active area of research. An improved understanding of biochemical and biophysical cues may inform the development of therapies that modulate the microenvironment to more effectively resolve challenging injuries[188]. Mechanical signals are among the most potent and dynamic environmental regulators of tissue repair[58,189]. In particular, forces exerted on musculoskeletal tissues during locomotion strongly influence regenerative processes[173]. The sensitivity of bone to extrinsic mechanical cues is well documented, where a moderate magnitude of mechanical loading accelerates osteoprogenitor differentiation, matrix mineralization, and restoration of biomechanical function[50,62,179].

Strategies for controlled transfer of mechanical loads in vivo are a promising therapeutic target to promote osteogenesis after fracture, segmental bone loss, spinal fusion, and joint arthroplasty. Indeed, there is substantial clinical need to enhance bone regeneration for the millions of patients undergoing these procedures each year, as a significant sub-set are afflicted with prolonged disability or multiple revision surgeries due to non-union or poor osseointegration[3]. Mechanical stimulation strategies have spanned a range of approaches and garnered significant scientific and clinical interest including external or percutaneous fixators and actuators[11], and stabilization hardware or scaffolds with reduced stiffness to permit load sharing[54,190,191]. Additionally, more functionally relevant, non-invasive methods such as physical rehabilitation and exercise may be implemented to enhance load transfer while simultaneously inhibiting adjacent tissue atrophy and accelerating functional recovery of daily activities[192–194]. Conversely, excessive loading can impair healing resulting in fibrosis, hypertrophic non-union, or construct failure[34,50]. A critical challenge limiting these techniques has been the ability to monitor the dynamic mechanical environment at the regenerative niche during repair—this mechanical environment has rarely been quantified, resulting in incomplete understanding of biomechanical conditions and limited means with which to reliably investigate the safety and efficacy of mechanical based interventions.

A promising approach to quantitatively evaluate mechanical cues during tissue repair is the integration of electromechanical sensors with devices already typically installed at the site of healing, such as fixation plates, implants, or scaffolds[170]. Advancements in microfabrication and wireless data transfer have attained a level of maturity and a sufficiently small size for biomedical applications. Recent reports of a broad

range of transient and permanent implantable sensors have facilitated new physiological insights in pre-clinical in vivo models as well as digital health monitoring in humans[152,153,195].

Using a pre-clinical rat model of long bone repair, we observed that varying load transfer modulates vascular and skeletal tissue formation after injury[34,62]. Motivated to better understand the temporal progression of tissue-level mechanical cues that could enhance skeletal repair, we recently developed a fully implantable strain sensor platform enabling real-time monitoring of mechanical boundary conditions across the defect during functional rehabilitative activities like walking[196]. The device possesses sufficient sensitivity and size for implementation in rats--animals which are used commonly used as a key pre-clinical test bed to screen therapeutic approaches before scaling up to more costly large animal models.

Here, we deployed this strain sensor platform with the objective to examine the evolution of biomechanical cues in the regenerative niche after injury and assess the effects of differing magnitudes of functional mechanical loading on bone defect repair and revascularization. We hypothesized that a moderate increase in ambulatory load sharing conferred by reduced stiffness fixation would increase mechanical stimuli initially, and that the elevated deformation would eventually decrease due to enhanced bone formation. We found that rehabilitative load sharing permitted by reduced stiffness of fixation substantially accelerated and enhanced bone repair. Furthermore, we observed that real-time monitoring of strain magnitude during gait correlated with the status of bone repair and that osteogenic ambulatory loading differentially regulated neovascular growth after injury. These results demonstrate the potential of advancements in biomedical sensors to

optimize mechanobiological therapies by remotely monitoring dynamic biophysical cues in vivo.

4.2 Methods

4.2.1 Device fabrication

A new digital transceiver unit was developed to provide a number of key functional improvements over the unit reportedly previously[196], mainly: (i) increased power budget and (ii) sampling frequency, (iii) improved connectivity via Bluetooth Low-Energy (BLE) wireless network, and (iv) remote-controlled circuit calibration. The unit used a BLE microcontroller (MCU) (Silicon Labs BLE113) to receive commands and transmit data at an increased frequency of 30 Hz through a PC-mounted USB receiver. A 620 mAh battery (Panasonic CR2450) was used to provide an 8 week power budget. Furthermore, a low-power receiving "sleep" mode was implemented, allowing the PC user to remotely activate to the unit to acquire and transmit measurements as needed, permitting flexible measurement time points and durations. A wirelessly-controlled digital rheostat was also implemented to allow remote calibration of the baseline voltage signal while implanted. The transceiver was encapsulated in a custom 3-d printed housing (Form 2, Formlabs) fully encapsulated in an ISO 10993 compliant UV-curing urethane (Dymax).

As previously described[196], the transceiver was connected via two 36 AWG braided stainless steel wires encapsulated in biocompatible silicon tubing (AM systems) to a single-element 350 Ω strain sensor (PGEA-06-125BZ-350/E, Vishay) integrated into a custom internal fixator used to stabilize the femoral defect. To modulate fixator stiffness and load sharing across the defect, the radiolucent, polymeric bridging element was either

polysulfone (PSU, McMaster-Carr) or ultra-high molecular weight polyethylene (UHMWPE, Quadrant), creating "stiff" and "compliant" fixator groups, respectively. Prior to implantation, each device was calibrated in three-point bending (TA Electroforce 3220) to strains encompassing physiological magnitudes.

4.2.2 Surgical procedure

Identical procedures were used in both bone repair and angiography studies. As previously described[196], a unilateral critically-sized 6 mm segmental defect was created in the left femur of 15-wk-old female CD (Sprague-Dawley) rats (Charles River Labs). Femurs were stabilized by either stiff (PSU) or compliant (UHMWPE) fixators with integrated strains sensors. Transceiver packs were mounted in the abdominal cavity and connected via a tunneled lead passing through a keyhole incision in the abdominal wall superior to the left inguinal ligament into the hindlimb compartment. Defects were either treated with 2 μg recombinant human bone morphogenetic protein 2 (BMP-2, Pfizer), delivered via a hybrid biomaterial scaffold described below consisting of 120 μL BMP-2-laden alginate hydrogel injected inside an electrospun polycaprolactone (PCL) tube, or left empty. Empty defects form negligible mineralized or soft tissue and served as non-healing negative controls. Animals were randomly allocated to experimental groups. Animals were anesthetized and then euthanized by CO_2 asphyxiation at either 3 or 8 weeks. All procedures were approved by the Georgia Institute of Technology IACUC (Protocol A17034).

4.2.3 Hybrid RGD-alginate/PCL scaffold production

Detailed scaffold production methods are described elsewhere[182,197]. Briefly, RGD-functionalized alginate (FMC BioPolymer) was reconstituted in α-MEM (Thermo Fisher Scientific) at 2% w/v. Recombinant human BMP-2 (Pfizer) was reconstituted in a 0.1% solution of rat serum albumin (Sigma-Aldrich) and 4 mM HCl and mixed with alginate, yielding 2 µg BMP-2 per 120 µL. The solution was ionically cross-linked with a 0.21 w/v $CaSO_4$ slurry mixed at a 1:25 volume ratio. Sheets of PCL nanofiber mesh were generated by electrospinning a 12% w/v solution of PCL in 90:10 (v/v) of hexafluoro-2-propanol:dimethylformamide from a syringe at a flow rate of 0.75 mL/h and a 15-20 kV potential onto a grounded collector plate 20-23 cm away. PCL sheets were laser cut into rectangles with a chessboard grid of 23 x 1 mm circular perforations, rolled and glued into 5 mm cylinders using ISO 10993 UV-curing adhesive (Dymax).

4.2.4 Gait analysis

Gait capture was performed longitudinally to assess hindlimb utilization for each rat using a Catwalk 7.1 system (Noldus). Rats were placed on an illuminated runway and allowed to walk freely between either ends. Illuminated paw prints were recorded by a digital camera and runs where the rat traversed the entire length of the runway were analyzed (2-3 runs per animal, 10 second max) before surgery for baseline, and 1, 2, 3, 4, 6, and 8 weeks after surgery. Automated footprint classifications were verified and corrected manually for each run. Paw print area and duty cycle (ratio of stance duration to the sum of stance and swing duration) were computed.

4.2.5 Treadmill walking

Before surgery, rats were acclimated to walk consistently on a treadmill (NordicTrack) at speeds ranging from 5-9 m/min over a period of 10-15 min. Beginning 1 week after surgery, and twice weekly thereafter, each animal was walked for 10 min at a consistent speed of 6.5 m/min, creating a gait cycle of approximately 1-2 Hz. The total distance travelled loosely approximated the distance traversed during one day of in-cage activity[198].

4.2.6 Strain measurement and analysis

During treadmill walking sessions, strain measurements were transmitted in real-time via Bluetooth to a nearby laptop and plotted on a custom Visual Studio C# (Microsoft) graphical user interface (GUI). Data was collected for 3 minutes of the treadmill session. After 4 weeks, strain was measured during the first treadmill period of the week. A custom MATLAB (Mathworks) script was developed to identify local maxima and minima pairs in the signal corresponding to individual step cycles, and strain amplitudes were computed.

4.2.7 X-ray video collection

One month after surgery, high-frame rate images of an empty defect control animal's skeleton were obtained to demonstrate sensor functionality during treadmill data collection. A custom radiographic imaging system comprised of bi-plane X-ray generators, image intensifiers (Imaging Systems & Service, Inc.), and high-speed digital video cameras (Xcitex XC-2M, Woburn, MA) was used to collect 6 second videos (100 frames/s; 43 kV, 100 mA, 5 ms exposure).

4.2.8 In vivo radiographs and microCT

In the bone repair study, in vivo radiographs and microcomputed tomography (microCT) scans were acquired at 2, 4, and 8 weeks to assess bone formation and bridging across the defect. Digital radiographs were acquired at 25 kV with a 15 sec exposure (Faxitron MX-20). MicroCT scans (VivaCT 40, Scanco Medical) were performed using 26.3 μm voxels, 55 kVp, 145 μA, and 300 ms integration time. Scans were manually aligned along the femoral axis prior to analysis. Mineral formation was evaluated inside a cylindrical volume of interest (VOI) of 5 mm in diameter and 4 mm long centered between the intact bone ends and encompassing the defect and PCL electrospun tube. Polar moment of inertia was assessed with a VOI encompassing all mineralized tissue throughout the entire defect and 1 mm of each bone end to include periosteal mineralization at the defect boundaries. Bone was segmented by applying a Gaussian filter (sigma=1.2, support=1) and a global threshold of 388 mg hydroxyapatite/cm^3, corresponding to half the density of intact cortical bone.

4.2.9 Biomechanical testing

After eight weeks, animals were euthanized by CO_2 asphyxiation, hindlimbs were cleaned of soft tissue, fixators were carefully removed, and femora were wrapped in PBS-soaked gauze and stored at -20° C until testing was performed 3 days later. Each femur was thawed before potting the ends in Wood's metal (Alfa Aesar). Specimens were tested to failure in torsion at 3°/sec using a load frame (TA Electroforce 3220). Failure strength was defined as the peak torque over the first 40° of rotation, and stiffness was assessed as the slope of the linear region of the torque-rotation curve.

4.2.10 Histology

One representative femur from both UHMWPE and PSU groups was selected for histology based on 8 week MicroCT bone volume. Samples were fixed in 10% NBF for 48 h at 4° C, then switched to PBS and shipped to HistoTox Labs for decalcification, paraffin processing, and staining. Midsagittal 5 µm thick sections were stained with H&E, Safranin-O/Fast Green, or Picro Sirius Red.

4.2.11 Finite element analyses

Finite element simulations of the femur-fixator system at 2 weeks were generated for representative UHMWPE and PSU samples. Images processing was performed in MIMICS (Materialise) to create models from animal- and time-specific in vivo microCT images. Image noise was suppressed using a Gaussian filter (sigma=1.2, support=1). The calcified tissue mask was cropped to only include the defect region and a sequence of erosion (radius =2) and dilation (radius=1) steps were applied to remove small volumes. Representative microCT-based geometries of the proximal and distal femur segments were manually aligned to the animal-specific bone segments visible in the microCT images. Unmineralized portions of the defect region were assumed to be a homogeneous cylinder of soft tissue (consisting of soft callus tissue and alginate) with a diameter of 5 mm (the diameter of the PCL tube), span the length of the defect, and centered about intact distal and proximal femoral segments. Mineralized bone was subtracted from the soft tissue mask to ensure continuity between mineralized bone and soft tissue. The PCL tube mask was aligned with and enveloped the soft tissue mask. Fixator and steel riser plate models were manually aligned with the fixator plate visible in microCT images. All masks were defined separately for each material (soft tissue callus, mineralized tissue, proximal and distal bone segments, fixator risers and plate, PCL mesh) and were combined to establish one unified

surface model. The unified surface mesh was then cleaned in 3Matic (Materialise) and converted to a volumetric mesh of quadratic tetrahedral elements. To determine mesh resolution, a convergence analysis was conducted. The 3rd principal strain within the defect soft tissue converging within 6% was designated as the criteria for sufficient mesh resolution (Figure 9A).

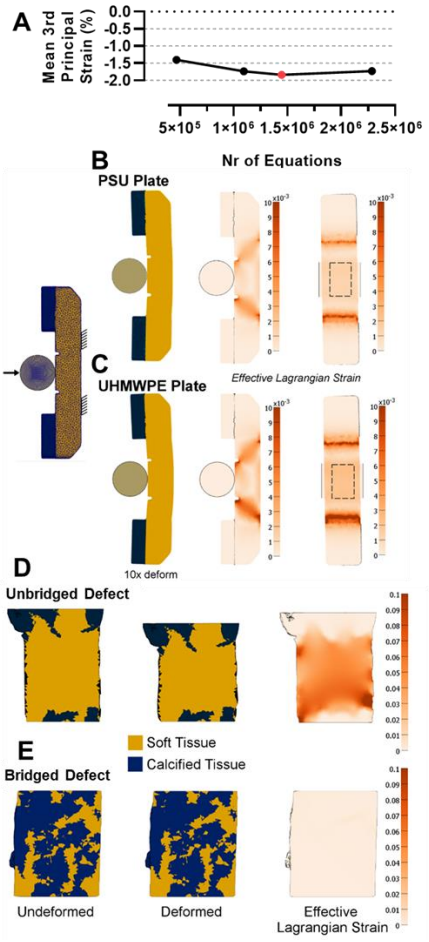

Figure 9: Finite element simulation development. (A) Femur-fixator finite element models were meshed using quadratic tetrahedral elements at increasingly refined resolutions until soft tissue 3rd principal strain converged. The red data point denotes the mesh resolution used here, where meshes consisted of approimately1.5M equations. Fixator mechanical properties were validated to match experimental three-point bending tests for both (B) PSU and (C) UHWMPE. Similarly, defect soft tissue and mineralized tissue mechanical properties were validated to match ex vivo experimental compression testing of (D) unbridged and (E) bridged defects.

A summary of material properties applied to the femur-fixator model is listed in Table 4. When available, material properties were assigned based on known properties (e.g., steel, cortical bone). The elastic moduli for the UHMWPE and PSU materials in the fixator were iteratively determined by matching model calculated reaction forces to those calculated during a three-point bending experiment (Figure 9B-C). Similarly, elastic moduli for soft tissue callus (Figure 9D) and mineralized tissue (Figure 9E) were also matched to experimentally determined displacements. Briefly, femora with an unbridged defect (Figure 9D) or a bridged defect (Figure 9E) were excised, potted in Wood's metal and tested in uniaxial compression with a ramp to 0.2 mm and 5.3 N, respectively. All materials were modeled as homogeneous neo-hookean materials with a single elastic coefficient (E) and poisson's ratio (ν). Mineralized tissue elastic coefficients within the defect were assumed to be related to the density of independent voxels to a power of 1.49. A scalar factor was then multiplied to this relationship and adjusted to match the model-derived with the experiment-derived displacements.

Table 4: Chapter 4 finite element model mechanical properties

Material	E (MPa)	ν
Intact cortical bone	18000	0.33
Intact trabecular bone	500	0.33
Soft defect tissue*	0.022	0.4
Mineralized defect tissue*	$0.000246*(\text{arbitrary density units})^{1.49}$ approximately 160-1700	0.33
PCL tube	1.44	0.37
PSU fixator*	844	0.37
UHMWPE fixator*	525	0.4
Steel anchor plate	200000	0.3

**Denotes properties validated by FE simulation to match experimental data*

The boundary conditions assigned to the femur-fixator model were implemented to best reflect in vivo loading as determined by Wehner and colleagues[183]. The distal femoral surface was fixed in all directions. Compressive and bending pressures, below, were applied to the cortical bone of the proximal surface (assumed to be 0.45 mm thick). Elemental pressures were formulated as a function of the medial-lateral and anterior-posterior position of each proximal surface element and a single scalar factor. The scalar factor *A* was then iteratively modified until the average axial Lagrangian strain in the sensor region of the fixator matched the in vivo strain amplitude for the respective animal at 2 weeks. All finite element analyses were completed using FEBio (version 2.8.5) and analyzed in PostView[199].

4.2.12 Statistical analysis

Sample sizes for treated groups were chosen based on a priori power analysis of prior mechanical loading model experiments. All statistical analyses were performed using Prism 7 (GraphPad), except multivariate linear regression, which was performed using SPSS 24 (IBM). Normality of data was tested using Shapiro-Wilk test. Fixation plate stiffness and sensor sensitivity were assessed by Student's t-test and Pearson's linear regression, respectively. Two-way ANOVA with Tukey's or Sidak's pairwise comparisons were used to compare groups for longitudinal strain, microCT, and gait analyses. Bonferroni comparisons were used to assess pairwise differences in vascular thickness distribution. Proportions of bridged defects were evaluated by chi-square test for trend, with pairwise comparisons assessed by individual chi-square tests. Non-parametric Mann-

Whitney U or Kruskal-Wallis tests were used to evaluate non-normally distributed data torsion and vascular morphometric data. Spearman's rank-order correlations were used to assess relationships between early strains and longer-term bone volume and strength. Data are displayed as mean ± s.e.m. or as box plots showing 25th and 75th percentiles, with whiskers extending to minimum and maximum values, unless otherwise noted in the figure heading.

4.3 Results

4.3.1 Real-time and on-demand ambulatory monitoring of in vivo mechanical boundary conditions across bone defects using an integrated strain sensor

To assess the relative effects of mechanical loading on bone repair, we used an established rat femoral bone defect model with well-characterized healing kinetics[200]. The critically-sized 6 mm defects received one of two treatments: 2 μg bone morphogenetic protein-2 (BMP-2), a minimal osteogenic dose that typically results in defects at the threshold of mineralized bridging at 8 weeks, or left empty as non-healing negative controls. The mechanical environment under ambulatory loads was perturbed by stabilizing defects with either stiff or moderately compliant internal fixation plates (fixators) which possessed a modular bridging segment fabricated from polysulfone (PSU) or ultra-high molecular weight polyethylene (UHMWPE), respectively. Our previous work in this model demonstrated that early ambulatory loading in a highly axially compliant fixator which was 80% more compliant than stiff PSU fixators drastically inhibited bone and vascular repair due to excessive deformation[34]. In this study, we sought to explore a more moderate mechanical environment that could enhance bone regeneration. Therefore,

compliant UHMWPE fixators featured a flexural stiffness about 40% lower than stiff PSU counterparts of identical geometry (Figure 10A; UHMWPE = 145.2 ± 10.6 N/mm & 525 MPa, PSU= 232.4 ± 20.1 N/mm & 844 MPa). The full study timeline is outlined in Table 5.

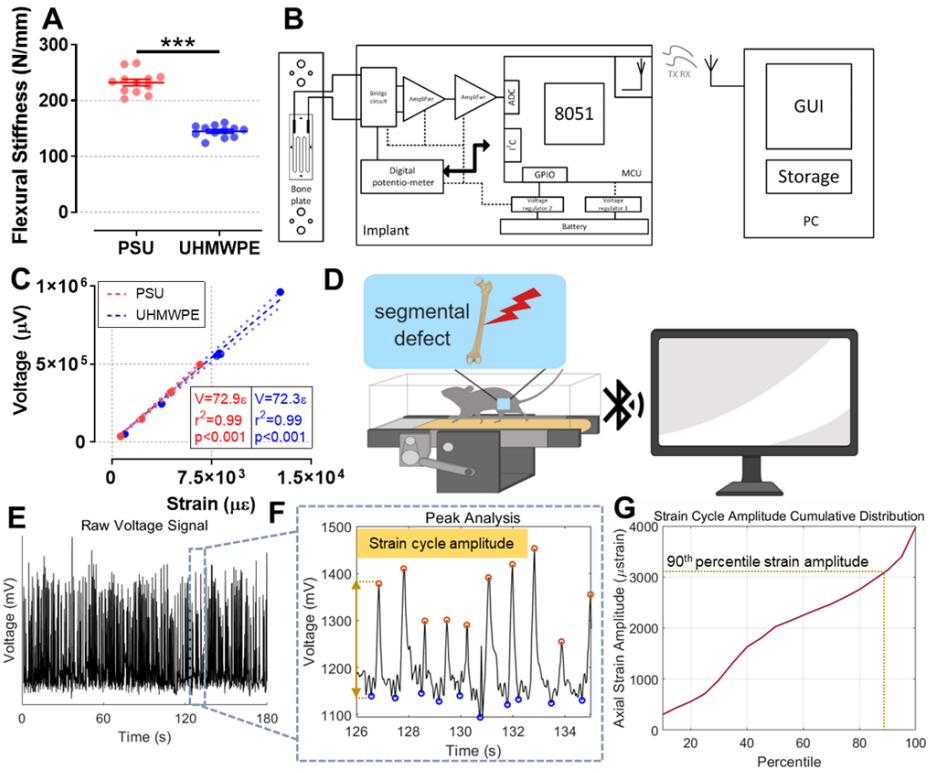

Figure 10: Real-time and on-demand ambulatory monitoring of in vivo mechanical boundary conditions across segmental bone defects using an integrated strain sensor. **(A)** UHMWPE fixation plates possessed a flexural stiffness 40% lower than PSU. n = 12. ***p < 0.001 via t-test. **(B)** Functional block diagram depicting fixator-mounted strain sensor interfaced with intra-abdominal transceiver unit consisting of analog front-end, MCU, GPIO, and BLE interface providing transmit and receive functionality with a host computer. **(C)** Representative electromechanical calibrations for UHMWPE and PSU fixators, strain sensors exhibited high linearity and precision. n = 20 cycles per strain. r^2 > 0.99, ***p < 0.001 via Pearson's. **(D)** Rats walked on a treadmill twice weekly 7 days after surgical creation of a unilateral segmental femoral defect and strain measurements were acquired in real-time. **(E)** Experimental sensor output during a 3 minute recording of rodent gait **(F)** Inset of sensor output depicting individual strain cycles corresponding to discrete steps and corresponding amplitudes. **(G)** Experimental cumulative distribution of strain cycles recorded during a treadmill session, indicating the 90th percentile amplitude.

In vivo strain measurements were facilitated via the integration of a strain sensor into the polymeric bridging segments of each fixator. The sensor transmitted real-time uniaxial strain measurements to a remote laptop with a USB receiver up to five meters away via a Bluetooth Low Energy (BLE) enabled digital transceiver (Figure 10B). The transceiver was remotely controlled to either transmit data or enter a low-power receiving mode by commands from the computer, enabling on-demand user control of data collection and power allocation. All devices exhibited linear responses and sufficient sensitivity to detect applied strain throughout the physiological dynamic range (Figure 10C).

Table 5: Bone repair in vivo study timeline. Experimental measurements and associated time points.

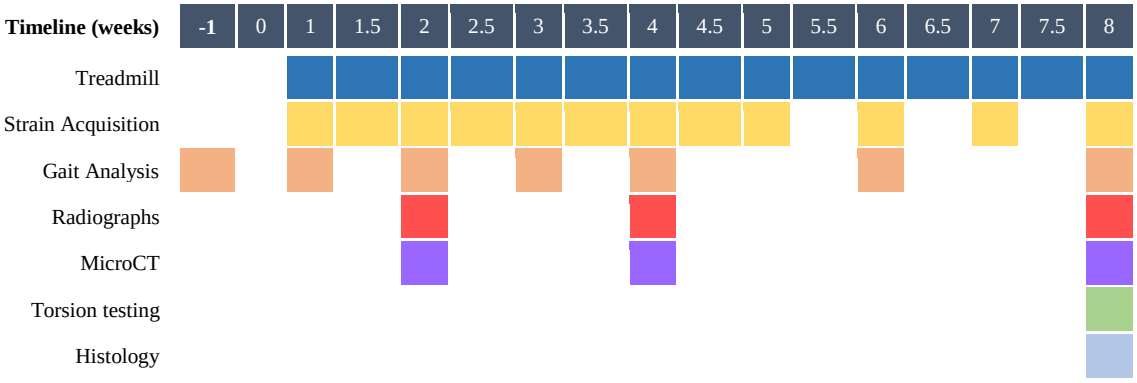

Ambulatory loading is a promising and straightforward approach to administer dynamic biophysical stimuli to the regenerative niche and enhance tissue repair[194]. Therefore, we sought to assess the temporal progression of mechanical cues imparted during slow walking by measuring strain during treadmill sessions starting one week after surgery and continuing twice weekly thereafter. Strain acquisition proceeded biweekly through 5 weeks and once weekly thereafter (Figure 10D). Dynamic strain cycle

amplitudes corresponding to individual steps were computed and ranked by magnitude (Figure 10E-G). The 90th percentile strain magnitude was tracked longitudinally as it represented a threshold of the 50-60 highest magnitude strain cycles, a sufficient number of cycles to provoke an adaptive cellular response[134,179,201]. Rehab collection periods represented the most significant mechanical stimulus exerted on the femur in terms of both magnitude and frequency content; treadmill walking produced a significant 60% increase in strain magnitude relative to nocturnal in-cage activity (Figure 11). To demonstrate real-time strain measurements during ambulatory activity with high temporal resolution, high-speed x-ray video of an animal walking on a treadmill during simultaneous strain acquisition was recorded one month after surgery (Figure 12). Video analysis demonstrated variations in strain signal were synchronized with stance and swing phases of walking, where stance phases produced a transient flexural strain on the fixator, conferring a compressive environment on the healing tissue. These data demonstrate the utility of implantable sensor technologies to remotely quantify mechanobiological cues within regenerating in vivo environments at meaningfully protracted time points after implantation.

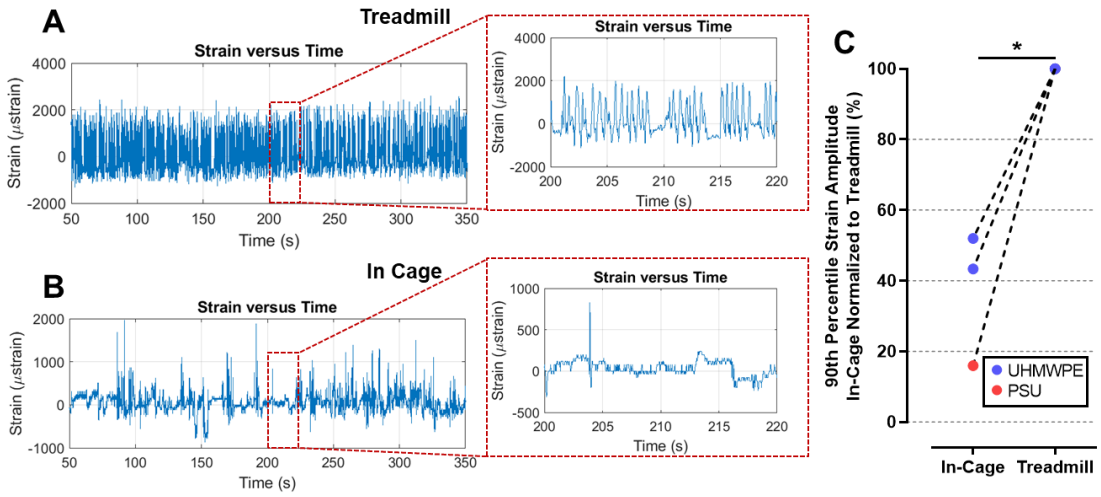

Figure 11: Treadmill walking is greater mechanical stimulus than in-cage activity in terms of both magnitude and frequency. Representative experimental strain measurements from the same animal acquired during **(A)** treadmill walking **(B)** and ad libitum nocturnal in-cage activity the same night. **(C)** 90th percentile strain magnitudes during treadmill activities were 60% higher than corresponding nocturnal in-cage activities. n = 3. *p < 0.05 via paired t-test.

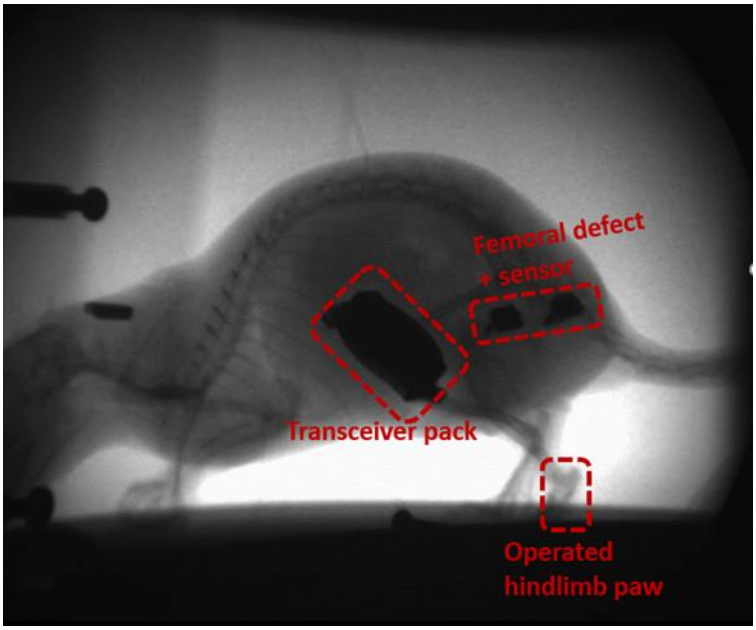

Figure 12: Annotated still image of high-speed X-ray video. Dotted boxes delineate the femoral defect, corresponding hindlimb paw, and transceiver pack.

4.3.2 Rehabilitative load sharing increased mechanical stimulation and accelerated bridging of segmental bone defects

Sensor measurements of longitudinal in vivo strains confirmed that compliant UHMWPE fixators permitted higher magnitude mechanical stimulation in vivo. Initial strain magnitudes were increased by approximately two-fold compared to stiff PSU fixators (Figure 13A; UHMWPE = 4760 ± 566 με, PSU = 2134 ± 277 με). Strain magnitudes did not change appreciably throughout the 8 week study in empty defect non-healing controls, regardless of fixator stiffness. Strain magnitudes on defects treated with a low dose of BMP-2 and stabilized by compliant UHMWPE fixators diverged from corresponding UHMWPE empty controls beginning at 2 weeks and continued to decline gradually until converging with levels observed in stiff PSU fixators. A similar decline was not observed in BMP-2 treated defects stabilized by PSU fixators, which showed no significant changes throughout the duration of the study. Serial radiographs corroborated our hypothesis that the progressive strain decline observed in UHMWPE fixators was due to bridging of mineralized tissue across the segmental defect, consequently reducing load share carried by the fixator (Figure 13B & C). Between weeks 2 and 4, the average strain magnitude in the UHMWPE group was halved from 5408 ± 704 με to 2698 ± 567 με, coinciding with a marked 64% increase in the percentage of bridged defects.

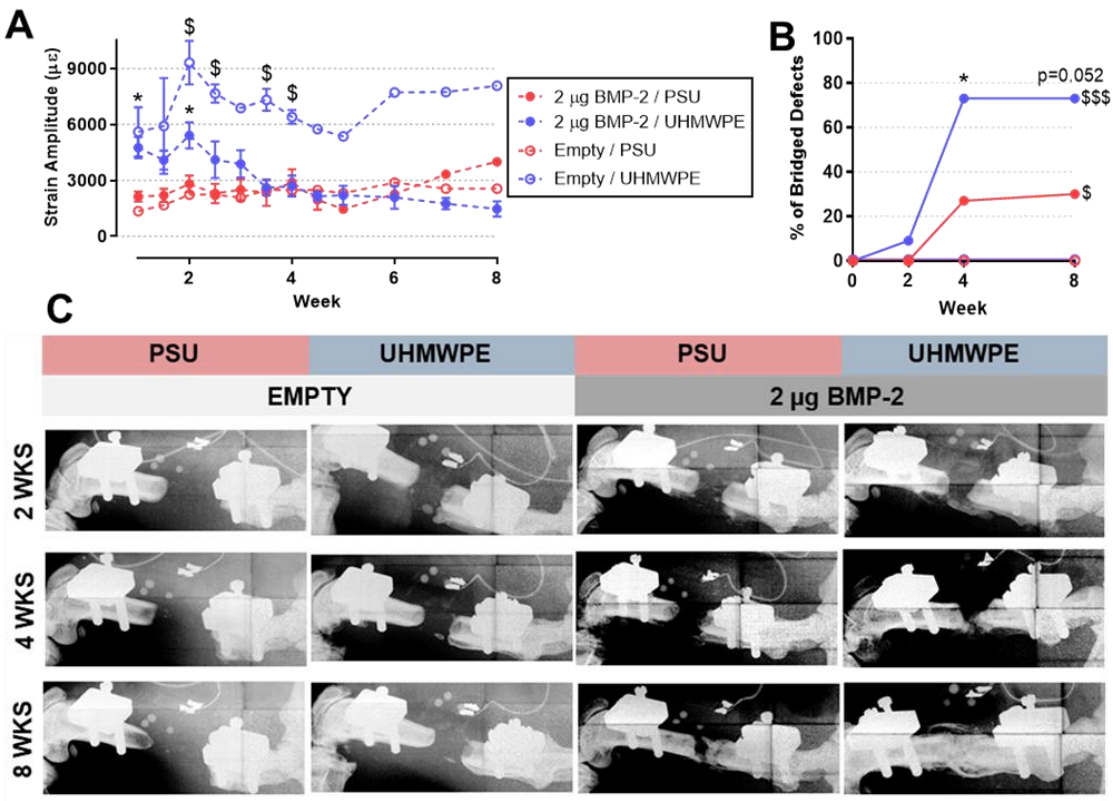

Figure 13: Rehabilitative load sharing initially increased mechanical stimulation and accelerated bridging of segmental bone defects. (A) Longitudinal strain amplitude measurements verified UHMWPE fixation permit increased mechanical stimulation of bone defects. n=1-9. 2 μg BMP-2: *$p < 0.05$ UHMWPE vs. PSU. UHMWPE: \$$p < 0.05$ Empty vs 2 μg BMP-2 via Two-way ANOVA with Tukey's test. **(B)** Longitudinal analysis of bone bridging via in vivo microCT segmented at 50% intact cortical bone mineral density. n = 10-11. *$p < 0.05$ differences between groups via chi-square test. \$$p < 0.05$ significance of trend via chi-square test for trend. **(C)** Representative longitudinal x-ray images for each group, demonstrating substantially increased mineralization with compliant UHMWPE fixators in the presence of BMP-2.

A fundamental motivation for developing the strain sensor platform was to elucidate dynamic mechanical boundary conditions in a healing skeletal defect and to identify specific ranges that could enhance repair. Radiographic comparisons between groups demonstrated that rehabilitative load sharing permitted by UHMWPE fixators significantly accelerated bridging and enhanced total mineralization in the presence of BMP-2. Bridging ratios were nearly tripled in UHMWPE stabilized defects compared to

PSU at 4 weeks. Empty non-healing controls confirmed that negligible mineralized tissue developed without intervention in this critically-sized defect model irrespective of fixation stiffness, which correlates with a similar lack of temporal variation in strain magnitude. Facilitated by the implantable strain sensor, these data support the potential for controlled biophysical signals imparted by normal movement activities to accelerate tissue regeneration in challenging injuries.

4.3.3 Bone regeneration was enhanced by ambulatory mechanical loading and initial strain magnitudes correlated with improved healing outcomes

We performed serial in vivo microcomputed tomography (microCT) scans to quantitatively assess the effect of the mechanical environment on bone formation. In agreement with the radiographic data, we observed a beneficial effect of mechanical loading on bone regeneration (Figure 14A). Compliant UHMWPE fixation had significant overall effects on bone volume, trabecular thickness, trabecular number, and trabecular separation (Figure 14B; D-F); at the 8 week time point bone volume and trabecular thickness in the UHMWPE group were significantly increased by 63% and 47%, respectively, compared to stiff PSU fixators. Mineral density and polar moment of inertia were not affected by load sharing (Figure 14C & Figure 15), suggesting that the early stage effects of mechanical stimulation are mediated primarily by accumulation of relatively centralized woven bone volume rather than acceleration of bone remodeling and mineral densification, processes whose kinetics may act over longer time spans. Picro Sirius Red histological analysis of 8 week tissue samples supported that UHMWPE fixation supported a mixture of woven and lamellar extracellular matrix (ECM), whereas PSU fixation exhibited primarily lamellar ECM (Figure 16). Ex vivo torsion testing to failure yielded no

significant effects on failure strength, though a single high-performing statistical outlier stabilized by PSU may have obscured the results, albeit this sample had no experimental observations to warrant exclusion (Figure 14G).

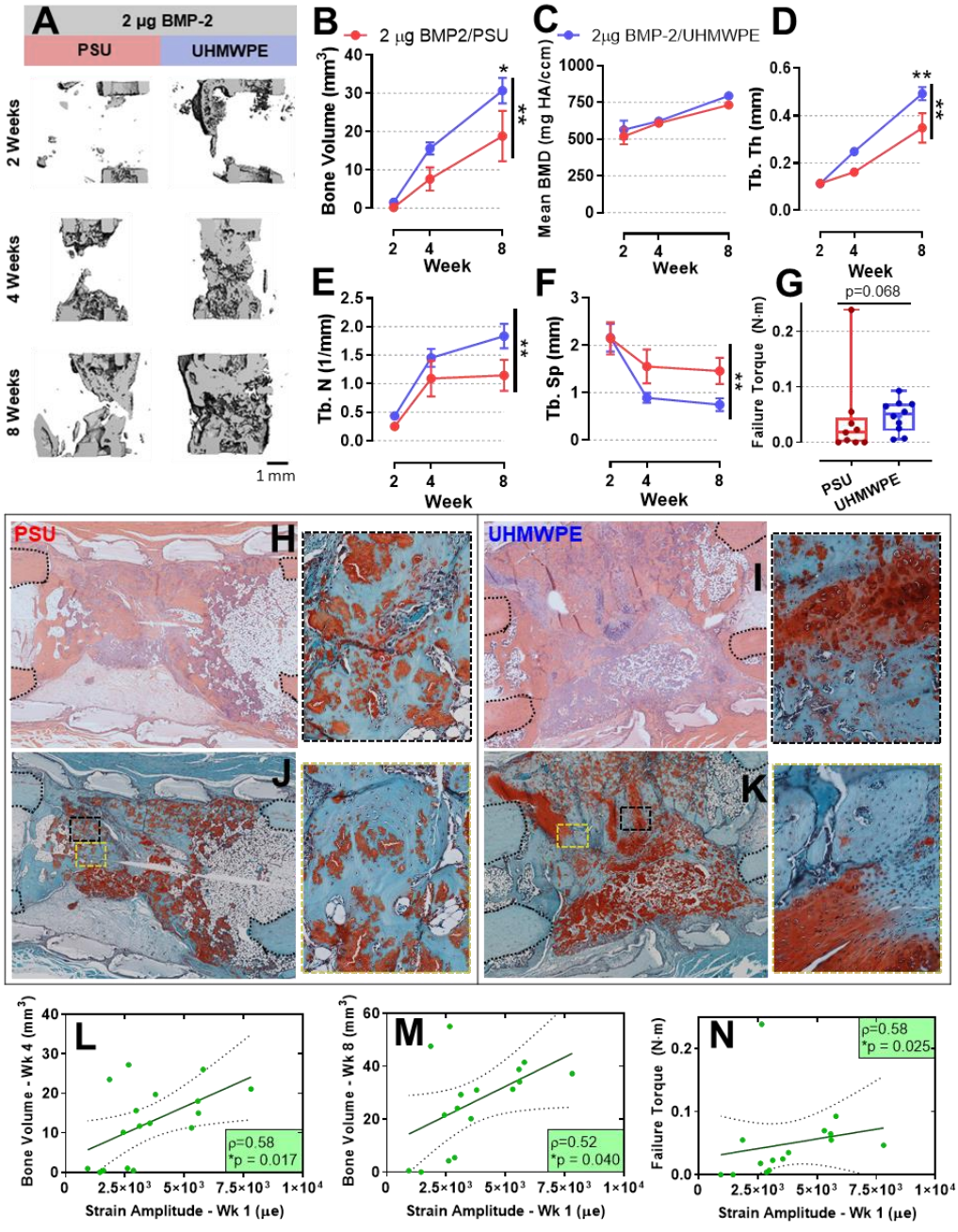

Figure 14: Bone regeneration was enhanced by ambulatory mechanical loading and initial strain amplitudes correlated positively with improved healing outcomes. (A)

Bone defect microCT reconstructions representing median samples, showing increased mineralization with compliant UHMWPE fixation. Scale bar, 1 mm. Longitudinal microCT quantifications of **(B)** bone volume, **(C)** mean bone mineral density, **(D)** trabecular thickness, **(E)** trabecular number, **(F)** trabecular spacing demonstrating increased architectural parameters and no effects on mineral density with compliant UHMWPE fixators. n = 10-11. Vertically oriented bar ** $p < 0.01$ overall main effect UHMWPE vs. PSU via Two-way ANOVA. Overhead asterisks * $p < 0.05$, ** $p < 0.01$ via Sidak's multiple comparisons test. **(G)** Failure torque of explanted femoral defects 8 weeks after surgery. n = 10-11. $p = 0.068$ via Mann-Whitney U test. **(H-I)** Week 8 H&E-stained histological sections showing intact femoral ends (black dotted lines) and increased mineralized tissue formation under compliant UHMWPE fixation. **(J-K)** Week 8 Safranin-O/Fast green sections demonstrate extensive regions of hypertrophic chondrocytes and endochondral bone formation under compliant UHMWPE fixation. Scale bars, 500 µm for full defect and 50 µm for insets. Specimen-specific strain amplitudes during the first treadmill activity period at 1 week, before appreciable mineralization had occurred, exhibited significant positive correlations with **(L)** 4 week bone volume, **(M)** 8 week bone volume **(N)** and 8 week failure torque. n = 17. *$p < 0.05$ via rank-order correlation.

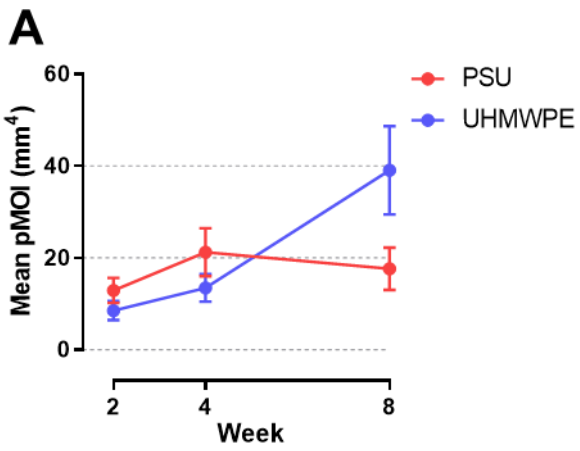

Figure 15: Longitudinal microCT quantification of additional morphometric parameters. (A) Mean polar moment of inertia was not significantly affected by fixator stiffness. n = 10-11. Vertically oriented bar **$p < 0.01$ overall main effect UHMWPE vs. PSU via Two-way ANOVA.

Histological analysis of the 8 week samples revealed direct contact between the regenerating tissue and biomaterial irrespective of fixation stiffnesses, with regions of mineralized tissue surrounding remnants of alginate hydrogel (Figure 14H-I). Safranin-O/Fast green staining indicated that compliant UHMWPE fixation exhibited extensive

regions of hypertrophic chondrocytes and endochondral ossification throughout the bone defect, while chondrocytes were observed to a qualitatively lesser extent with PSU (Figure 14J-K). These data are supported by prior reports that moderate mechanical loading primarily mediates osteogenesis via endochondral bone formation, the primary mechanism for long bone formation and fracture repair under load-bearing conditions[34,50,130,179].

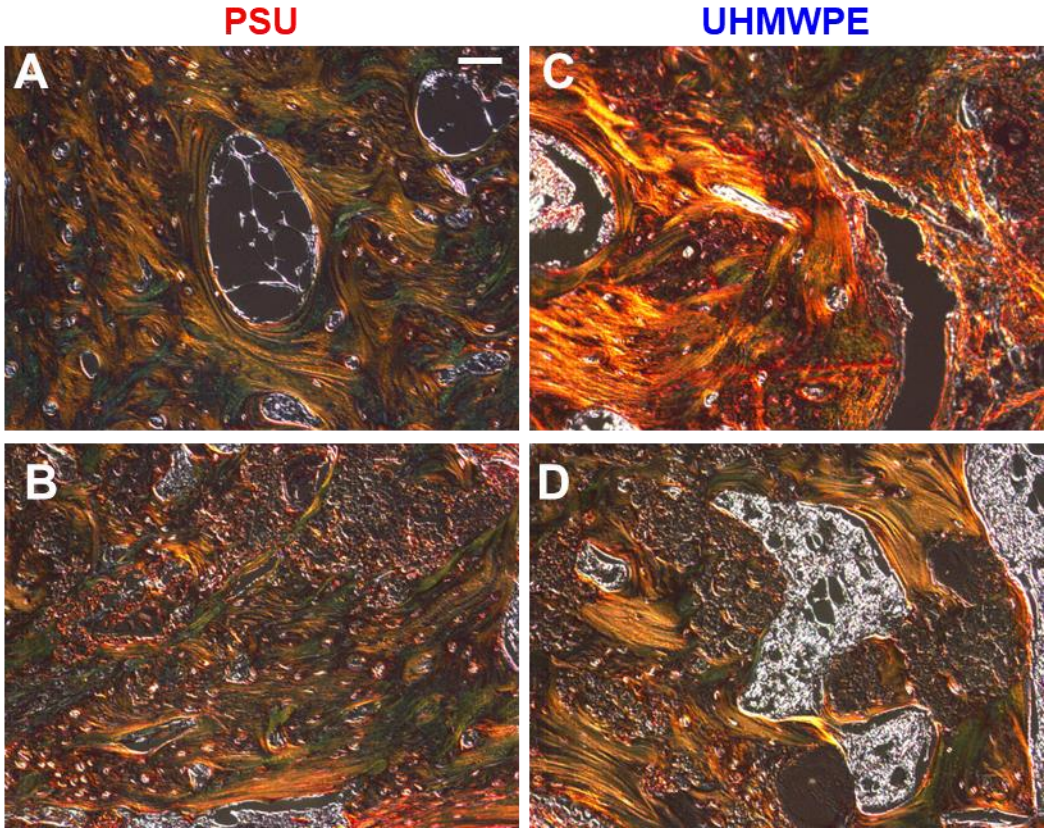

Figure 16: Extracellular matrix organization. Histological images of Picro Sirius Red stained sections at 8 weeks viewed under polarized light. (A-B) Defects stabilized by stiff PSU fixators exhibited primarily lamellar ECM possessing a mix of green and yellow/orange collagen fibers, indicative of a mixture of both smaller and larger fibers, respectively. **(C-D)** Defects stabilized by compliant UHMWPE fixators possessed a range of ECM organizations. **(C)** Large and intense yellow/orange collagen fibers were visible, indicative of newly formed woven bone and pronounced matrix remodeling. **(D)** In addition, regions with more organized green and yellow/orange fibers analogous to PSU samples were also apparent. Scale bar, 50 μm.

The significant enhancement of bone regeneration stabilized by UHMWPE fixation supported further inquiry into the therapeutic potential of early, moderate mechanical stimulation. To evaluate this effect more carefully, we examined the relation between initial strain amplitudes and longer-term healing outcomes on a per animal basis to investigate if slight inter-animal variations in strain correlated with differential healing outcomes at disparate time points. Rank-order correlation revealed a significant positive relationship between strain cycle amplitude at week 1 and bone volume at weeks 4 and 8 and failure torque (Figure 14L-N). This correlation with tissue strain was no longer significant at 2 weeks (Figure 17A-C); radiographic shadowing and mineralization had already begun by 2 weeks (Figure 13B & C, Figure 14A), potentially stiffening those defects which were on a favorable progression toward regeneration.

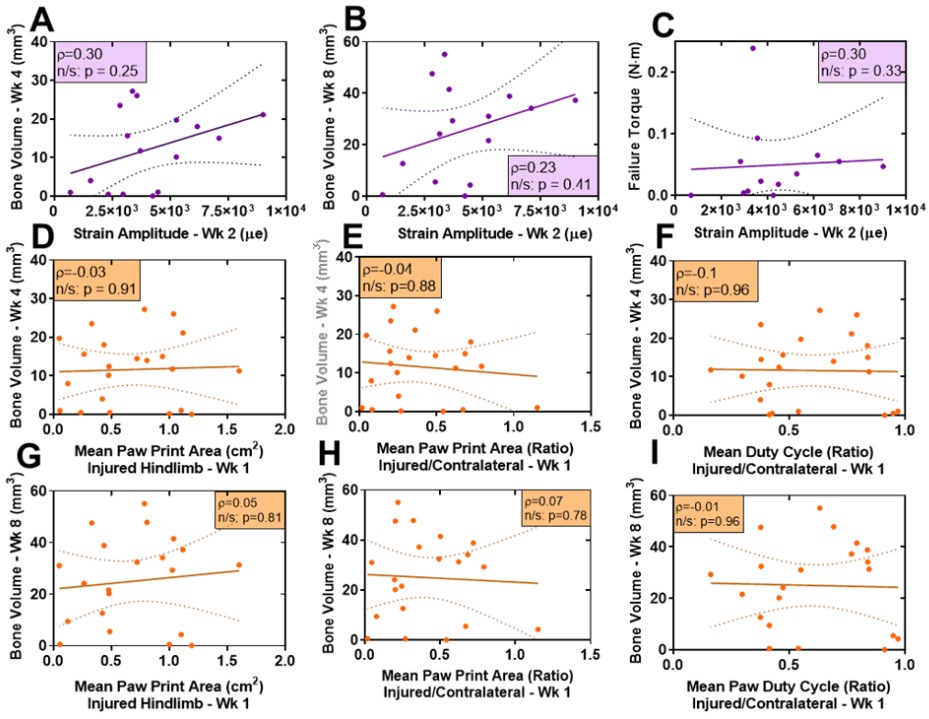

Figure 17: Later time point strain amplitudes and initial gait analysis metrics do not correlate with healing outcomes. Strain amplitudes acquired at 2 weeks no longer

correlated significantly with **(A)** 4 week bone volume, **(B)** 8 week bone volume **(C)** and 8 week failure torque, as mineralization had initiated thereby stiffening defects with a favorable prognosis. n = 16. n/s via rank-order correlation. Gait analysis metrics at 1 week including mean paw print area of injured hindlimb and injured to contralateral ratios of mean paw print area and duty cycle also did not correlate with 4 week **(D-F)** or 8 week **(G-I)** bone volume, respectively, indicating that animals with increased gait deficits were not predisposed toward poor healing outcomes. n = 21-22. n/s via rank-order correlation.

An alternative but plausible interpretation of the data was that animals that were not recovering well from surgery were consequently not loading their operated hindlimb, and their poor prognosis for recovery was instigating lower strain amplitudes. However, this hypothesis was not supported, as initial gait analysis metrics representing operated hindlimb recruitment during walking revealed no relationships with bone volume or failure torque (Figure 17D-I). Additionally, all animals recovered well from surgery with no visible signs of post-operative distress. These results suggest that early stage dynamic mechanical stimuli may play a persistent role in the healing progression and have the potential to influence tissue repair at later-stage time points.

4.3.4 Strain magnitudes correlated with gait function and healing status

Another potential beneficial application for the sensor platform is to provide a non-invasive readout of the progression of healing. We hypothesized that the magnitude of fixation plate deformation would primarily be dictated by three factors: the force input on the operated femur during each step cycle, and the apparent stiffness of both the fixator and the adjacent bone defect, which share load as parallel deformable bodies. To obtain an indirect estimate of the hind limb force, we assessed the degree of operated hind limb utilization via weekly quantitative gait analysis immediately after treadmill rehabilitation periods. We observed significant deficiencies in mean paw print area and duty cycle of the

operated hindlimb relative to the naïve contralateral initially after surgery, with no relative effects of fixator stiffness (Figure 18A & B). These deficits were gradually restored to pre-operative levels within 6 weeks.

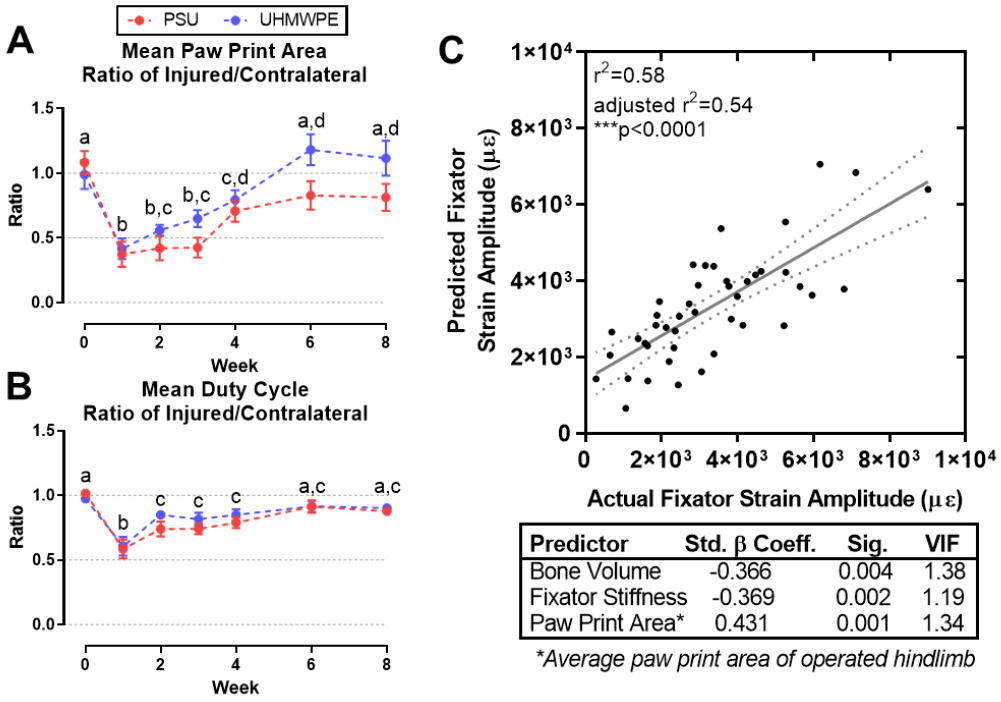

Predictor	Std. β Coeff.	Sig.	VIF
Bone Volume	-0.366	0.004	1.38
Fixator Stiffness	-0.369	0.002	1.19
Paw Print Area*	0.431	0.001	1.34

**Average paw print area of operated hindlimb*

Figure 18: Strain magnitudes correlated with gait function and healing status. Longitudinal gait analysis quantifications for ratio of operated hindlimb over naïve contralateral for mean **(A)** paw print area **(B)** and duty cycle demonstrating substantial gait deficits are present 1 week after surgery and are progressively resolved by 6 weeks. n = 10-11. Differing letters denote significant differences $p < 0.05$ via Two-way ANOVA with Tukey's test. **(C)** Regression model of pooled ambulatory strain measurements across all imaging time points demonstrate strain magnitude is predicted by a linear combination of bone volume, fixator stiffness, and mean paw print area. n = 44. Adjusted $r^2 = 0.54$, ***$p < 0.0001$ via multiple regression.

To evaluate the accuracy of our simplified working model for fixator strain magnitude, we performed forward selection and backward elimination multivariate linear regression on a response variable data set consisting of all strain measurements acquired at time points with corresponding microCT scans (ranging from 2-8 weeks). The predictor

variable pool consisted of the fixator stiffness of each device, bone volume, and gait analysis metrics. The optimal predictive model was identical for both directions and highly significant. Lending support to the working model, experimental inputs predictive of fixator strain magnitude consisted of negative correlations with bone volume and fixator stiffness, and a positive correlation with average paw print area of the operated hind limb (Figure 18C). The three predictor variables exhibited low collinearity (VIF $\leq$ 1.38) and a maximal adjusted coefficient of determination overall, signifying parsimony. Together, these data help to describe the key biomechanical relationships within the long bone healing environment and demonstrate the potential for strain-based readouts to provide real-time assessment of mineralization progress during controlled functional activities without the use of X-rays.

4.3.5 Tissue-level compressive strains at 2 weeks were significantly elevated with compliant fixation

While the strain sensor provides a quantitative readout of axial strain on the fixator stabilizing the defect, the effects of mechanical stimulation are ultimately mediated by the tissue-level biophysical environment within the regenerative niche. To investigate this, we used the experimental data to inform image-based computational models of the early-stage bone defect mechanical environment. In this experimental system, the deformation measured on the fixation plate during gait provided an experimentally validated in vivo boundary condition for the fixator-femur system at 2 weeks (Figure 19A-B). Using sample-specific boundary conditions and microCT geometry of the defect tissue, we observed a dramatic increase in the magnitude of the 3rd principal strain, the maximum compressive local strain, within the defect soft tissue under compliant UHMWPE fixation (Figure 19C-

D). The defect tissue was largely load-shielded by PSU fixation, with 85% of the tissue undergoing less than 0.5% compressive strain (Figure 19E). Conversely, load sharing permitted by UHMWPE fixation produced a much wider distribution of local tissue strain encompassing larger compressive magnitudes up to 6.7%. The average strain magnitude under UHMWPE was substantially elevated compared to PSU, and the interquartile ranges scarcely overlapped (Figure 19F; UHMWPE: -0.3% to -3.0% vs. PSU: -0.1% to -0.4%). These data further demonstrate the utility of the implantable strain sensor platform to identify general tissue-level dynamic strain magnitudes that promote bone formation before appreciable mineralized bridging has occurred.

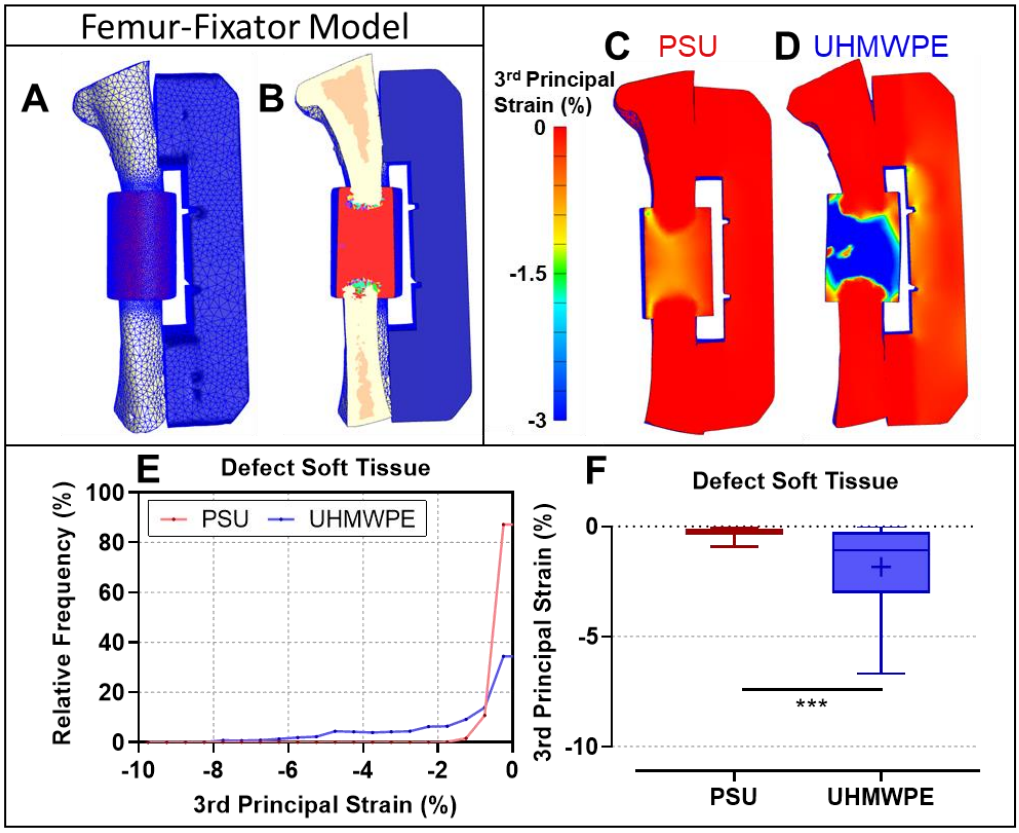

Figure 19: Tissue-level compressive strains at 2 weeks were significantly elevated **with compliant fixation. (A)** To assess the early-stage tissue-level mechanical environment produced by the differing fixators, microCT-based finite element models of representative

samples stabilized by UHMWPE and PSU at 2 weeks were developed. Specimen-specific boundary conditions were validated using in vivo strain sensor measurements. **(B)** Cross-sectional view of finite element model, brightly colored elements in the defect zone represent immature woven bone. Local strain map of defects stabilized by **(C)** PSU **(D)** UHMWPE fixators reveal substantially elevated compressive strains throughout unmineralized tissue in the defect. **(E)** Histogram and **(F)** box plot further demonstrate significant increase in compressive local tissue strains permitted by compliant UHMWPE fixation. n > 16,000 elements with whiskers extending from the 2.5 to the 97.5 percentile values. ***p<0.001 via Mann-Whitney U test.

4.4 Discussion

Physical forces critically regulate collective cell behavior during transient healing processes[189]. However, dynamic forces are challenging to characterize in vivo, precluding a clear understanding of how external mechanical cues may be exploited therapeutically to enhance repair. Here, we sought to investigate the temporal progression of mechanical signals in a regenerating orthotopic site and to evaluate the biomechanical and therapeutic effects of a load sharing-inspired approach on bone regeneration. To this end, we integrated an implantable sensor platform into internal fixators of differing stiffness, creating an in vivo bone repair model in which we could perturb and remotely quantify mechanical boundary conditions in real-time during ambulation. We hypothesized that moderately compliant UHMWPE internal fixators would permit increased strain across the defect during gait relative to stiffer PSU and consequently enhance bone repair in a challenging critically-sized long bone defect small animal model. The results showed that load-sharing permitted by UHMWPE fixators initially delivered a two-fold increase in deformation magnitude, subsequently increased mineralized bridging by nearly three-fold, and increased bone formation by over 60% (Figure 13A-C & Figure 14A & B). Furthermore, by coupling in vivo imaging with strain sensor data as experimentally validated in vivo boundary conditions, we quantified differences in the early stage tissue-level mechanical

environment mediated by reduced fixator stiffness (Figure 19). Together, these results establish the utility of in vivo telemetric sensing approaches to aid in the measurement of tissue healing and outcomes after regenerative therapeutics. Additionally, the present study demonstrates that early stage physical stimuli exert potent effects on these healing outcomes and that the judicious use of rehabilitative loading activities informed by real-time biomechanical measurements may have the potential to resolve skeletal injuries more effectively.

At the tissue level, the benefits of mechanical stimulation to skeletal repair have been largely established using percutaneous and bulky external fixator frames; with these systems loads are applied via manual adjustment, actuators, or spring systems, but the invasiveness of such approaches substantially limits their utilization[50,137]. At the cellular level, mechanical stimulation is known to differentially regulate a wide array of mechanisms critical to tissue regeneration including mesenchymal stromal cell differentiation and migration[58,85] and vascular formation and remodeling[34,60]. Together, data from large and small animal models implicate certain mechanical cues may enhance bone repair in a strain magnitude and healing stage dependent manner[179]. Invasive external loading systems applying non-physiological loading patterns have indicated that relatively small early compressive strains (3-7%) support early callus precursor formation and woven bone formation[50,176]. Early-stage deformation exceeding 10-15% has been implicated to inhibit vascularization and cause fibrotic non-union or fracture the newly formed bone bridge, though in vivo strains were not actually measured[26,34]. The defect stiffens by several orders of magnitude as mineralization and bridging occurs allowing larger magnitude loads to be exerted while resultant tissue strains decrease; osteogenic strain magnitudes on newly

formed woven are well established to be approximately 0.1-0.4% and can accelerate mineralization and vascular maturation after the interfragmentary gap has already bridged with calcified tissue[34,62,201–203]. Taken together, the mechanobiological regulation of bone (re)modeling after bridging is well established. However, the magnitude of and functional effects of physiological mechanical cues imparted by rehabilitative activity like walking during early phases, prior to the establishment of bridging or non-union, remains poorly understood. Clinically, it would be beneficial to leverage the potential of local mechanical therapies via early loading, since later stage interventions offer limited benefit to vulnerable cases at risk of non-union. Due to the lack of understanding of early loading and technologies to quantify it in vivo, current rehabilitation protocols for fractures treated with open reduction and internal fixation are typically non-weight bearing for 6-12 weeks[204].

An alternative mechanobiological strategy is to introduce mechanical cues into the regenerative niche non-invasively via ambulatory activities. In addition to direct biophysical stimulation of the skeletal defect, rehabilitative exercise may exert second-order benefits to peripheral tissues injured during trauma or surgery including surrounding muscles and nerves[193,194]. Randomized clinical trial evidence has shown that supervised progressive resistance exercise after proximal hip fracture enhances physical function and quality of life compared to low-intensity exercise targeting flexibility for elderly patients[192]. However, the actual mechanical environment imparted by rehabilitative activity, such as resistance training, within a bone defect has not been quantified longitudinally, impeding a generalized understanding of tissue-level mechanical stimuli with the potential to augment regeneration. The in vivo experimental system that we developed and used in the studies herein allowed us to longitudinally measure dynamic

axial strain during gait. Concurrently, we observed a substantial enhancement in bone repair via increased load sharing. These data implicate a critical role for early mechanical cues on the long term healing response as strain cycle magnitude at 1 week (before appreciable healing occurred) had a significant positive correlation with the long-term bone regeneration outcomes (Figure 14L-N).

While fixator strain measurements were useful to assess differences between groups and temporal trends reflective of healing, mechanical cues transmitted to cells within the healing tissue ultimately regulate mechanobiological responses. Given the potent longer-term osteogenic effects of early-stage loading under compliant UHMWPE fixation, we reasoned that quantifying the tissue-level deformation provided a more generalizable understanding of dynamic mechanical cues that accelerate early-stage bone repair, irrespective of the fixator. Subject-specific, image-based finite element analysis revealed that tissue-level compressive strain within the bone defect at 2 weeks ranged from 0.1-6.7% under UHMWPE fixation, whereas stiffer PSU fixation shielded the entire defect, permitting only 0.1-0.9% strain. These data are consistent with the results of Miller et al., who reported that local maximum compressive strains of about 3% resulted in peak probability of subsequent mineralization between days 7 and 14 using an invasive percutaneous loading system in a rat osteotomy model[176]. Miller and colleagues further showed that the probability of fibrous tissue formation surpasses mineralization when compressive strains exceed 8%. The results from this study corroborate the osteogenic nature of early-stage tissue strains below 7% using a completely implantable telemetric system and leveraging ambulatory activity to non-invasively deliver mechanical cues. Together, the data reported here support the hypothesis that mechanobiological responses

to ambulatory loading can be therapeutically exploited to accelerate bone repair, and further research is warranted to investigate how controlled rehabilitation regimens may be safely enacted relatively early after surgical intervention.

In addition to the mechanobiological findings facilitated by the strain sensor platform, the data support that future iterations of strain sensing approaches may have promising applications in clinically relevant contexts such as diagnostics and rehabilitative monitoring. While not the primary impetus for the sensor platform developed in this model, the results provide proof of principle as strain amplitudes during gait gradually declined over time in healing defects. The magnitude of a given strain measurement was a function of the volume of mineralized tissue in the defect, the degree of hindlimb usage, and the fixator stiffness (Figure 18C). Therefore, this study provides pre-clinical in vivo evidence that it may be feasible to infer the status of bone healing via measurements acquired under a repetitive controlled task without the need for X-rays. Such an approach is pertinent to pediatric patients after procedures that would typically entail CT imaging, as radiation exposure should be curtailed to minimize risk of radiation-induced cancers[205]. This idea has been explored of late in percutaneous devices to measure strain and tissue impedance[168,206], but emerging developments in passive and active devices could offer fully implantable, wireless embodiments[207]. In addition, we obtained measurements in real-time while animals walked on a treadmill. Such an approach could provide real-time feedback to guide rehabilitative specialists while patients perform functional activities, enabling patients to maximize recovery of function after surgery while ensuring hardware safety thresholds are not exceeded.

The sensor platform does have limitations that warrant further research. Though sufficient for implantation in a relatively small rat model, the size of the fully-packaged transceiver (38 mm x 23 x 12 mm) would benefit from miniaturization. The primary contributor to the size was the coin-cell battery, which was selected for its relatively high power density and sufficient theoretical power budget for an 8 week study. Nonetheless, transceiver attrition was unexpectedly high in the initial bone repair study, reaching 33% and 83% by 3 and 8 weeks, respectively. Explant testing indicated this was due to variability in voltage regulator performance. Improvements to the transceiver voltage regulator in the follow-up angiography study substantially increased device reliability. Attrition was reduced to a single failed device (6% failure rate) at 3 weeks, where the root cause was due to fixator loosening and not electrical malfunction. Additional work toward circuit board layout and power consumption optimization would substantially reduce device size and improve power budget fidelity. Passive approaches for power input and data transfer are a promising avenue for sensor miniaturization in certain contexts, but require externally mounted inductive coil elements, have reduced transmission range, and are sensitive to variation in coil-pair orientations. Together, these are significant limitations to monitoring during dynamic movements. For these reasons, we employed an active BLE telemetry approach that permitted straightforward sleep-wake control and parallel data acquisition from multiple animals walking at once. Despite the size of the transceiver, it is worth noting that the current footprint is than sufficient for large animal and human scale hardware research.

The specific objective of this study was to assess the role of the tissue-level mechanical environment on regeneration. Treadmill walking at a constant speed was

employed as a relatively controlled ambulatory activity with which to impart mechanical stimulation for all groups. Therefore, the net contribution to tissue repair of periodic walking relative to cage restriction was not targeted, but warrants further investigation. Forced walking may cause stress and confounding systemic effects in small animals[194]. The findings of this study motivate the development of experimental rehabilitative protocols that better mimic clinical regimens in both small and large animal models to improve translation of insights obtained by in vivo strain sensing platforms to humans, similar to the methods of Dalise and colleagues studying aerobic exercise in rats[208].

Here, we implemented an implantable sensor platform to monitor how mechanical stimulation of the regenerative niche permitted by reduced stiffness fixation promotes bone repair. In this study, in vivo strain monitoring enabled observations that: 1) early strain amplitudes correlated with healing outcomes before radiographic indications of healing were apparent, and that 2) local strain magnitudes within the regenerative nice between 1-7% significantly enhanced bone regeneration. By facilitating real-time longitudinal characterization of in vivo mechanical cues, the data represent a notable advancement in regenerative mechanobiology. The capacity of integrated biomedical sensors to remotely quantify dynamic mechanical signals throughout musculoskeletal regeneration offer new opportunities to investigate mechanisms by which biophysical cues augment tissue repair. With continued research, similar sensor approaches have the potential to provide instantaneous clinical feedback for physicians and physical therapists to aid implementation of safe and effective rehabilitation regimens optimized for restoration of tissue structure and function.

CHAPTER 5. EFFECTS OF MECHANICAL LOADING ON EARLY STAGE NEOVASCULARIZATION AND CYTOKINE SIGNALING

5.1 Introduction

In CHAPTER 4, we deployed the strain sensor platform developed in CHAPTER 3 to investigate the longitudinal progression of mechanical cues and bone regeneration within segmental defects undergoing differing degrees of load sharing. We observed that early stage load sharing imparting tissue levels strains between 2-7% significantly enhanced bone regeneration in a magnitude dependent manner. Interestingly, we observed that strain magnitude 1 week after injury positively correlated with long term bone repair, suggesting that the progression of bone defect repair is altered by mechanical loading at early stages in the healing cascade. These early stages can be defined as the acute interval of bone repair prior to substantial mineralized bridging and bone remodeling. Therefore, the early stage encompasses immune signaling, angiogenesis, soft callus formation and early mineralization (CHAPTER 2.2). In this chapter we investigated the effects of mechanical loading on critical biological processes that coordinate early stage bone regeneration.

Bone is a dynamic tissue whose development and maintenance are heavily influenced by biomechanical stimuli exerted by load-bearing activities. After fracture, bone possesses a significant intrinsic capacity for tissue regeneration and restoration of critical biomechanical functions. However, approximately 5% of the millions of fractured bones

each year result in nonunions, where the bone defect does not heal effectively from the initial treatment and remains mechanically unstable[3]. The prolonged disability and multiple surgeries endured by such patients therefore represent a substantial global health burden[209]. New therapeutic options to stimulate bone regeneration after injury are needed to address this issue. In particular, regenerative therapies are needed for individuals suffering from segmental bone loss due to tumor resection or severe traumatic injuries, as intrinsic repair mechanisms cannot restore large volumetric defects without the introduction of osteogenic or osteoinductive biomechanical or biochemical cues[210].

Given the potent mechanosensitive regulatory mechanisms present in bone[172,211], the integration of rehabilitative exercise and natural load-bearing activity into treatment regimens represents a promising cost-effective, non-pharmacologic approach to stimulate bone repair after injury[126,130,179,194]. We previously developed a novel implantable strain sensor platform to quantify mechanical cues in rat femoral segmental defects during rehabilitation and observed that controlled delivery of mechanical stimulation via early ambulatory loading can significantly enhance bone regeneration outcomes (CHAPTER 4). Furthermore, we observed a significant positive correlation between strain magnitudes at 1 week with long term healing outcomes, suggesting potent magnitude-dependent effects of mechanical stimulation on early stages of bone repair. However, the underlying early-stage biological effects of this mechanical environment are not yet understood.

Early stages of effective bone repair are facilitated by the coordinated action of diverse cell types over rapid time scales after injury or surgery. Several processes preceding defect mineralization are vital to osteogenesis, including immune cell recruitment, cytokine signaling, and angiogenesis. As the defect size increases, early stages of repair may be

temporally protracted as cells migrate over longer distances to fill the defect. Initially, a diverse population of myeloid and lymphoid lineage immune cells including neutrophils, monocytes, macrophages, and T cells infiltrate the defect site to clear pathogens and necrotic debris, remodel the extracellular matrix (ECM), and secrete cytokines to recruit mesenchymal and endothelial progenitors into the defect[15,212]. Neutrophils have a short life span and typically undergo apoptosis within the first several hours, while monocytes rapidly differentiate into macrophages in response to environmental cues within the healing niche[212,213].

Macrophages are perhaps the most established immune cell phenotype involved in the coordination of multiple phases of bone repair[213–215]. Macrophages and macrophage-lineage cells are a functionally diverse population known to mediate phagocytosis, granulation tissue formation, vascular anastomosis, and production of a range of inflammatory, osteogenic and angiogenic cytokines including interleukin-1β (IL-1β), bone morphogenetic protein-2 (BMP-2), LIX (CXCL5), and vascular endothelial growth factor (VEGF)[213,215–219]. Macrophages function on a continuum, but are classically segmented into M1 and M2 polarization phenotypes; where M1 are associated with phagocytosis and acute inflammatory paracrine signaling over the first several days after injury, and M2 are implicated in later stages of immune response including fibroblast stimulation, protease expression, and suppression of inflammation[213]. Depletion studies indicate that macrophages are indispensable to fracture healing, as both transgenic and clodronate liposome-induced macrophage depletion abrogates endochondral and intramembranous bone repair in mice, though the specific contributions of M1 or M2 phenotypes remains unclear[214,215,220].

As immune cells resolve acute inflammatory signals, angiogenic and osteogenic paracrine cues mediate the next phase of bone repair typically during the first several weeks after injury. Effective bone regeneration is reliant on sufficient revascularization of the defect region via angiogenesis of nearby vasculature[221]. Vascularization, must reach a sufficient threshold to provide oxygen and nutrients to support metabolic demands of bone formation and (re)modeling or non-union will occur[33]. Angiogenesis after injury in vivo occurs as an underdamped adaptive response, where exuberant revascularization of injured tissue initially exceeds physiological demands[31,222]. However, vessel number and volume are tightly regulated and excess vessels are pruned during later stages of tissue repair as superfluous vessel formation can actually compromise efficient tissue perfusion[222,223].

It is well known that bone repair outcomes are heavily regulated by mechanical loading. However, data are scarce describing how vital biological mechanisms of bone repair prior to mineralization, including immune modulation and vascularization, are affected by extrinsic forces present in orthotopic healing environments. Macrophage polarization has been modulated by altering cytoskeletal interactions with the surrounding matrix in two-dimensional cultures[224]. Further, monocytes respond to fluid shear and compressive stresses by increasing production of pro-inflammatory cytokines in agarose gel cultures[225]. Additionally, vascular networks have been shown to be mechanosensitive where growth and alignment of microvessels in three-dimensional cultures were modulated significantly by tensile strain[60]. Overall, in vitro results provide preliminary evidence that both immune mediators and angiogenesis are mechanosensitive; however, in vitro systems do not recapitulate the cellular and molecular complexity of the regenerative niche in vivo. Several animal studies have demonstrated that severe rotational or axial instability lead to

delayed bone repair or non-union and also increase the presence of cytotoxic T cells, inhibit angiogenic gene expression, and abrogate defect revascularization. In contrast, the effect of more clinically relevant and osteogenic mechanical loading protocols remain unclear[16,200,226]. We recently used a wireless implantable strain sensor to demonstrate that bone repair was significantly enhanced due to dynamic strain imparted by ambulatory load sharing initiating 1 week after injury (CHAPTER 4). Consistent with prior literature, we observed elevated endochondral ossification at 8 weeks in response to load sharing (CHAPTER 4)[50], however the underlying biological response to loading at earlier stages are unknown. Overall, little has been investigated regarding the fundamental effects of potentially therapeutic mechanical cues on the coordination of early stage bone repair.

To address this, here we evaluated the effects of mechanical loading on early stage cytokine signaling, angiogenesis, and tissue structure in vivo. Our overarching objective was to investigate how key aspects of the regenerative response were modulated by osteogenic mechanical strain in vivo. Prior studies in the rat femoral segmental defect model used in this study demonstrated that vascular volume under stiff fixation peaks at 2 weeks and appreciable mineralization begins to occur at 3 weeks[200,227]. Thereafter, excess vessels are progressively pruned while remaining vessels mature via dilation and arteriogenesis[34,227]. Therefore in this study, we examined cytokine expression during peak vascularization (2 weeks), and the status of vascularization at the onset of mineralization (3 weeks). Given prior research has demonstrated that excessive loading dramatically increases inflammatory signaling[16], we hypothesized that osteogenic mechanical stimulation would elevate inflammatory cytokine expression to a more moderate degree while supporting sufficient vascularization to promote endochondral bone repair.

5.2 Methods

5.2.1 Surgical procedure

All animal procedures were approved by the Georgia Institute of Technology IACUC (Protocol A17034). Two animal studies were conducted using identical injury, treatment, and rehabilitation procedures described below. The experimental designs for the studies lasting 2 and 3 weeks post-surgery, respectively, are outlined in Table 6 and Table 7. The 3 week study concluded with terminal microCT angiography. The second study concluded 2 weeks post-surgery with multiplex cytokine analysis of the newly formed tissue in the bone defect. Histological and immunohistochemical (IHC) analyses were conducted using samples from both time points.

Table 6: Bone angiography in vivo study timeline.

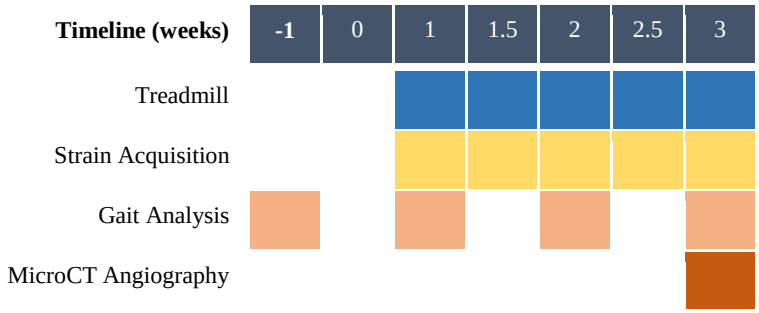

Table 7: Experimental timeline for defect tissue cytokine expression study.

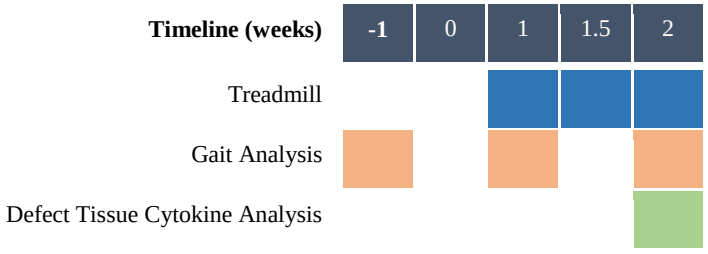

Similar to previously described procedures, a unilateral 6 mm segmental defect was surgically created in the left femur of 15 week old female CD Sprague-Dawley rats (n=24, Charles River Labs)[181]. Anesthesia was maintained by isoflurane inhalation and analgesia was provided by a pre-operative subcutaneous injection of sustained-release buprenorphine. Before creating the defect with an oscillating saw, femurs were stabilized by affixing a radiolucent internal fixator plate comprised of either polysulfone (PSU, McMaster-Carr), or ultra-high molecular weight polyethylene (UHMWPE, Quadrant) using four stainless steel screws. UHMWPE fixators were 40% more compliant than PSU (flexural stiffness: PSU = 232 ± 20 N/mm; UHMWPE = 145 ± 11 N/mm). Fixators in the 3 week vascularization study contained integrated wireless strain sensors that provided real-time non-invasive measurements of mechanical strain across the bone defect during ambulatory activity, as previously described (CHAPTER 4.2.1). Fixators in the 2 week defect tissue cytokine analysis study were stabilized by fixators without strain sensors. In both animal studies, defects were acutely treated with a minimal healing dose of recombinant human bone morphogenetic protein 2 (BMP-2) delivered via a hybrid RGD-alginate/PCL biomaterial platform described in detail elsewhere[182,197]. Briefly, treatment consisted of installing an electrospun polycaprolactone (PCL, Sigma-Aldrich) tube across the defect gap, then injecting 120 µL alginate hydrogel laden with 2 µg BMP-2 (Pfizer) inside the tube. Fixators were allocated randomly. After either 2 or 3 weeks, animals were anesthetized then euthanized via CO_2 asphyxiation.

5.2.2 Treadmill walking

To exert a semi-controlled ambulatory mechanical load on the femur, animals were walked on a treadmill. Animals were trained to walk at a slow, consistent speed of 6.5

m/min 1 week prior to surgery. After surgery, animals were allowed to recover in cages for 1 week, then 10 minute walking periods were initiated at day 7 and continued twice weekly thereafter. During the 3 week angiography study, axial strain across the bone defect was measured non-invasively for 3 minutes during each treadmill rehabilitation period by recording measurements via each wireless strain sensor implant. The distance traversed during this period roughly approximates the best available estimate of the total distance covered during one day of in-cage activity[198].

5.2.3 Gait analysis

To measure how animals were using their operated hindlimb under voluntary walking conditions, gait was analyzed longitudinally. Gait capture and analyses were conducted 1 week prior to surgery (baseline) and 1 and 2 weeks after surgery using a Catwalk 7.1 system (Noldus). Briefly, rats walked freely across an illuminated walkway and individual illuminated paw prints were captured by a digital camera. Passes where the animal traversed the entire length of the runway in less than 10 seconds were analyzed (2-3 runs per animal). Individual paw prints were automatically categorized then verified and corrected manually, when necessary. The ratio of the operated hindlimb to naïve contralateral paw print area and duty cycle were quantified.

5.2.4 MicroCT angiography

Vascular perfusions were performed after 3 weeks in the angiography study according to previously described protocols[228]. Animal vasculature were sequentially perfused through the ascending aorta with 0.9% saline, 0.4% papaverine hydrochloride vasodilator, 0.9% saline, 10% neutral buffered formalin (NBF), 0.9% saline, and

radiopaque lead chromate contrast agent (2:1; Microfil MV-22, FlowTech Inc.). Samples were stored overnight at 4° C to ensure polymerization, and both operated and naïve femora were dissected with surrounding musculature left intact. Samples were submerged in a formic acid/citrate decalcifying solution (Newcomers Supply) for 10 days on a rocker plate with daily solution changes.

MicroCT scans were performed using 15 µm voxels, 55 kVp, 145 µA, and 300 ms integration time. Vascular formation and morphology was assessed inside two different 4.14 mm long cylindrical VOI: a 5 mm diameter "Defect VOI" encompassing the interior of the PCL tube in operated femora or the approximate central axis of the femur in naïve contralateral samples, and a 7 mm diameter "Total VOI" encompassing the bone defect and immediate surrounding tissue. Vasculature was segmented using a Gaussian low-pass filter and a global threshold.

5.2.5 Analyses of defect tissue cytokines

Animals were euthanized 24 hours after the final week 2 treadmill period. Defect tissue inside and adhered to the outside of the PCL tube was immediately and carefully harvested. Upon dissection, two samples were excluded from analysis due to evidence of tissue abscess near the fixator indicative of infection. Individual tissue samples were flash frozen in liquid nitrogen and then stored at -80º C for subsequent Luminex multiplexed immunoassays. Samples were thawed and homogenized in RIPA lysis buffer (Thermo Fisher) supplemented with 1X Halt protease inhibitor cocktail (Thermo Fisher). Lysates were centrifuged at 13,000 g for 15 minutes and supernatants were transferred to new tubes and stored at -80º C. A panel of 27 cytokine were quantified using a Milliplex

MAP Rat Cyotkine/Chemokine Magnetic Bead Panel according to the manufacturer's instructions and then read using a MAGPIX instrument (Luminex). Cytokine concentration was normalized to total protein content quantified using a bicinchoninic acid assay (BCA assay, Thermo Fisher). The sample sizes for each group were: UHMWPE = 9 and PSU = 11.

5.2.6 Histology and immunohistochemistry

At the endpoint of each study (weeks 2 and 3, respectively), representative femur samples were reserved for histological analysis based on digital radiographs acquired immediately before euthanasia. Femora were fixed in 10% neutral-buffered formalin for 48 hrs at 4º C, and switched to PBS after. HistoTox Labs completed decalcification, paraffin processing, and staining. Midsagittal 5 µm thick sections were stained with Hematoxylin & Eosin (H&E), Safranin-O/Fast Green, or Picro Sirius Red.

IHC was performed on tissue sections to assess the presence of macrophages in the defect. M1-like macrophages were defined as CD11b+/CD68+/CD163-, while M2-like macrophages were defined as triple positive CD11b+/CD68+/CD163+[213,229–231]. The following antibodies were used: CD11b (1:50; Thermo Fisher #12-0110-82), CD163 (1:50; Bio-Rad #MCA342F), and DAPI (1:1000; Invitrogen #D3571).

5.2.7 Finite element analyses

Sample-specific finite element (FE) models of the femur-fixator construct were constructed at 1 and 3 weeks using similar methods described previously (CHAPTER 4.2.11). Briefly, microCT images were processed in MIMICS (Materialise) to create a

representative model of proximal and distal femur segments with the fixator attached. At 1 week, defects were assumed to be a homogeneous 5 mm diameter cylinder comprised of soft tissue. For 3 week models, pre-decalcification microCT geometry of mineralized woven bone (threshold = 388 mg HA/ccm) were included within the soft tissue cylinder of each femur sample. Volumetric meshes of quadratic tetrahedral elements were constructed. Mesh resolution convergence was previously demonstrated at approximately $1.5x10^6$ equations. All materials were constitutively modelled as neo-hookean solids and previously reported experimentally validated mechanical properties were assigned (Table 8, CHAPTER 4.2.11)[232].

Table 8: Chapter 5 finite element model mechanical properties.

Material	E (MPa)	ν
Intact cortical bone	$18x10^3$	0.33
Intact trabecular bone	500	0.33
Soft defect tissue[1]	0.022	0.4
Mineralized defect tissue[2]	36.2	0.33
PCL tube[1]	1.44	0.37
PSU fixator[1]	844	0.37
UHMWPE fixator[1]	525	0.4
Steel anchor plate	$200x10^3$	0.3

[1] *CHAPTER 4.2.11*
[2] *Leong & Morgan, 2009.*

In each model, animal-specific boundary conditions were defined based on axial strain measurements by the wireless strain sensor at the corresponding 1 or 3 week treadmill period. Similar to previously reported simulations, boundary conditions were applied to replicate in vivo loading[183]; the distal end of the femur was fixed in all directions and combined axial compression and bending pressures were applied to the proximal surface. All FE simulations were conducted in FEBio (version 2.8.5) and results were

evaluated in PostView[199]. To capture inter-animal variability of the complete data set while maintaining computational efficiency, a sub-set of animals (n=5 from each fixator group) were evaluated by longitudinal FE analyses at both 1 and 3 weeks, creating 20 FE simulations in total. The distribution of strain magnitude and woven bone volume were identical between the sub-set of animals and the complete experimental group (Figure 20).

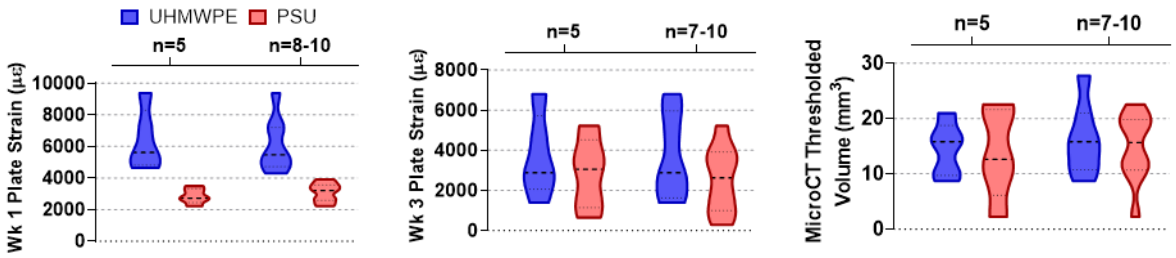

Figure 20: Finite element analyses were conducted on a sub-set of experimental samples representative of the complete data set. Longitudinal element analyses were conducted on 5 experimental samples from each experimental group. The magnitudes of strain at 1 and 3 weeks, as well as the thresholded tissue volume at 3 weeks of this were not different from the complete data set for each group.

5.2.8 Statistical analyses

Data are displayed as mean ± s.e.m. or as box plots showing 25th and 75th percentiles, with whiskers extending to minimum and maximum values, unless otherwise noted in the figure heading. Differences were assessed using t-test. Welch's t-test or Mann-Whitney U test was used in cases of unequal variances or non-normal distributions, respectively. Significance was determined using $p < 0.05$. Statistical tests were performed by GraphPad Prism 8.

Univariate and multivariate analysis of cytokine expression profiles within the defect were conducted to evaluate differences between fixator stiffness groups, as

described previously[233]. Univariate t-tests were performed comparing the normalized median fluorescence intensity values of individual cytokines. Discriminant partial least squares regression (D-PLSR) was performed using the PLS MATLAB (Mathworks) algorithm developed by Cleiton Nunes. Individual cytokine measurements were used as independent variables, and fixator stiffness was used as the discrete regression variable. Multi-dimensional latent variables (LV's) were defined in three dimensions, and an orthogonal rotation was implemented to assess separation by fixator stiffness in the LV1-LV2 plane. Standard deviation of individual cytokines along LV1 were computed using leave-one-out cross validation without replacement.

5.3 Results

5.3.1 Gait deficits after surgery were similar regardless of fixation stiffness

Quantitative longitudinal gait analysis revealed that animals' utilization of their operated hindlimb relative to the naïve contralateral hindlimb was significantly reduced after surgery (Figure 21). There was no effect of fixation plate stiffness on the gait deficits. No animals exhibited severe gait deficits in which the operated hindlimb was not used and thus none warranted exclusion.

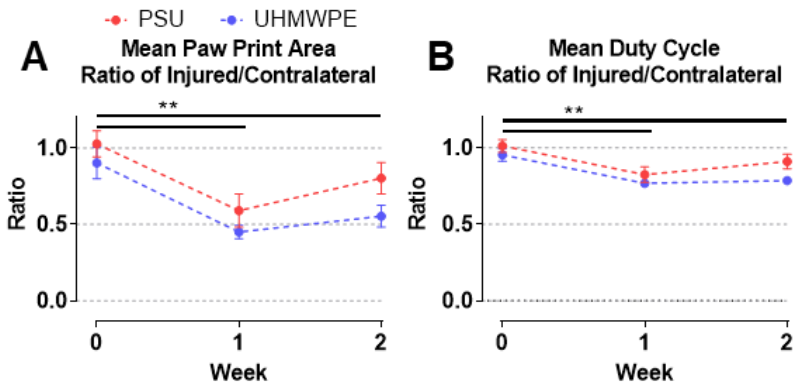

Figure 21: Gait analysis demonstrated moderate functional deficits in the defect hindlimb after surgery. Longitudinal gait analysis quantifications for ratio of operated hindlimb over naïve contralateral for mean **(A)** paw print area **(B)** and duty cycle demonstrating substantial gait deficits are present 1 week after surgery. n = 11-12. * $p < 0.05$ via Two-way ANOVA with Tukey's test.

5.3.2 Defect revascularization at 3 weeks was elevated by load-shielding stiff fixation

MicroCT angiography revealed that vascular volume within the defect volume was significantly increased under stiff PSU fixation at 3 weeks relative to compliant UHMWPE fixation or unoperated contralateral femora (Figure 22A). The vascular volume in defects stabilized by UHMWPE was similar to the contralateral. Changes in vascular volume mediated by fixation plate stiffness were only present within the defect volume, there were no differences between PSU and UHMWPE fixators in the total analysed volume or in the surrounding tissue alone (Figure 22B & C). Regardless of fixator stiffness, vascular volume surrounding the bone defects was significantly increased relative to unoperated femora, demonstrating excess angiogenesis after injury (Figure 22C).

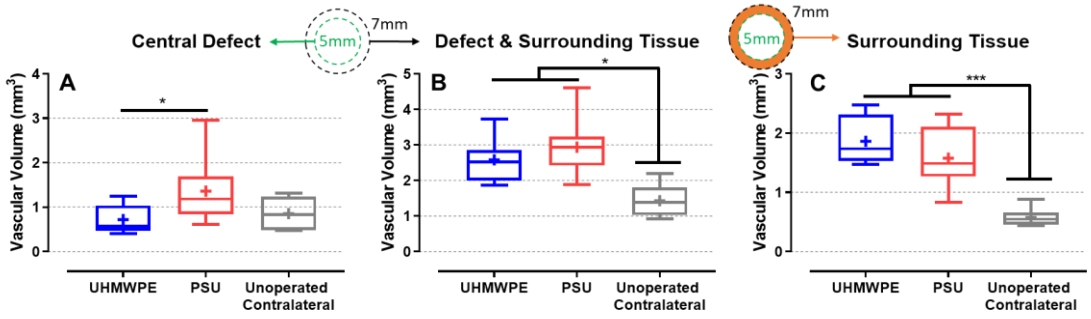

Figure 22: Vascular volume within the defect was increased at 3 weeks with stiff PSU fixation. MicroCT angiography quantification of vascular volume at 3 weeks in and surrounding bone defects. **(A)** Vascular volume within the central 5 mm of the defect is increased under stiff fixation, though compliant fixation remained similar to the intact femora. n=6-10. *p<0.05 via Kruskal-Wallis test with Dunn's pairwise comparisons **(B)** Vascular volume throughout the entire defect and surrounding tissue was elevated in injured femora relative to naïve, irrespective of fixation stiffness. n=6-10. *p<0.05 via ANOVA with Tukey's test. **(C)** In the surrounding tissue alone, vascular volume was similarly elevated in injured hindlimbs regardless of fixator. n=6-10. *p<0.05 via ANOVA with Tukey's test.

Representative microCT reconstructions of vascular perfusions qualitatively supported volume quantifications (Figure 23A-C). In vivo strain sensor measurements during gait replicated similar amplitudes and temporal trends as the preceding bone repair study (Figure 23J & Figure 13A), indicating the mechanical environment produced by rehabilitative walking was repeatable across studies. Regardless of fixator stiffness, we observed a significant increase in the amount of relatively small blood vessels (30-120 μm diameter) and the connectivity of the vascular network throughout the defect and surrounding tissue, demonstrating a potent angiogenic sprouting response to the injury and treatment with BMP-2 (Figure 23D & H). Neovessel orientation was significantly more isotropic compared to naïve vasculature, which was primarily aligned along the limb axis (Figure 23A-C, I).

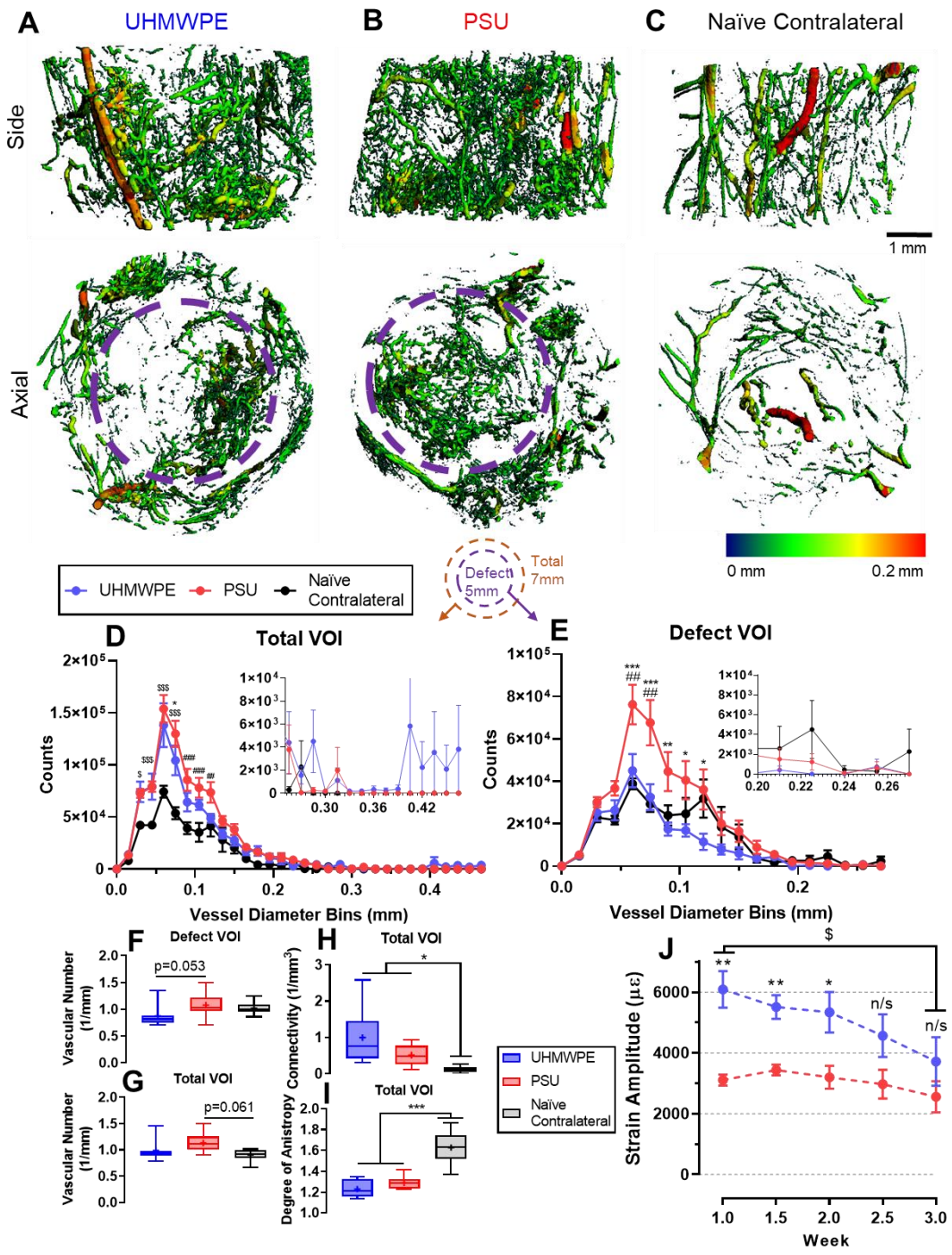

Figure 23: Defect revascularization at 3 weeks was elevated by load-shielding stiff fixation. Representative microCT reconstructions of blood vessels in the bone defect region at 3 weeks illustrate robust vascularization in operated hindlimbs stabilized by **(A)** UHMWPE and **(B)** PSU fixators relative to **(C)** naïve contralateral femora. Violet dashed circles delineate the location of the PCL tube, the interior of which is the Defect VOI. **(D)** Vascular thickness histograms demonstrate a significant increase in the presence of 45-90

μm thick blood vessels throughout the defect and surrounding tissue in operated femora, regardless of fixator stiffness, demonstrating pronounced angiogenesis in peripheral tissues in response to injury. **(E)** 60-120 μm thick blood vessels were significantly higher within defects stabilized by PSU fixators relative to the more compliant UHMWPE fixators. n=6-10. *p<0.05: PSU vs. UHMWPE, #p<0.05: PSU vs. naïve contralateral, $p<0.05: PSU & UHMWPE vs. naïve contralateral via Two-way ANOVA with Bonferroni pairwise comparisons. Vascular number in the **(F)** defect and **(G)** total VOIs, and **(H)** connectivity and **(I)** degree of anisotropy in the total VOI. n=6-10. *p<0.05 via Kruskal-Wallis with Dunn's test. **(J)** Longitudinal in vivo strain amplitudes replicated the preceding 8 week study, with an initial two-fold increase in deformation on UHMWPE fixators which steadily declined, converging with PSU strain amplitudes. n=7-10. Two-way ANOVA *p<0.05 UHMWPE vs. PSU with Tukey's test, $p<0.05 UHMWPE: week 1 vs 3 with Sidak's test.

Interestingly, when we localized the analysis within the confines of the defect we observed a significant increase in the number of relatively small vessels (60-120 μm diameter) within defects stabilized by PSU fixators relative to more compliant UHMWPE fixators (Figure 23E). The vessel size distribution of defects stabilized by UHMWPE more closely matched naïve vasculature. Furthermore, the number of distinct vascular structures within defects stabilized by PSU fixators was elevated (Figure 23F & G).

5.3.3 Increased strain magnitude altered cytokine expression profile within bone defects at 2 weeks

Defect tissue lysate was analyzed for an array of inflammatory cytokines. To distinguish multivariate cytokine expression profiles differentially regulated by defect tissue strain, discriminant partial least squares regression (D-PLSR) was performed. D-PLSR revealed that fixation plate stiffness groups primarily separated along the LV1 axis (Figure 24A). Defect samples stabilized by stiff PSU fixators scored significantly higher along LV1 relative to samples stabilized by compliant UHMWPE fixators (Figure 24B). "The LV1 axis represents a combination of cytokines that have been reduced in

dimensionality in order to maximally separate the data based on fixator stiffness. Based on the LV1 loading plot, we can determine which cytokines most contributed to positive and negative LV1 scores, which are associated with stiff and compliant fixation, respectively (Figure 24C). Cytokines most associated with stiff fixation were VEGF and IL-4 were, whereas expression of LIX (CXCL5), IL-1β, and RANTES (CCL5) were most associated with compliant fixation (Figure 25). Univariate pairwise comparisons demonstrated that LIX (CXCL5) levels were significantly elevated by compliant fixation. Conversely, VEGF expression was elevated by stiff fixation (p=0.052).

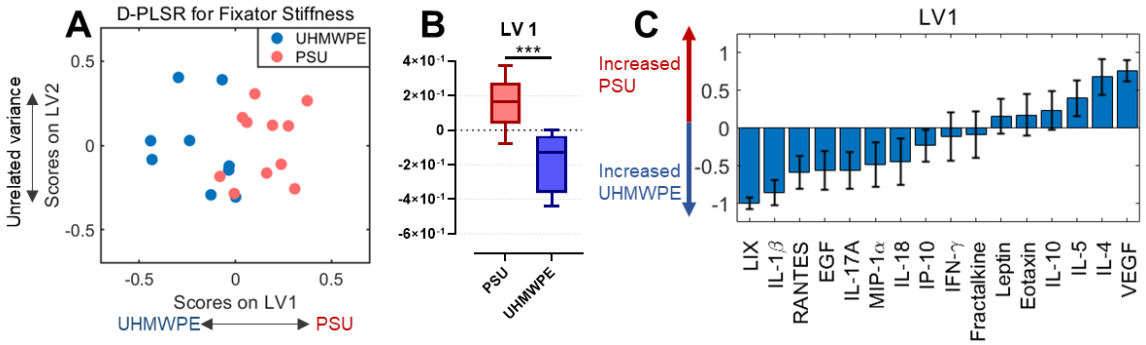

Figure 24: Increased strain magnitude altered cytokine expression profile in bone defect at 2 weeks. Discriminant partial least squares regression (D-PLSR) analysis of the expression of 16 cytokines in the defect tissue at 2 weeks. **(A)** Latent variable 1 (LV1) defines a multivariate cytokine expression profile depicted along the x-axis that separates defects stabilized by stiff PSU fixators to the right and compliant UHMWPE fixators to the left. **(B)** Mean LV1 score was significantly upregulated by stiff PSU fixation. n=9-11. ***p<0.001 via t-test. **(C)** Values along LV1 describe individual cytokines with elevated expression for UHMWPE fixation (negative values) or PSU (positive values). Error bars were computed using leave-one-out cross validation (mean ± SD).

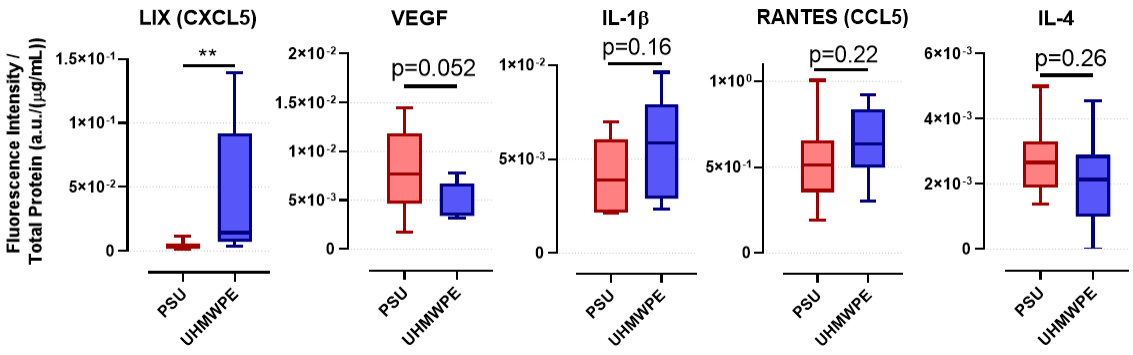

Figure 25: Univariate comparisons of individual cytokine expression in defect tissue at 2 weeks. LIX (CXCL5) expression was significantly increased by increased load sharing with compliant UHMWPE fixation. Conversely, VEGF expression was elevated with by load shielding with stiff PSU fixation. Significant pairwise differences were not observed in the remaining cytokines. n=9-11. **p<0.01 via t-test.

Non-supervised principal component analysis was also conducted on the cytokine expression profiles to test if samples still separated by fixation stiffness without providing experimental groups as discrimination inputs. Samples still significantly separated along principal component (PC) axis 2 (Figure 26A & B), and individual cytokine profiles up-regulated were similar to D-PLSR, where negative scores along PC2 were upregulated in stiff PSU fixation while positive scores were upregulated by UHMWPE fixation. VEGF and IL-4 were similarly elevated by stiff fixation, while RANTES (CCL5), LIX (CXCL5), and IL-1β were likewise elevated under compliant fixation (Figure 26C). These unsupervised results corroborate the significant separation of cytokine expression profiles regulated by defect tissue strain revealed by D-PLSR.

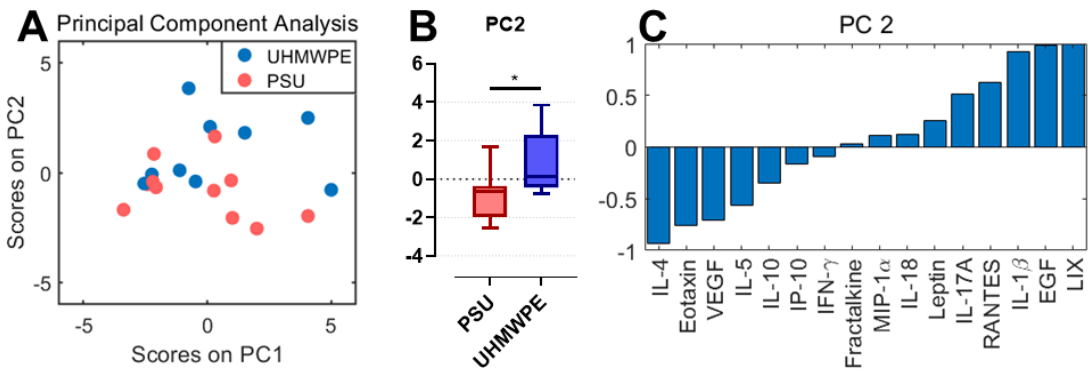

Figure 26: Unsupervised principal component analysis (PCA) corroborated findings of D-PLSR. (A) Moderate separation along principal component 2 (PC2) indicated divergent cytokine expression profiles under unsupervised analyses. **(B)** Mean PC2 score was significantly upregulated by stiff UHMWPE fixation. n=9-11 **(C)** Key differentially expressed cytokines along PC2 were similar to LV1, where positive values correspond to increased expression under compliant fixation and negative values represent increased expression under stiff fixation. ***p<0.001 via t- test.

5.3.4 Mechanical loading supported endochondral woven bone formation at 3 weeks

Qualitative histological analysis of defect tissue samples at 2 and 3 weeks revealed that marked changes in tissue composition occurred during this relatively brief interval (Figure 27). At 2 weeks, the defect was predominantly comprised of alginate hydrogel from the BMP-2 delivery vehicle. Irrespective of fixation stiffness, the presence of alginate declined between weeks 2 and 3, while qualitative increases in mineralized tissue were simultaneously apparent. Hypertrophic chondrocytes were evident at 3 weeks throughout defects stabilized by compliant fixators, suggesting the initiation of endochondral ossification. Vessels perfused with contrast agent were visible in 3 week samples. Qualitatively supporting microCT angiography results, more vessels were apparent in stiff PSU stabilized defects. Picro Sirius red staining viewed under polarized light revealed large red collagen fibers adjacent to regions of hypertrophic chondrocytes with UHMWPE,

indicative of woven bone formation. Collagen in PSU-stabilized samples appeared primarily orange-yellow in color and qualitatively smaller in size. Lamellar collagen architecture was not observed in either group at these early time points.

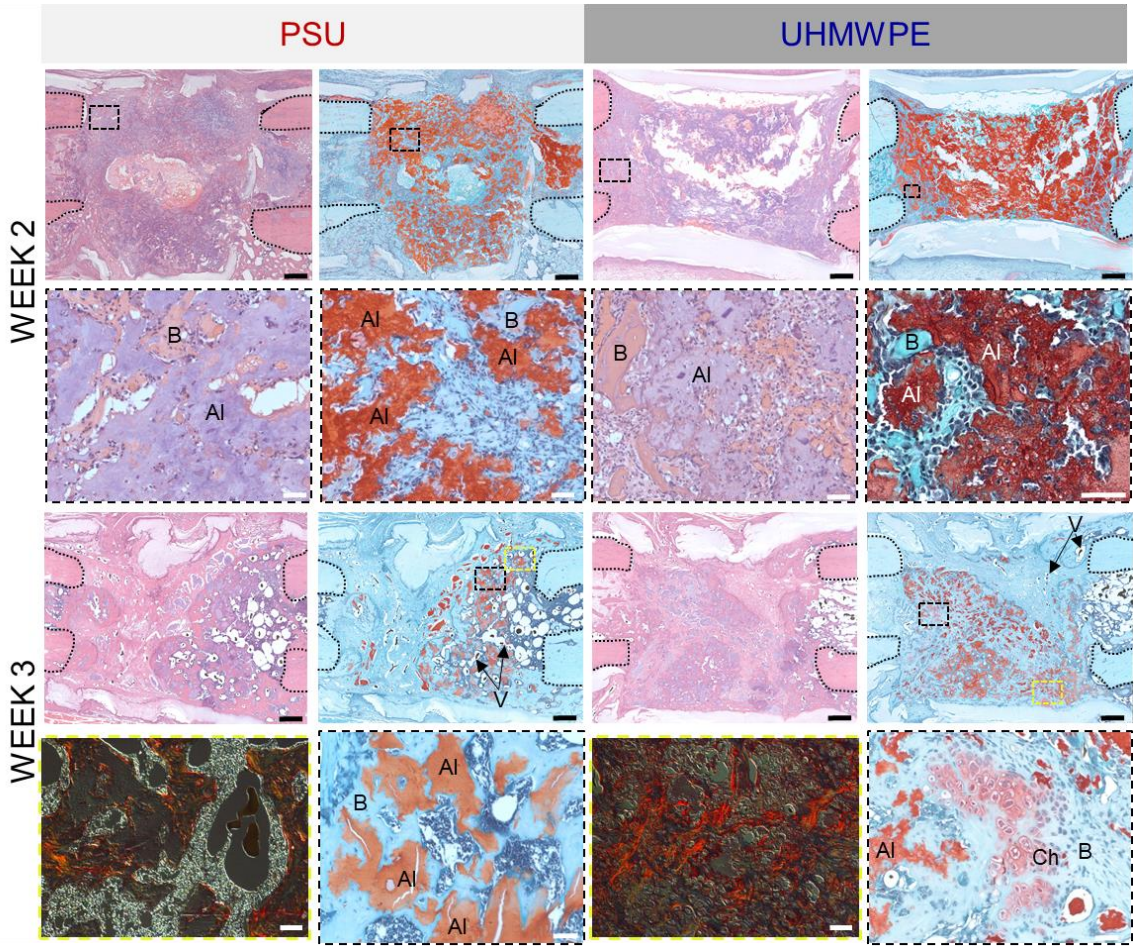

Figure 27: Mechanical loading supported endochondral woven bone formation at 3 weeks. Bone defect at histology at 2 and 3 weeks, including Hematoxylin & Eosin (left column for PSU and UHMWPE, except for bottom image), Safranin-O/Fast Green (right columns), and Picro Sirius red (bottom image in left columns). Alginate hydrogel remnants are denoted as "Al", bone is denoted as "B", chondrocytes are denoted as "Ch", and blood vessels are indicated with arrows extending from "V". Insets are registered to full defects by color-coded dotted rectangles. Black scale bar = 500 µm. White scale bar = 50 µm.

5.3.5 M2-like macrophages were present in defect under compliant fixation at 2 weeks

Qualitative IHC analysis revealed regions of numerous CD11b+/CD163+ M2-like macrophages present within defect tissue stabilized by compliant UHMWPE fixators (Figure 28). These regions were primarily observed near the transition from soft tissue and alginate to immature woven bone. Qualitatively, regions containing numerous M2-like macrophages were not observed under stiff PSU fixation. CD11b+/CD163- M1-like macrophages were not observed in the defect, regardless of fixator stiffness.

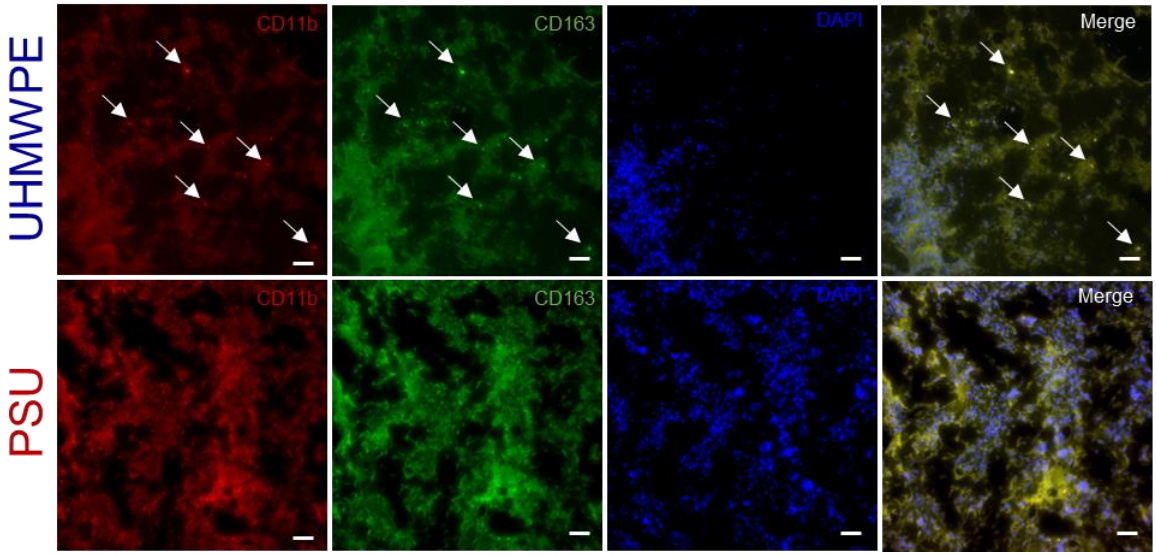

Figure 28: M2-like macrophages were present in defect tissue under compliant fixation at 2 weeks. IHC of bone defect at week 2 suggests M2-like macrophages are present under compliant UHMWPE fixation; red = CD11b+, green = CD163+, blue = DAPI; white arrows denote regions containing CD11b+/CD163+ M2-like macrophages; White scale bar = 50 μm.

5.3.6 Mechanical analyses of bone defect mechanical environment throughout early stage repair

Specimen-specific longitudinal FE analyses revealed elevated 3rd principal strain magnitude (the maximum local compressive strain) during gait within defects stabilized by compliant UHMWPE fixation at 1 week (Figure 29 & Figure 30A & B; UHMWPE: -1.54

± 0.17%; PSU: -0.76 ± 0.06%, p = 0.077). Between 1 and 3 weeks, woven bone extending from the intact bone ends was formed within the defects. The deposition of relatively stiff woven bone reduced the proportion of soft tissue within the defect. Consequently, the magnitude of 3rd principal strain within soft tissue increased between weeks 1 and 3 (Figure 30A & C; Wk 3: UHMWPE: -1.89 ± 0.35%; PSU: -1.38 ± 0.35%, *p = 0.04 Wk 1 vs. 3). As indicated by representative FE model cross-sections, the magnitude of strain was relatively heterogeneous throughout the defect, reaching 3-6% in some regions under compliant fixation and 5-10% under either fixation at 1 and 3 weeks respectively (Figure 29 & Figure 30B & C). In newly formed woven bone, mean 3rd principal strain magnitude was similar regardless of fixator stiffness (Figure 30D & E; UHMWPE: -0.47 ± 0.08%; PSU: -0.55 ± 0.12%, n/s).

The resultant axial load at the proximal femur during gait averaged 3.78 ± 0.35 bodyweight (BW) overall (Figure 30F). Axial load did not change between 1 and 3 weeks and was not affected by fixation stiffness. Actual loads varied widely from animal to animal (Min: 0.87 BW; Max: 7.2 BW), and there was a significant effect of matching animals ($p < 0.05$), suggesting heterogeneity in hindlimb utilization on a per animal basis as each recovered from surgery.

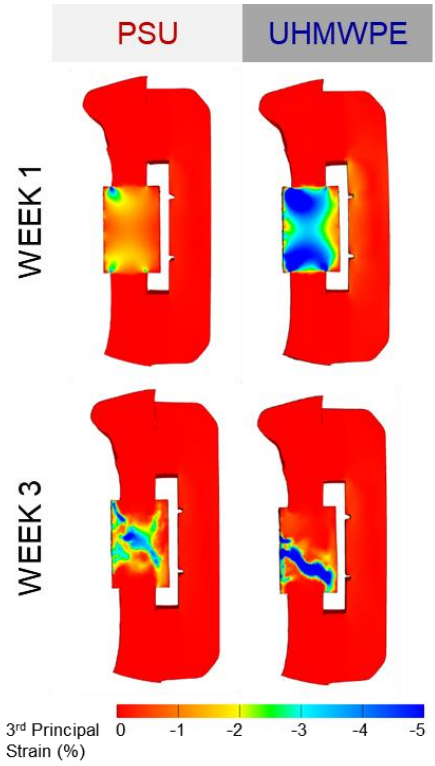

Figure 29: Mechanical analyses of bone defect mechanical environment throughout early stage repair. Representative image-based finite element model cross-sections demonstrate elevated compressive strain magnitude within UHMWPE-stabilized defects.

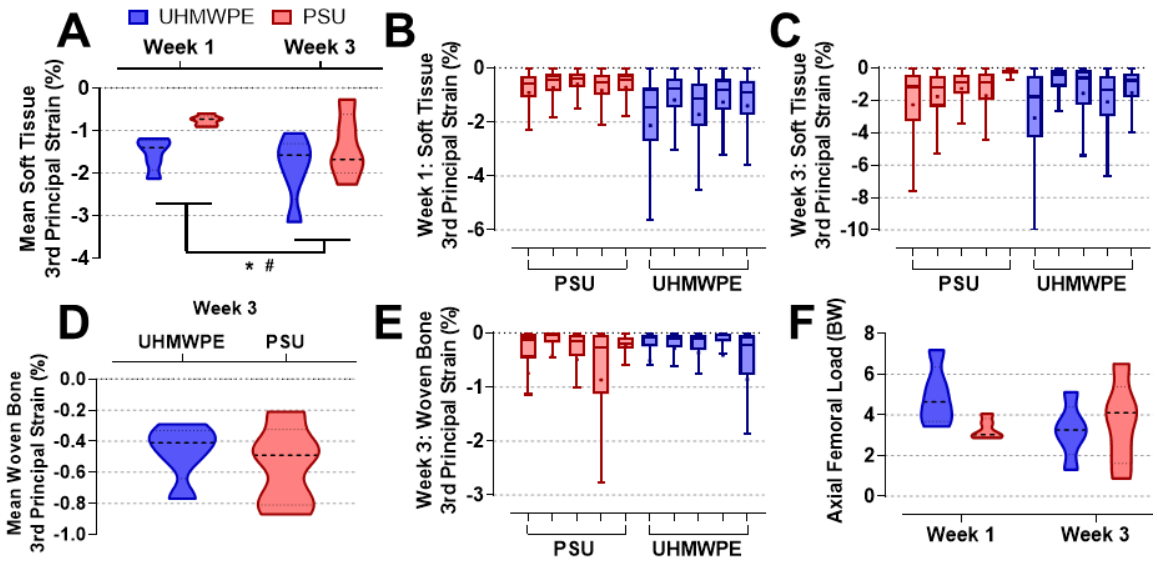

Figure 30: Tissue strain is elevated by compliant fixation and localizes to soft tissue as woven bone forms. (A) Mean 3rd principal strain of non-mineralized soft tissue within

the defect increased between 1 and 3 weeks due to the increased proportion of much stiffer woven bone as healing progressed. n=5. *p<0.05 Wk 1 vs. 3, #p=0.077 UHMWPE vs. PSU via Two-way RM ANOVA. Tissue strain distribution within each sample was spatially heterogeneous throughout the defect soft tissue at **(B)** 1 and **(C)** 3 weeks. In all box plots, the mean is denoted by a dot and whiskers are defined using the Tukey method. **(D)** Mean 3rd principal strain magnitude within immature woven bone at 3 weeks averaged approximately 0.5% regardless of fixator stiffness. n=5. n/s via t-test. **(E)** Woven bone tissue strain was similarly heterogeneous throughout the defect in each sample. **(F)** Peak femoral loads were variable between animals, averaging approximately four-fold body weight (BW) regardless of fixator stiffness or time point. n=5. n/s via Two-way RM ANOVA.

5.4 Discussion

Controlled mechanical loading of bone defects represents a promising therapeutic approach to stimulate endogenous bone repair with the goal of reducing the risk of nonunion. Osteogenesis stimluated by mechanical loading after bone defects have been bridged with mineralized tissue are well described. However, there is very little data characterizing how potentially beneficial biophysical stimuli modulate the early stages of tissue repair after skeletal injury. Increasing evidence has demonstrated the fundamental role of the immune response in coordinating cell recruitment and angiogenesis preceding mineralization, and preliminary in vitro studies support that immune mediators are sensitive to mechanical stimuli. Elucidating the interplay between biophysical stimulation and early stage bone repair is critical to gain a mechanistic understanding of how best to employ mechanical therapies to benefit patients at elevated risk of non-union.

In this study, we observed that mechanical load sharing previously shown to significantly enhance bone repair in the presence of a minimal healing dose of BMP-2 exerted substantial effects on the early stage molecular, cellular, and structural progression of bone defects. Vascular infiltration into the defect at 3 weeks was significantly altered by

dynamic strain magnitude, where reduced strain permitted by stiff PSU fixators led to elevated vascular volume in the defect at 3 weeks. However, the relatively larger magnitude deformation with UHMWPE fixation still supported similar vascular volume to intact femora. Furthermore, load shielding under PSU fixation permitted an increase in the number of relatively small vessels in the defect at 3 weeks, whereas the vascular number under UHMWPE fixation was similar to the naïve contralateral femur. Supporting the variation in vascularization observed at 3 weeks, VEGF levels in the defect tissue lysate were upregulated by stiff fixation at 2 weeks. One of our previous studies in this segmental defect model used similar BMP-2 dosing and a compliant fixator possessing a stiffness about 50% lower than the UHMWPE fixators; the former fixators with lower stiffness dramatically impaired both vascular ingrowth and bone regeneration after injury[34]. Conversely, in CHAPTER 4 we observed a potent osteogenic effect from the deformation permitted by UHMWPE fixation possessing a more moderate compliance. Given the single 3 week measurement of vascularization in this study, it cannot be explicitly determined if increased strain magnitude permitted by compliant UHMWPE fixation reduced or delayed angiogenic sprouting, or accelerated pruning. Regardless, vascular volume, number, and size distribution with compliant fixation was similar to intact bone, suggesting that a threshold of sufficient vascularization had been achieved.

Together with our previous work, these data indicate a potential minimum threshold of vascularization is necessary to support osteogenesis, above which there may not be further benefit to the regenerative capacity of the tissue. These results contrast the generally accepted paradigm directly linking the enhancement of angiogenesis with improved osteogenesis. Instead, there appear to be distinct magnitude-dependent mechanobiological

thresholds that differentially impair either bone or neovascular growth when exceeded. As a result, increased strain magnitude can slightly modulate the progression of angiogenesis but still support sufficient tissue revascularization to significantly enhance bone repair.

Peak compressive strain magnitude in unmineralized defect tissue under UHMWPE fixation averaged -1.54 ± 0.17% at 1 week and -1.89 ± 0.35% at 3 weeks. Strains were reduced under stiffer PSU fixation, averaging -0.76 ± 0.06% and -1.38 ± 0.35% at 1 and 3 weeks, respectively. As deposition of comparatively stiff woven bone initiated, the strain magnitude within non-mineralized defect tissue increased between 1 and 3 weeks and deformation localized to remaining soft tissue regions. Spatial heterogeneity in deformation was apparent at both 1 and 3 weeks, though soft tissue regions with locally elevated strain magnitudes remained below 10-15% strain, a biomechanical threshold implicated to promote fibrosis and hypertrophic non-union throughout[50,175,176]. FE simulations also revealed that animals exerted an axial load at the proximal femur of approximately 4-fold bodyweight during rehabilitative treadmill walking sessions which was unaffected by fixation stiffness or time. Considering the bone injury and iatrogenic effects of the surgery, these results are comparable with an inverse dynamics analysis by Wehner and colleagues which estimated that the peak axial load through the proximal femur in an uninjured rat was 6-fold bodyweight[183].

Consistent with prior reports, larger magnitude strain permitted by UHMWPE fixation supported endochondral ossification at 3 weeks, whereas intramembranous ossification was predominant with PSU[50,62,126,234,235]. We previously observed the presence of hypertrophic chondrocytes in this mechanical loading model at 8 weeks, at which point there was a significant 60% increase in bone formation over stiff fixation. Together, these

findings support that skeletal repair in the presence of BMP-2 can proceed via either intramembranous or endochondral ossification, and that the biomechanical conditions can dictate this switch. Overall, the data indicate there is a strain magnitude threshold where vascularization begins to be reduced or delayed slightly while bone repair is simultaneously improved, primarily via endochondral repair. Prior work using significantly more compliant fixation systems have demonstrated that further increases in local tissue strain exceeding 10-15% dramatically inhibits both angiogenesis and osteogenesis[34,50]. Therefore, the biomechanical environment produced by rehabilitative or mechanical therapies must be carefully monitored to be safe and efficacious.

In addition to VEGF, expression profiles of immune cytokines and chemokines were also differentially regulated by strain magnitude. Multivariate expression profile analysis indicated levels of LIX (CXCL5), IL-1β, and RANTES (CCL5), cytokines classically categorized as pro-inflammatory and angiogenic, were elevated by mechanical loading. Even after the resolution of acute inflammation, IL-1β signaling has also been shown to play subtle roles stimulating various phases of tissue regeneration, including VEGF production, endochondral ossification, and bone remodeling[174,236–239]. In addition, LIX (CXCL5) expression has been shown to enhance angiogenesis, inhibit osteoclastogenesis, and is secreted by mesenchymal progenitors via non-canonical WNT signaling as well as by macrophages[240–243]. Similarly, RANTES (CCL5) promotes VEGF productions and angiogenesis[243–245]. These data are consistent with in vitro experiments in monocytes and sheep osteotomy studies indicating mechanical loads elevate immune cell expression of paracrine signals canonically associated with acute inflammation[16,225]. Further supporting elevated immune activity in response to loading, we observed clusters

of CD163+ M2-like macrophages near the transition between woven bone and soft tissue in defects stabilized by compliant UHMWPE fixation at 2 weeks. More specifically, the CD163 surface receptor is associated with M2c macrophages, a phenotype associated with IL-1β expression and the promotion of ECM remodeling and angiogenesis via secretion of MMP9[213,246,247]. Qualitatively, myeloid lineage cells were not observed to the same extent under stiff fixation. Taking the protein, cellular, and vascular analyses conducted in this study together, the data suggest that the early stage immune response is mechanosenstive and that the therapeutic effects of mechanical loading may initially be manifested by altering early stage immunological aspects of bone repair prior to cartilaginous callus or osteoid formation. We speculate that slight elevations in chemokine and cytokine signaling due to loading may facilitate sustained progenitor recruitment into the defect, but further research is warranted to determine the downstream effects of mechanosensitive perturbations in immune paracrine signaling on specific progenitor cell sub-populations that mediate osteogenesis.

When considering the immunological findings of this segmental defect study alongside transverse fracture models common in the literature, it is worth noting that each model produces differing degrees of trauma. The model used in this study better represents segmental defects created surgically after the resection of tumors, debridement of heavily comminuted traumatic fractures, or spinal fusions and corpectomies. The data are particularly applicable to such defects treated with BMP-2. Alterations in the immune response due to the injury mechanism would be expected to be play a more significant role at very acute stages, but appreciable differences could still be present at 2 and 3 weeks.

The acute inflammatory response is critical to coordinate skeletal repair after injury. The data presented here suggest that key immune cytokines coordinating bone repair are mechanosenstive and are stimulated by osteogenic mechanical loading produced by rehabilitative activity. Additionally, these data demonstrate that increased levels of vascularization at intermediate time points do not necessarily portend enhanced bone regeneration. The findings of this study motivate continued research to examine the proximate effects of mechanically sensitive immune signaling on endochondral bone repair.

CHAPTER 6. CONCLUSIONS AND FUTURE DIRECTIONS

6.1 Primary Conclusions & Contributions to the Field

Together, the work conducted in this thesis supported 4 principal contributions:

1) Established a new sensor platform that can non-invasively quantify strain across skeletal defects in vivo
2) Validated that the aforementioned platform can be used to measure dynamic strains imparted by rehabilitation and assess both the temporal progression of the healing process, including bridging
3) Challenged the paradigm that targeting enhanced angiogenesis will necessitate improved bone repair
4) Demonstrated mechanosensitivity of the immune response after injury

. While prior studies have demonstrated the substantial osteogenic potential of mechanical stimulation to enhance fracture healing, the tissue-level mechanical environment within the regenerative niche was either not quantified or stimulated via invasive loading systems that exert non-physiological loading patterns not representative of locomotion[126]. Therefore, a major challenge facing researchers seeking to develop novel regenerative strategies that integrate therapeutics and rehabilitation is defining and controlling the mechanical environment in vivo. Due to this lack of understanding, fractures requiring open surgical reduction and internal fixation are typically handled very conservatively and are primarily non-weight bearing for 6-12 weeks after stabilization[204]. Motivated to address this challenge, the studies described in this thesis were envisioned to

engineer technical platforms that enable longitudinal quantification of in vivo mechanical cues, and to elucidate how perturbing the magnitude of these mechanical cues modulates the progression of bone repair. The findings and conclusions represent both technical and scientific advances, where a novel technological platform was developed and exploited to investigate previously unexplored mechanobiological phenomena.

Biomedical Sensors

In Aim I, we developed a first-of-its-kind wireless implantable strain sensor platform with which to measure dynamic mechanical strain across a bone defect during functional movements[196]. Through rigorous in vitro testing, we demonstrated the sensor platform possessed promising sensitivity and signal resolution to monitor physiological strain magnitudes and to detect the progression of bone repair. Preliminary in vivo implantation studies further validated the potential of the sensor to non-invasively quantify mechanical strain across bone defects in real-time during gait.

In Aim II, we integrated the strain sensor platform into stiff and compliant internal fixators, allowing us to both perturb and quantify the in vivo mechanical environment. We deployed the sensor platform to longitudinally measure strain over 8 weeks after creation of a segmental bone defect. Notably, strain magnitude measurements exhibited significant positive correlations with the bone volume present in the defect. These results are consistent with previous reports suggesting the potential utility of strain sensing modalities as an X-ray free diagnostic to assess fracture or spinal fusion healing[149,249]. Such radiographic-free approaches are particularly beneficial for pediatric populations whose exposure to X-rays warrants significant restraint[205,250]. The diagnostic potential of both

wearable and implantable sensors has been established for decades in cardiology and cardiac electrophysiology[251,252]. Future work incorporating sensors into implants used in the treatment of complex orthopaedic or spine procedures is warranted and has the potential to provide important post-surgical feedback to clinicians. Furthermore, the incorporation of sensors into actuating implants, such as recently introduced growing spinal rods used to treat scoliosis, has significant potential to confer feedback control for clinicians to optimize healing based on real-time diagnostic information[253].

Together, Aims I and II demonstrated that microfabrication and low power telemetric systems have reached sufficiently small size and low cost to be effectively leveraged in pre-clinical models, including small animals. The novel findings enabled by the strain sensor platform motivate the expansion of development efforts for sensor and telemetry systems with the ability to study pre-clinical models of tissue degeneration or repair. Expanded usage of sensors explicitly developed for biomedical applications offers significant potential to quantify dynamic biophysical or biochemical signals present in the regenerative niche and to inform the rational design of new therapeutics and biologics[170].

Mechanical Loading

In Aim II, periodic walking on a treadmill was employed to mimic dynamic functional loading conferred by rehabilitation. In vivo strain amplitudes acquired while animals walked were used as boundary conditions for finite element models of the regenerating femur to determine the tissue-level mechanical environment created by rehabilitation. The findings of Aim II corroborate prior reports in the literature that dynamic compressive strain magnitudes in the range of 1-7% are potently osteogenic

compared to load-shielding and promote a mechanistic shift from intramembranous toward endochondral ossification[50,176]. Furthermore, the magnitude of strain at 1 week held significant positive correlations with long term healing outcomes, suggesting early stage mechanical stimuli have significant potential to augment bone repair.

The segmental defect model was employed to create a repeatable mechanical environment throughout this thesis. This is an important limitation to note because this model represents a simplified mid-diaphyseal injury that does not recapitulate the architectural complexities of severe traumatic injuries or congenital deformities sometimes encountered clinically. Nonetheless, the studies conducted in this thesis demonstrate that simple functional movements have the potential to create therapeutic biophysical stimuli in a cost-effective manner. To address more complex scenarios, validated clinical orthopaedic classification systems could be used to segment prevalent injury patterns, and similar biomechanical environment evaluations during rehabilitative activities could be performed on representative injury sub-classes of interest[254].

Mechanobiology of Early Stage Bone Repair

Given the observations of improved bone repair due to early loading and the significant correlation of strains at 1 week with long term repair in Aim II, we hypothesized that early stage mechanical loading differentially regulates early stage biological processes such as immune cytokine signaling and angiogenesis that coordinate bone repair before mineralization. Preliminary in vitro work reports suggest that cells mediating these processes are mechanosensitive, but the early stage biological effects of mechanical stimulation in well-defined biomechanical environments have not been studied[60,224,225]. In

Aim III, we investigated effects of osteogenic mechanical loading on early stage repair and observed significant changes in defect revascularization and cytokine signaling.

Angiography analysis revealed that vascular volume was actually increased at 3 weeks within load-shielded bone defects relative to defects stimulated with osteogenic mechanical loading. Mechanically loaded defects maintained similar vascular volume to naïve contralateral femurs, suggesting that there may be threshold of sufficient vascularization above which there are negligible benefits to bone repair. Consistent with the 3 week angiography data, we observed elevated VEGF levels in load-shielded defects at 2 weeks. Conversely, mechanically loaded defects were associated with increased LIX (CXCL5), IL-1β, and RANTES (CCL5) levels, cytokines implicated in inflammation, cell recruitment and survival, and matrix synthesis. We speculate moderate elevations in these cytokine signals may exert beneficial effects by promoting sustained cell recruitment[15,16,20,255], but this hypothesis requires further research to be tested. While elucidating the specific mechanism by which immune signals enhance load-induced bone repair will require additional investigation, this thesis is among the first in vivo studies demonstrating that the immune response is sensitive to relatively small magnitude changes in the mechanical environment.

Overall, these data break with the widely held paradigm that therapeutically targeting increased vascularization will assure improved healing outcomes, as increased vascularization at 3 weeks in this study did not lead to improved bone repair. Placing the findings of this thesis alongside the literature suggests the following simplified working model describing how osteogenesis and angiogenesis are regulated by the initial magnitude of dynamic compression after skeletal injury (Figure 31). Here, slight elevations in strain

magnitude in the range 2-7% enhance osteogenesis and gradually shift the healing mechanism from primarily intramembranous ossification toward endochondral repair[50,126,176]. Concurrently, angiogenesis at intermediate time points in healing is slightly modulated as strain increases without negatively impacting osteogenesis and bone repair. As strains approach 10%, angiogenesis is substantially impaired and osteogenic potential begins to diminish[34,176]. Deformation up to 15% may yield successful bone repair via considerably prolonged endochondral ossification, but there is evidence of significant risk for fibrosis and non-union beyond 10% strain[34,50,126]. Thus, therapeutic strategies incorporating mechanical stimulation must be developed and implemented carefully, ensuring the resultant mechanical environment produced by a loading device or rehabilitation activity is in the maximal osteogenic range. Incorporating real-time sensing capabilities demonstrated in this thesis into orthopaedic devices may ease the development of safe and effective loading therapies that exploit early stage skeletal mechanobiology to improve patient outcomes.

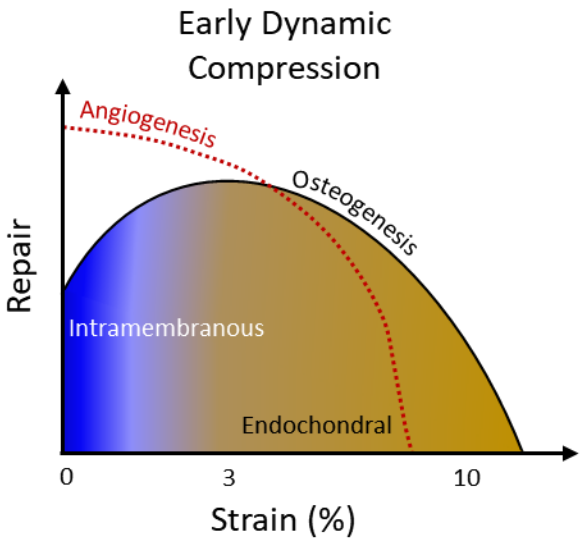

Figure 31: Simplified working model describing effects of early dynamic compressive strain magnitude on osteogenesis and angiogenesis.

6.2 Future Directions

The findings of this thesis motivate the future exploration of several interesting questions and research initiatives. The potential research initiatives outlined below focus on three thrusts: (1) using this relatively well characterized in vivo model to obtain a more mechanistic understanding of early stage mechanobiology, (2) establishing biological and biomechanical congruence between pre-clinical models and clinical protocols of rehabilitation, (3) improving the technical versatility of biomedical sensors for a wider range of clinical and scientific applications.

Mechanobiology

While Figure 31 outlined a simplified working model describing the effects of early loading on angiogenesis and osteogenesis, a number of experiments could greatly improve the fidelity of this model. First, a more detailed temporal characterization of defect

revascularization kinetics would help to answer the question if early mechanical loading slightly reduces, delays, or actually accelerates remodeling of newly formed vessels. This could be achieved by completing microCT angiography at multiple time points. Furthermore, while microCT angiography facilitates quantification of perfused arteriole-level blood vessels, it does not have sufficient resolution to capture capillaries or immature angiogenic sprouts. Efforts to quantify microvasculature within tissue samples using serial sectioning and digital reconstruction could aid our understanding of how the seminal stages of angiogenesis are regulated by biophysical stimuli. Quantification and imaging of microvasculature structures within and surrounding actual bone defects could also inform image-based finite element simulations to investigate underlying mechanobiological mechanisms regulating vessel growth in vivo. The Weiss group have developed an open-source angiogenesis simulation plug-in for FEBio called AngioFE and has substantial expertise creating such models based on in vitro systems[256]. Simulations of the mechanical environment could be complimented by detailed biological characterization of gene and protein expression of in vivo samples, analogous to in vitro PCR microarray analyses conducted by Ruehle on dynamically loaded 3D microvessel cultures in their recently submitted doctoral thesis.

This thesis targeted two mechanical environments by modulating internal fixator stiffness: a stiff load-shielding plate permitting very low strains, and a moderately compliant plate allowing osteogenic strains. The development of an excessively compliant fixator platform with an integrated strain sensor would help to define the threshold where mechanical loading results in fibrosis and hypertrophic non-union. In light of the findings of this thesis, a more nuanced question that could be answered using a more compliant

fixator is what is the threshold of minimum revascularization to achieve bone repair? Given we observed a reduction in vascularization at 3 weeks due to loading while bone repair was enhanced, it would be beneficial to determine when further deformation disrupts vascularization so severely that non-union occurs. The best estimate of this threshold is likely 10% based on previous work from our lab, though this is a rough estimate because the sensor platform had not been developed and thus actual mechanical environment was not quantified[34].

Differences in the expression of immune modulatory cytokines at 2 weeks due to loading indicate that previously unexplored critical inflammatory processes during tissue repair are mechanosensitive. Critical questions warranting further research include: What cell types are differentially secreting VEGF, IL-1β, and CXCL5 in response to deformation? What cells are these cytokine and chemokine signals acting on? Preliminary evidence in the literature indicate that macrophages may play a pivotal role in this process, but we speculate that multiple cell types including neutrophils, mesenchymal and endothelial progenitors, and T cells may also be involved. We performed a pilot flow cytometry analysis of macrophages within the defect tissue at 10 days, but total cell numbers were too low to robustly classify cell sub-populations. Using a smaller defect 2-3 mm defect could perhaps enable more rapid cell recruitment and permit quantitative cytometric analysis of the defect tissue. However, decreasing the defect size would also alter the tissue-level mechanical environment. Alternatively, temporal characterization of cell subtypes with relatively low numbers present could be achieved using IHC. Nonetheless, the overarching objective of all the aforementioned methods is to define the underlying biological targets altered by early mechanical loading long before osteogenesis

actually occurs, and to investigate how these targets propagate downstream signaling as mineralization ensues.

Rehabilitation

A potential path forward to clinically translate the mechanobiological findings of this thesis will rely on studying rehabilitation protocols that safely deliver mechanical stimulation. We selected treadmill walking for 10 minutes at a slow controlled speed because: (1) it produced repeatable cyclic strain cycles, (2) the step frequency was sufficiently slow (1-1.5 Hz) that is would not be aliased by the digital transceiver (30 Hz sampling frequency), and (3) because it approximated our best estimate of a total distance covered in a full day of in-cage activity. To better optimize rehabilitation, there is a strong need to develop more representative pre-clinical small and large animal models that better simulate actual physical therapy or clinical rehabilitation activities. The recent work of Dalise and colleagues represents a systematic approach to recapitulate dose-dependent effects of aerobic exercise commonly prescribed in physical therapy in small animal models[208]. Similar approaches could be undertaken using the pre-clinical segmental defect model developed in this thesis by investigating activity type, frequency, and duration as experimental variables and studying the resultant mechanical environment along with the bone healing outcomes.

Biomedical Sensors

The key technical challenges facing widespread adoption of biomedical sensors for both research and clinical applications lie in a few areas. First, the footprint of fully integrated devices remains a barrier to entry for relatively small microenvironments of

interest, such as, cartilage lesions, arterioles, or the eye. While most electrical components can readily be miniaturized to extremely small sizes given sufficient design resources, the key component limiting miniaturization of the overall size envelope remains the battery. Therefore, continued research is needed to further maximize power density of battery systems, minimize power consumption of implantable circuitry, or to improve the range and reliability of passive powering systems that eliminate the need for large power sources. Recent demonstrations of passive power transfer to deep-tissue devices implanted up to 4-5 cm beneath the skin are extremely encouraging[257,258]. Future research to passively power implantable devices will significantly expand the breadth of feasible use cases.

Finally, besides bone, the vast majority of biological tissues are far too compliant to interface with the traditional suite of MEMS materials used in this study. Recently, technical feasibility has been demonstrated in a number compliant biomedical sensor systems for wearable and implantable soft tissue applications[152,259,260]. Continued fundamental research in materials and fabrication techniques to construct highly flexible and stretchable sensors, circuit components, and power sources, as well as durable and biocompatible adhesives could spread applicability of biomedical sensors throughout the body. The ability to continuously and quantitatively assess physiological properties of interest in situ represents a disruptive change to the current clinical treatment paradigm for the vast majority of diseases, and future research toward engineered systems that can accomplish this task is warranted[170,261].

APPENDIX A. STRAIN SENSOR FIXATOR PREP PROTOCOL

Materials

1. PSU or UHMWPE fixator (see Appendix B)
2. Strain sensor (Micro-measurements # MMF001747 EA-06-125BZ-350/E)
3. 220 grit sandpaper
4. VWR lab tape
5. Razor blade
6. Isopropyl alcohol
7. Surgical instrument cleaner
8. Conditioner & neutralizer solutions (from Omega #TT300 adhesive kit)
9. Cotton swabs
10. M-Bond AE-10 epoxy (Micro-measurements)
11. Rubber blocks (cut from McMaster-Carr neoprene strip, 1/8" Thick)
12. Pinstripe brush
13. Dymax 3401 UV-curing adhesive
14. Dymax 1072-M UV-curing adhesive
15. Dymax UV spotlamp
16. SS-braided wire (AM systems #793200 Nominal AWG: 41 bare, 36 coated)
17. Silicon rubber tubing (AM systems #806100 Inside diamter 0.012 in.)
18. Wire crimpers
19. Soldering iron
20. Solder (Kester 32117 24-6040-0027 60/40 Stand, 0.031" Diameter,"44", 1.5)
21. Easy-clean “blue” flux (McMaster-Carr 7755A1)
22. Stainless steel “black bottle” soldering flux (McMaster-Carr 7695A1)
23. Teflon covers (laser-cut from McMaster-Carr #8711K91, 0.015” thick)
24. Music wire (McMaster-Carr 302/304 SS Wire, 0.010" Diameter, 1' Long)
25. Omnetics copper connectors (D4354-701 female nano contact)

Set-up

26. Set oven temperature to ~60°C for PSU or ~37°C for UHMWPE
27. Tape white plastic adhesion fixture to clear area on bench

Plate surface preparation

1. Dry abrade pocket of fixation plate where strain gage will be adhered with 220 grit sandpaper
2. Sonicate fixation plates for 15 minutes in DI water with a few drops of surgical instrument cleaner

3. Throughout steps 2 and 4, trim strain gage matrix to size using razor blade while sensors sit on a glass slide. Trim each side of the sensor up to the triangular alignment marks
4. Sonicate fixation plates for 15 minutes in Isopropyl alcohol (IPA)
5. Dry plates and place them in adhesion fixture
6. Using cotton swabs, wipe sensor pocket of each plate with Conditioner solution
7. Wet abrade the sensor pocket of each plate
8. Using cotton swabs, wipe sensor pock again with Conditioner (water with trace phosphoric acid to etch the plate), then immediately dry with another swab
9. Using cotton swabs, wipe sensor pock again with Neutralizer (water with trace ammonia to rebalance pH), then immediately dry with another swab
10. Using blue low-tack tape, position each sensor on a fixation plate so that it can be mounted into sensor pocket, orient sensor so that solder pads are offset to one end of plate with wire routing slot on side of plate to the left. The bottom edge of the solder pads should be about even with the top edge of the wire slot.

Sensor adhesion

1. Mix M-Bond AE10
    a. Use dropper to withdraw curing solution to marking on side of dropper
    b. Dispense curing solution into epoxy container
    c. Mix vigorously with stir rod for 3-4 minutes
2. Using fine tip paint brush, apply very thin layer of epoxy to underside of gage and into sensor pocket on fixation plate
3. Lightly press each gage into the sensor pocket
4. Position rubber block on top of gage so that it will compress into the pocket when pressure is applied
5. Carefully set the 2 steel plates on top of the rubber blocks, ensuring that no sideways motion moves the blocks from their position on the fixation plates
6. Cut tape holding adhesion fixture to table, apply new tape to secure steel plates to the adhesion fixture
28. Carefully move the entire adhesion fixture with steel blocks into oven,
29. For PSU: cure at 60°C for 1 hour / For UHMWPE: cure at 37°C for 3 hours
30. After 1 hour, remove steel blocks from adhesion fixture and increase oven temperature to:
    a. For PSU: 70°C (USE AUTOCLAVE GLOVES)
    b. For UHMWPE: 45°C
31. After 2 hours remove from oven (USE AUTOCLAVE GLOVES)
32. Set on bench and let everything cool.

Wire prep

1. Cut 2 wires to ss-braided wires to equal length (~6 inches)
2. Cut silicone tubing to a slightly shorter length (about 0.5 inch shorter)
3. Wearing gloves, apply UV-curing glue (e.g. Dymax 1072-M) to fingers and run fingers along wires to glue them together. Leave about 3 mm unglued on the end that will be soldered to the strain sensor
4. Slide copper connector tubes over one end of each wire
5. Strip about 1 mm of each wire with razor blade
6. Slide copper connector tube up wire over top of the stripped region and crimp with wire stripper
7. Cut excess copper tubing, leaving 2-3 mm of crimped tube remaining
8. On opposite end of wire, strip wires, flux (with black flux bottle), and tin the two ends together
9. Flux and tin the end of a piece of music wire and solder the braided wire ends to the music wire
10. Push music wire through silicone tubing and pull lead wires through the tubing
11. Once the music wire is through the tubing, de-solder the music wire from the rest of the lead wire
12. Place copper tubes on the uncovered ends identical to the previous side
13. On the end of the wire that is attached to the sensor, tubing should be within 3 mm of the end of the wire so it can be routed and anchored into the wire slot of the plate

Sensor wiring and encapsulation

1. Flux and tin solder pads of sensor, then solder wire ends to sensor
2. Apply a few droplets of Dymax 3401 onto solder connections and cure with light to provide strain relief
3. The tricky part here is to bend the wires 90 to left, wrap them down they side of the plate.
4. Apply a few droplets of Dymax 1072-M into the wire slot on the slide of the plate and place tubing into the slot. The tubing is a force fit into the slot so it should hold in place once you push it into the slot, then use light to cure the glue.
5. On the side of the plate where the sensor is adhered, completely fill the well the sensor sits in with light-curing Dymax 1072-M. The goal is to completely fill the well without any bubbles flush with the top of the walls that form the well so that there is a flat surface to adhere the teflon covers.
6. Once the Dymax 1072-M is cured, roughen the brown side of a teflon cover for the side and back of the plate with 220 grit sandpaper. Wipe off the teflon with a little IPA
7. Apply a few droplets of Dymax 1072-M distributed on the back of the fixation plate and few droplet distributed onto the teflon covers

8. Leave the teflon cover sitting on the table, flip the plate over so that the sensor side is facing the table and place down onto the teflon cover, carefully watching alignment. Hold down with firm pressure and turn on light (since the plate is translucent the light can cure the glue from the opposite side of the plate). Once teflon cover is adhered, carefully scrape away any excess cured glue with forceps or a razor blade.
9. Follow the same procedure for adhering the teflon cover for the side of the plate to cover the wire exit slot.

APPENDIX B. STRAIN SENSOR FIXATOR DRAWING

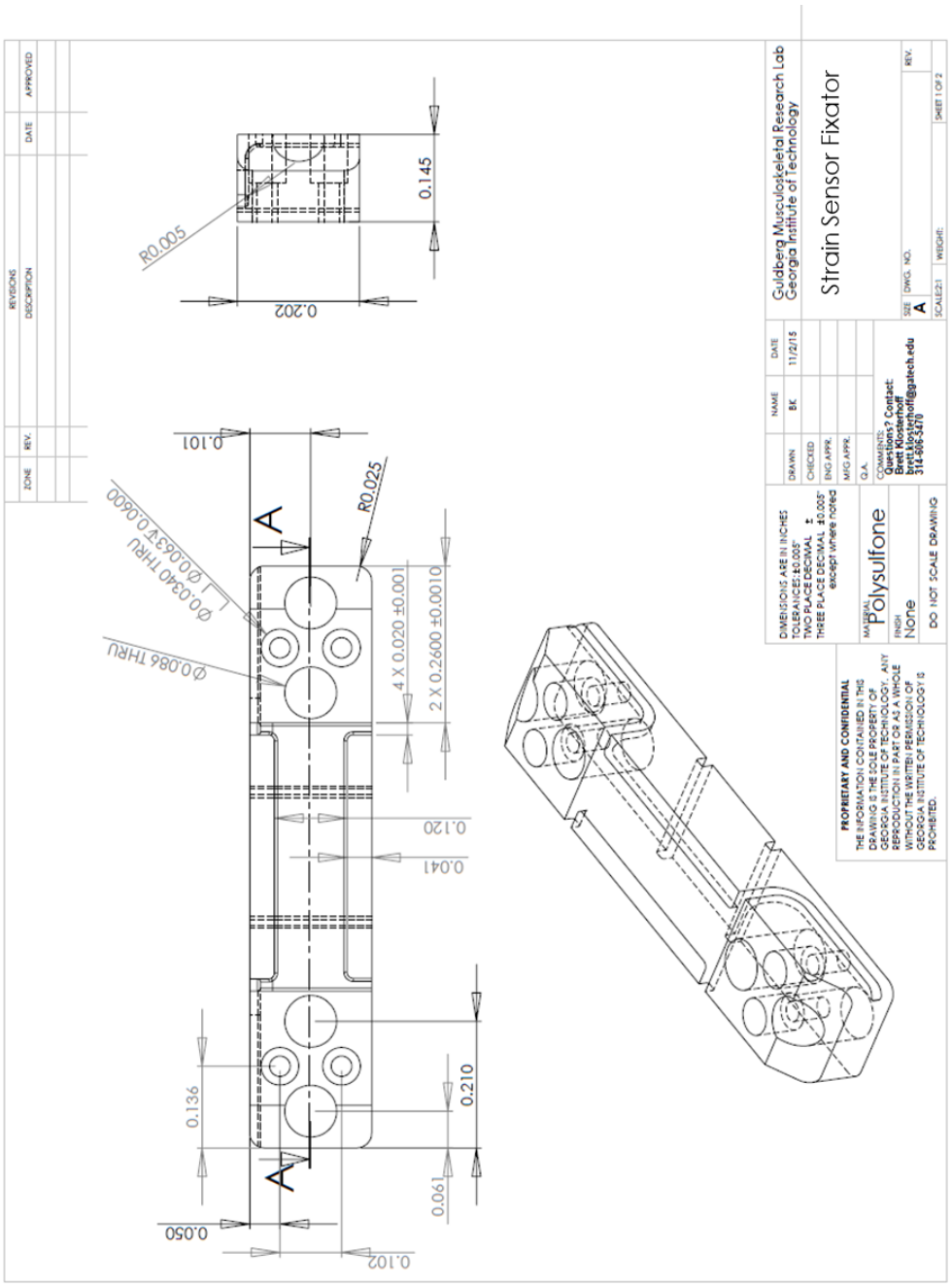

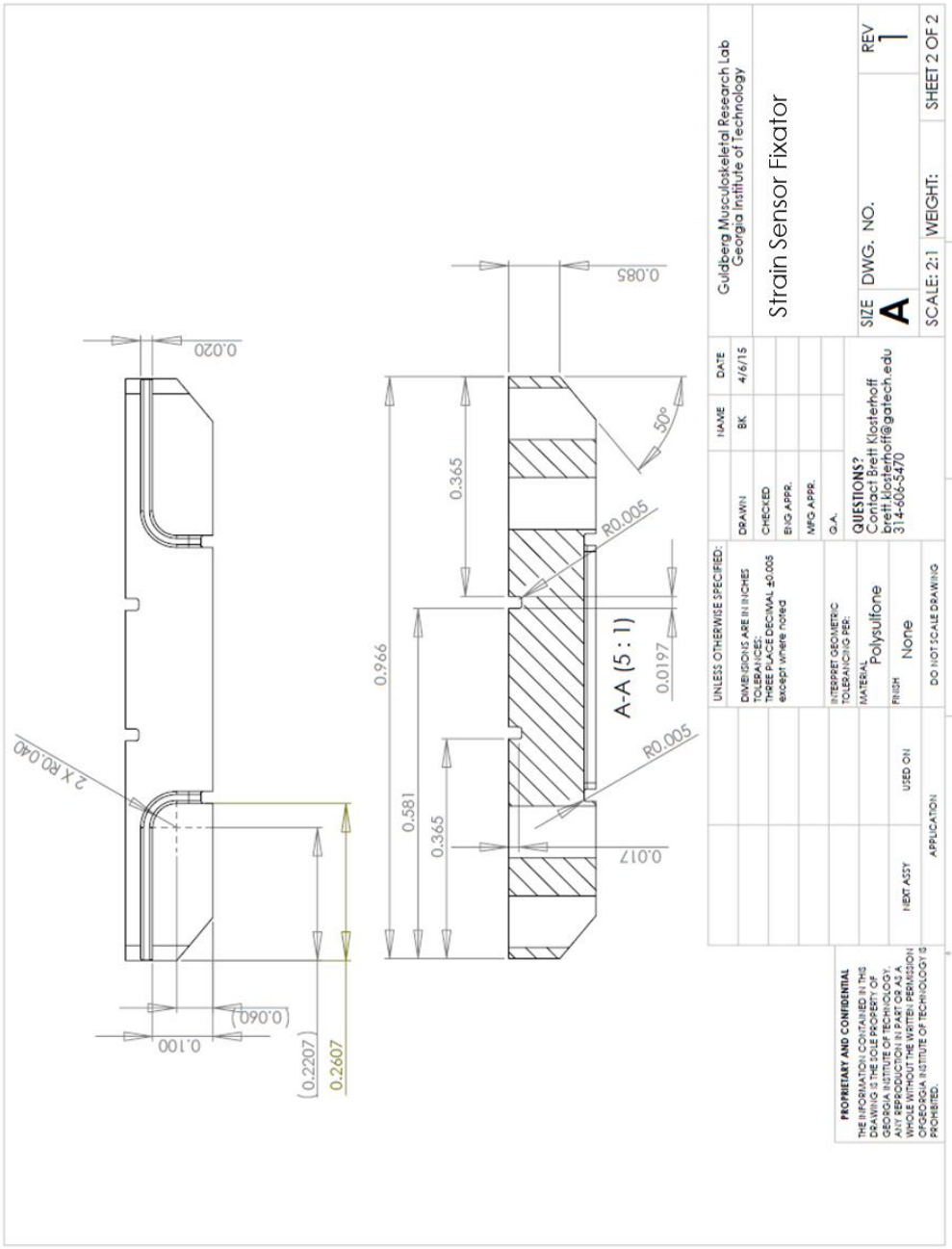
0.020
2 X R0.040
0.100
(0.060)
(0.2207)
0.2607
0.085
0.966
0.365
50°
R0.005
0.581
0.365
A-A (5 : 1)
0.0197
R0.005
0.017
Guldberg Musculoskeletal Research Lab
Georgia Institute of Technology
Strain Sensor Fixator
NAME
DATE
DRAWN
BK
4/6/15
CHECKED
ENG APPR.
MFG APPR.
Q.A.
UNLESS OTHERWISE SPECIFIED:
DIMENSIONS ARE IN INCHES
TOLERANCES:
THREE PLACE DECIMAL ±0.005
except where noted
INTERPRET GEOMETRIC
TOLERANCING PER:
MATERIAL
Polysulfone
FINISH
None
NEXT ASSY
USED ON
APPLICATION
DO NOT SCALE DRAWING
QUESTIONS?
Contact Brett Klosterhoff
brett.klosterhoff@gatech.edu
314-606-5470
SIZE
A
DWG. NO.
REV
1
SCALE: 2:1
WEIGHT:
SHEET 2 OF 2
PROPRIETARY AND CONFIDENTIAL
THE INFORMATION CONTAINED IN THIS DRAWING IS THE SOLE PROPERTY OF GEORGIA INSTITUTE OF TECHNOLOGY. ANY REPRODUCTION IN PART OR AS A WHOLE WITHOUT THE WRITTEN PERMISSION OF GEORGIA INSTITUTE OF TECHNOLOGY IS PROHIBITED.

REFERENCES

1. HCUPnet. Healthcare Cost and Utilization Project (HCUP). *Rockville, MD Agency Healthc Res Qual*. (1997-2012). https://www.hcup-us.ahrq.gov/reports/factsandfigures/figures/2005/2005_3_6C.jsp.

2. Pollak A, Watkins-Castillo S. *Fracture Trends - The Burden of Musculoskeletal Diseases in the United States*.; 2014. http://www.boneandjointburden.org/2014-report/via23/fracture-trends.

3. Zura R, Xiong Z, Einhorn T, et al. Epidemiology of Fracture Nonunion in 18 Human Bones. *JAMA Surg*. 2016;151(11):e162775. doi:10.1001/jamasurg.2016.2775

4. Santolini E, West R. Risk factors for long bone fracture non-union: a stratification approach based on the level of the existing scientific evidence. *Injury*. 2015;46:S8-S19. doi:10.1016/S0020-1383(15)30049-8

5. Tzioupis C, Giannoudis P V. Prevalence of long-bone non-unions. *Injury*. 2007;38:S3-S9. doi:10.1016/S0020-1383(07)80003-9

6. Hak DJ, Fitzpatrick D, Bishop JA, et al. Delayed union and nonunions: Epidemiology, clinical issues, and financial aspects. *Injury*. 2014;45:S3-S7. doi:10.1016/j.injury.2014.04.002

7. Antonova E, Le TK, Burge R, Mershon J. Tibia shaft fractures: costly burden of nonunions. *BMC Musculoskelet Disord*. 2013;14(1):42. doi:10.1186/1471-2474-14-42

8. Beaver R, Brinker MR, Barrack RL. An analysis of the actual cost of tibial nonunions. *J La State Med Soc*. 1997;149(6):200-206. http://www.ncbi.nlm.nih.gov/pubmed/9188244. Accessed May 23, 2017.

9. Busse JW, Bhandari M, Sprague S, Johnson-Masotti AP, Gafni A. An economic analysis of management strategies for closed and open grade I tibial shaft fractures. *Acta Orthop*. 2005;76(5):705-712. doi:10.1080/17453670510041808

10. Patil S, Montgomery R. Management of complex tibial and femoral nonunion using the Ilizarov technique, and its cost implications. *Bone Joint J*. 2006;88-B(7). http://www.bjj.boneandjoint.org.uk/content/88-B/7/928. Accessed May 23, 2017.

11. Ilizarov GA. The tension-stress effect on the genesis and growth of tissues. Part I. The influence of stability of fixation and soft-tissue preservation. *Clin Orthop Relat Res*. 1989;(238):249-281. http://www.ncbi.nlm.nih.gov/pubmed/2910611. Accessed January 12, 2016.

12. Stafford PR, Norris BL. Reamer-irrigator-aspirator bone graft and bi Masquelet

technique for segmental bone defect nonunions: a review of 25 cases. *Injury*. 2010;41:S72-S77. doi:10.1016/S0020-1383(10)70014-0

13. Obremskey W, Molina C, Collinge C, et al. Current Practice in the Management of Open Fractures Among Orthopaedic Trauma Surgeons. Part B: Management of Segmental Long Bone Defects. A Survey of Orthopaedic Trauma Association Members. *J Orthop Trauma*. 2014;28(8):e203-7. doi:10.1097/BOT.0000000000000034

14. McKibbin B. The biology of fracture healing in long bones. *J Bone Joint Surg Br*. 1978;60-B(2):150-162. http://www.ncbi.nlm.nih.gov/pubmed/350882. Accessed May 10, 2015.

15. Claes L, Recknagel S, Ignatius A. Fracture healing under healthy and inflammatory conditions. *Nat Rev Rheumatol*. 2012;8(3):133-143. doi:10.1038/nrrheum.2012.1

16. Schmidt-Bleek K, Schell H, Schulz N, et al. Inflammatory phase of bone healing initiates the regenerative healing cascade. *Cell Tissue Res*. 2012;347(3):567-573. doi:10.1007/s00441-011-1205-7

17. Kolar P, Gaber T, Perka C, Duda GN, Buttgereit F. Human early fracture hematoma is characterized by inflammation and hypoxia. *Clin Orthop Relat Res*. 2011;469(11):3118-3126. doi:10.1007/s11999-011-1865-3

18. Taguchi K, Ogawa R, Migita M, Hanawa H, Ito H, Orimo H. The role of bone marrow-derived cells in bone fracture repair in a green fluorescent protein chimeric mouse model. *Biochem Biophys Res Commun*. 2005;331(1):31-36. doi:10.1016/j.bbrc.2005.03.119

19. Kon T, Cho TJ, Aizawa T, et al. Expression of osteoprotegerin, receptor activator of NF-kappaB ligand (osteoprotegerin ligand) and related proinflammatory cytokines during fracture healing. *J Bone Miner Res*. 2001;16(6):1004-1014. doi:10.1359/jbmr.2001.16.6.1004

20. Naik AA, Xie C, Zuscik MJ, et al. Reduced COX-2 expression in aged mice is associated with impaired fracture healing. *J Bone Miner Res*. 2009;24(2):251-264. doi:10.1359/jbmr.081002

21. Wang Y, Wan C, Deng L, et al. The hypoxia-inducible factor alpha pathway couples angiogenesis to osteogenesis during skeletal development. *J Clin Invest*. 2007;117(6):1616-1626. doi:10.1172/JCI31581

22. Mizuno K, Mineo K, Tachibana T, Sumi M, Matsubara T, Hirohata K. The osteogenetic potential of fracture haematoma. Subperiosteal and intramuscular transplantation of the haematoma. *J Bone Joint Surg Br*. 1990;72(5):822-829. http://www.ncbi.nlm.nih.gov/pubmed/2211764. Accessed May 10, 2015.

23. Park S-H, Silva M, Bahk W-J, McKellop H, Lieberman JR. Effect of repeated

irrigation and debridement on fracture healing in an animal model. *J Orthop Res*. 2002;20(6):1197-1204. doi:10.1016/S0736-0266(02)00072-4

24. Bhandari M, Tornetta P, Sprague S, et al. Predictors of reoperation following operative management of fractures of the tibial shaft. *J Orthop Trauma*. 2003;17(5):353-361. http://www.ncbi.nlm.nih.gov/pubmed/12759640. Accessed May 10, 2015.

25. Epari DR, Kassi J-P, Schell H, Duda GN. Timely fracture-healing requires optimization of axial fixation stability. *J Bone Joint Surg Am*. 2007;89(7):1575-1585. doi:10.2106/JBJS.F.00247

26. Boerckel JD, Dupont KM, Kolambkar YM, Lin ASP, Guldberg RE. In Vivo Model for Evaluating the Effects of Mechanical Stimulation on Tissue-Engineered Bone Repair. *J Biomech Eng*. 2009;131(8):084502-084502. doi:10.1115/1.3148472

27. Jain RK. Molecular regulation of vessel maturation. *Nat Med*. 2003;9(6):685-693. doi:10.1038/nm0603-685

28. Geudens I, Gerhardt H. Coordinating cell behaviour during blood vessel formation. *Development*. 2011;138(21):4569-4583. doi:10.1242/dev.062323

29. Cursiefen C, Chen L, Borges LP, et al. VEGF-A stimulates lymphangiogenesis and hemangiogenesis in inflammatory neovascularization via macrophage recruitment. *J Clin Invest*. 2004;113(7):1040-1050. doi:10.1172/JCI200420465.1040

30. Adams RH, Alitalo K. Molecular regulation of angiogenesis and lymphangiogenesis. *Nat Rev Mol Cell Biol*. 2007;8(6):464-478. doi:10.1038/nrm2183

31. Korn C, Augustin HG. Mechanisms of Vessel Pruning and Regression. *Dev Cell*. 2015;34(1):5-17. doi:10.1016/j.devcel.2015.06.004

32. van Royen N, Piek JJ, Buschmann I, Hoefer I, Voskuil M, Schaper W. Stimulation of arteriogenesis; a new concept for the treatment of arterial occlusive disease. *Cardiovasc Res*. 2001;49(3):543-553. http://www.ncbi.nlm.nih.gov/pubmed/11166267. Accessed February 2, 2015.

33. Street J, Bao M, deGuzman L, et al. Vascular endothelial growth factor stimulates bone repair by promoting angiogenesis and bone turnover. *Proc Natl Acad Sci U S A*. 2002;99(15):9656-9661. doi:10.1073/pnas.152324099

34. Boerckel JD, Uhrig BA, Willett NJ, Huebsch N, Guldberg RE. Mechanical regulation of vascular growth and tissue regeneration in vivo. *Proc Natl Acad Sci*. 2011;108(37):E674-E680. doi:10.1073/pnas.1107019108

35. Hirao M, Tamai N, Tsumaki N, Yoshikawa H, Myoui A. Oxygen tension regulates chondrocyte differentiation and function during endochondral ossification. *J Biol*

Chem. 2006;281(41):31079-31092. doi:10.1074/jbc.M602296200

36. Wang Y, Wan C, Gilbert SR, Clemens TL. Oxygen sensing and osteogenesis. *Ann N Y Acad Sci*. 2007;1117:1-11. doi:10.1196/annals.1402.049

37. Sheehy EJ, Buckley CT, Kelly DJ. Oxygen tension regulates the osteogenic, chondrogenic and endochondral phenotype of bone marrow derived mesenchymal stem cells. *Biochem Biophys Res Commun*. 2012;417(1):305-310. doi:10.1016/j.bbrc.2011.11.105

38. Hankenson KD, Dishowitz M, Gray C, Schenker M. Angiogenesis in bone regeneration. *Injury*. 2011;42(6):556-561. doi:10.1016/j.injury.2011.03.035

39. Dennis SC, Berkland CJ, Bonewald LF, Detamore MS. Endochondral Ossification for Enhancing Bone Regeneration: Converging Native Extracellular Matrix Biomaterials and Developmental Engineering In Vivo. *Tissue Eng Part B Rev*. October 2014. doi:10.1089/ten.TEB.2014.0419

40. Fiedler J, Leucht F, Waltenberger J, Dehio C, Brenner RE. VEGF-A and PlGF-1 stimulate chemotactic migration of human mesenchymal progenitor cells. *Biochem Biophys Res Commun*. 2005;334(2):561-568. doi:10.1016/j.bbrc.2005.06.116

41. Yang Y-Q, Tan Y-Y, Wong R, Wenden A, Zhang L-K, Rabie ABM. The role of vascular endothelial growth factor in ossification. *Int J Oral Sci*. 2012;4(2):64-68. doi:10.1038/ijos.2012.33

42. Deckers MML, van Bezooijen RL, van der Horst G, et al. Bone morphogenetic proteins stimulate angiogenesis through osteoblast-derived vascular endothelial growth factor A. *Endocrinology*. 2002;143(4):1545-1553. doi:10.1210/endo.143.4.8719

43. Zhang F, Qiu T, Wu X, et al. Sustained BMP signaling in osteoblasts stimulates bone formation by promoting angiogenesis and osteoblast differentiation. *J Bone Miner Res*. 2009;24(7):1224-1233. doi:10.1359/jbmr.090204

44. Malladi P, Xu Y, Chiou M, Giaccia AJ, Longaker MT. Effect of reduced oxygen tension on chondrogenesis and osteogenesis in adipose-derived mesenchymal cells. *Am J Physiol Cell Physiol*. 2006;290(4):C1139-46. doi:10.1152/ajpcell.00415.2005

45. Tuncay OC, Ho D, Barker MK. Oxygen tension regulates osteoblast function. *Am J Orthod Dentofacial Orthop*. 1994;105(5):457-463. doi:10.1016/S0889-5406(94)70006-0

46. Utting JC, Robins SP, Brandao-Burch A, Orriss IR, Behar J, Arnett TR. Hypoxia inhibits the growth, differentiation and bone-forming capacity of rat osteoblasts. *Exp Cell Res*. 2006;312(10):1693-1702. doi:10.1016/j.yexcr.2006.02.007

47. Hausman M., Schaffler M., Majeska R. Prevention of fracture healing in rats by an

inhibitor of angiogenesis. *Bone*. 2001;29(6):560-564. doi:10.1016/S8756-3282(01)00608-1

48. Kanczler JM, Oreffo ROC. Osteogenesis and angiogenesis: the potential for engineering bone. *Eur Cell Mater*. 2008;15:100-114. http://www.ncbi.nlm.nih.gov/pubmed/18454418. Accessed February 2, 2015.

49. Morgan EF, Salisbury Palomares KT, Gleason RE, et al. Correlations between local strains and tissue phenotypes in an experimental model of skeletal healing. *J Biomech*. 2010;43(12):2418-2424. doi:10.1016/j.jbiomech.2010.04.019

50. Claes LE, Claes LE, Heigele C a, et al. Effects of mechanical factors on the fracture healing process. *Clin Orthop Relat Res*. 1998;355S:S132-47. http://www.ncbi.nlm.nih.gov/pubmed/9917634.

51. Shapiro F. Bone development and its relation to fracture repair. The role of mesenchymal osteoblasts and surface osteoblasts. *Eur Cell Mater*. 2008;15:53-76. http://www.ncbi.nlm.nih.gov/pubmed/18382990. Accessed April 7, 2015.

52. Claes L, Blakytny R, Besse J, Bausewein C, Ignatius A, Willie B. Late Dynamization by Reduced Fixation Stiffness Enhances Fracture Healing in a Rat Femoral Osteotomy Model: *J Orthop Trauma*. 2011;25(3):169-174. doi:10.1097/BOT.0b013e3181e3d994

53. Hou T, Li Q, Luo F, et al. Controlled dynamization to enhance reconstruction capacity of tissue-engineered bone in healing critically sized bone defects: an in vivo study in goats. *Tissue Eng Part A*. 2010;16(1):201-212. doi:10.1089/ten.TEA.2009.0291

54. Carpenter RD, Klosterhoff BS, Torstrick FB, et al. Effect of porous orthopaedic implant material and structure on load sharing with simulated bone ingrowth: A finite element analysis comparing titanium and PEEK. *J Mech Behav Biomed Mater*. 2018;80(September 2017):68-76. doi:10.1016/j.jmbbm.2018.01.017

55. Huiskes R, Weinans H, Grootenboer HJ, Dalstra M, Fudala B, Slooff TJ. Adaptive bone-remodeling theory applied to prosthetic-design analysis. *J Biomech*. 1987;20(11-12):1135-1150. http://www.ncbi.nlm.nih.gov/pubmed/3429459. Accessed April 8, 2015.

56. Guilak F, Cohen DM, Estes BT, Gimble JM, Liedtke W, Chen CS. Control of stem cell fate by physical interactions with the extracellular matrix. *Cell Stem Cell*. 2009;5(1):17-26. doi:10.1016/j.stem.2009.06.016

57. McBeath R, Pirone DM, Nelson CM, Bhadriraju K, Chen CS. Cell Shape, Cytoskeletal Tension, and RhoA Regulate Stem Cell Lineage Commitment. *Dev Cell*. 2004;6(4):483-495. doi:10.1016/S1534-5807(04)00075-9

58. Engler AJ, Sen S, Sweeney HL, Discher DE. Matrix elasticity directs stem cell

lineage specification. *Cell*. 2006;126(4):677-689. doi:10.1016/j.cell.2006.06.044

59. Matsumoto T, Yung YC, Fischbach C, Kong HJ, Nakaoka R, Mooney DJ. Mechanical strain regulates endothelial cell patterning in vitro. *Tissue Eng*. 2007;13(1):207-217. doi:10.1089/ten.2006.0058

60. Krishnan L, Underwood CJ, Maas S, et al. Effect of mechanical boundary conditions on orientation of angiogenic microvessels. *Cardiovasc Res*. 2008;78(2):324-332. doi:10.1093/cvr/cvn055

61. Yung YC, Chae J, Buehler MJ, Hunter CP, Mooney DJ. Cyclic tensile strain triggers a sequence of autocrine and paracrine signaling to regulate angiogenic sprouting in human vascular cells. *Proc Natl Acad Sci U S A*. 2009;106(36):15279-15284. doi:10.1073/pnas.0905891106

62. Boerckel JD, Kolambkar YM, Stevens HY, Lin ASP, Dupont KM, Guldberg RE. Effects of in vivo mechanical loading on large bone defect regeneration. *J Orthop Res*. 2012;30(7):1067-1075. doi:10.1002/jor.22042

63. Turner CH, Pavalko FM. Mechanotransduction and functional response of the skeleton to physical stress: The mechanisms and mechanics of bone adaptation. *J Orthop Sci*. 1998;3(6):346-355. doi:10.1007/s007760050064

64. Ingber DE. Cellular mechanotransduction: putting all the pieces together again. *FASEB J*. 2006;20(7):811-827. doi:10.1096/fj.05-5424rev

65. Giancotti FG. Integrin Signaling. *Science (80-)*. 1999;285(5430):1028-1033. doi:10.1126/science.285.5430.1028

66. Lee D-Y, Yeh C-R, Chang S-F, et al. Integrin-mediated expression of bone formation-related genes in osteoblast-like cells in response to fluid shear stress: roles of extracellular matrix, Shc, and mitogen-activated protein kinase. *J Bone Miner Res*. 2008;23(7):1140-1149. doi:10.1359/jbmr.080302

67. Turner CH, Forwood MR, Otter MW. Mechanotransduction in bone: do bone cells act as sensors of fluid flow? *FASEB J*. 1994;8(11):875-878. http://www.ncbi.nlm.nih.gov/pubmed/8070637. Accessed August 15, 2015.

68. Papachristou DJ, Papachroni KK, Basdra EK, Papavassiliou AG. Signaling networks and transcription factors regulating mechanotransduction in bone. *Bioessays*. 2009;31(7):794-804. doi:10.1002/bies.200800223

69. Hynes RO. Integrins: bidirectional, allosteric signaling machines. *Cell*. 2002;110(6):673-687. http://www.ncbi.nlm.nih.gov/pubmed/12297042. Accessed January 14, 2015.

70. Thompson WR, Rubin CT, Rubin J. Mechanical regulation of signaling pathways in bone. *Gene*. 2012;503(2):179-193. doi:10.1016/j.gene.2012.04.076

71. Helmke BP, Rosen AB, Davies PF. Mapping mechanical strain of an endogenous cytoskeletal network in living endothelial cells. *Biophys J*. 2003;84(4):2691-2699. doi:10.1016/S0006-3495(03)75074-7

72. Orr AW, Helmke BP, Blackman BR, Schwartz MA. Mechanisms of mechanotransduction. *Dev Cell*. 2006;10(1):11-20. doi:10.1016/j.devcel.2005.12.006

73. Sokabe M, Sachs F, Jing ZQ. Quantitative video microscopy of patch clamped membranes stress, strain, capacitance, and stretch channel activation. *Biophys J*. 1991;59(3):722-728. doi:10.1016/S0006-3495(91)82285-8

74. Duncan RL, Hruska KA. Chronic, intermittent loading alters mechanosensitive channel characteristics in osteoblast-like cells. *Am J Physiol*. 1994;267(6 Pt 2):F909-16. http://www.ncbi.nlm.nih.gov/pubmed/7528987. Accessed June 30, 2015.

75. Duncan RL, Kizer N, Barry EL, Friedman PA, Hruska KA. Antisense oligodeoxynucleotide inhibition of a swelling-activated cation channel in osteoblast-like osteosarcoma cells. *Proc Natl Acad Sci U S A*. 1996;93(5):1864-1869. http://www.pubmedcentral.nih.gov/articlerender.fcgi?artid=39873&tool=pmcentrez&rendertype=abstract. Accessed August 16, 2015.

76. Lansman JB, Hallam TJ, Rink TJ. Single stretch-activated ion channels in vascular endothelial cells as mechanotransducers? *Nature*. 325(6107):811-813. doi:10.1038/325811a0

77. Kizer N, Guo XL, Hruska K. Reconstitution of stretch-activated cation channels by expression of the alpha-subunit of the epithelial sodium channel cloned from osteoblasts. *Proc Natl Acad Sci U S A*. 1997;94(3):1013-1018. http://www.pubmedcentral.nih.gov/articlerender.fcgi?artid=19631&tool=pmcentrez&rendertype=abstract. Accessed August 16, 2015.

78. Malone AMD, Anderson CT, Tummala P, et al. Primary cilia mediate mechanosensing in bone cells by a calcium-independent mechanism. *Proc Natl Acad Sci U S A*. 2007;104(33):13325-13330. doi:10.1073/pnas.0700636104

79. Temiyasathit S, Tang WJ, Leucht P, et al. Mechanosensing by the primary cilium: deletion of Kif3A reduces bone formation due to loading. *PLoS One*. 2012;7(3):e33368. doi:10.1371/journal.pone.0033368

80. Hoey DA, Tormey S, Ramcharan S, O'Brien FJ, Jacobs CR. Primary cilia-mediated mechanotransduction in human mesenchymal stem cells. *Stem Cells*. 2012;30(11):2561-2570. doi:10.1002/stem.1235

81. McGlashan SR, Jensen CG, Poole CA. Localization of extracellular matrix receptors on the chondrocyte primary cilium. *J Histochem Cytochem*. 2006;54(9):1005-1014. doi:10.1369/jhc.5A6866.2006

82. Iomini C, Tejada K, Mo W, Vaananen H, Piperno G. Primary cilia of human endothelial cells disassemble under laminar shear stress. *J Cell Biol*. 2004;164(6):811-817. doi:10.1083/jcb.200312133

83. Davies PF. Hemodynamic shear stress and the endothelium in cardiovascular pathophysiology. *Nat Clin Pract Cardiovasc Med*. 2009;6(1):16-26. doi:10.1038/ncpcardio1397

84. Ingber DE. Tensegrity I. Cell structure and hierarchical systems biology. *J Cell Sci*. 2003;116(7):1157-1173. doi:10.1242/jcs.00359

85. Vincent LG, Choi YS, Alonso-Latorre B, del Álamo JC, Engler AJ. Mesenchymal stem cell durotaxis depends on substrate stiffness gradient strength. *Biotechnol J*. 2013;8(4):472-484. doi:10.1002/biot.201200205

86. Hadjipanayi E, Mudera V, Brown RA. Close dependence of fibroblast proliferation on collagen scaffold matrix stiffness. *J Tissue Eng Regen Med*. 2009;3(2):77-84. doi:10.1002/term.136

87. Yeh Y-T, Hur SS, Chang J, et al. Matrix stiffness regulates endothelial cell proliferation through septin 9. *PLoS One*. 2012;7(10):e46889. doi:10.1371/journal.pone.0046889

88. Wang H-B, Dembo M, Wang Y-L. Substrate flexibility regulates growth and apoptosis of normal but not transformed cells. *Am J Physiol Cell Physiol*. 2000;279(5):C1345-1350. http://ajpcell.physiology.org/content/279/5/C1345.short. Accessed August 16, 2015.

89. Leight JL, Wozniak MA, Chen S, Lynch ML, Chen CS. Matrix rigidity regulates a switch between TGF-β1-induced apoptosis and epithelial-mesenchymal transition. *Mol Biol Cell*. 2012;23(5):781-791. doi:10.1091/mbc.E11-06-0537

90. Huebsch N, Arany PR, Mao AS, et al. Harnessing traction-mediated manipulation of the cell/matrix interface to control stem-cell fate. *Nat Mater*. 2010;9(6):518-526. doi:10.1038/nmat2732

91. Nelson CM, Jean RP, Tan JL, et al. Emergent patterns of growth controlled by multicellular form and mechanics. *Proc Natl Acad Sci U S A*. 2005;102(33):11594-11599. doi:10.1073/pnas.0502575102

92. Dalby MJ, Gadegaard N, Tare R, et al. The control of human mesenchymal cell differentiation using nanoscale symmetry and disorder. *Nat Mater*. 2007;6(12):997-1003. doi:10.1038/nmat2013

93. Burke DP, Kelly DJ. Substrate stiffness and oxygen as regulators of stem cell differentiation during skeletal tissue regeneration: a mechanobiological model. *PLoS One*. 2012;7(7):e40737. doi:10.1371/journal.pone.0040737

94. Khetan S, Guvendiren M, Legant WR, Cohen DM, Chen CS, Burdick JA. Degradation-mediated cellular traction directs stem cell fate in covalently crosslinked three-dimensional hydrogels. *Nat Mater*. 2013;12(5):458-465. doi:10.1038/nmat3586

95. Sumanasinghe RD, Bernacki SH, Loboa EG. Osteogenic differentiation of human mesenchymal stem cells in collagen matrices: effect of uniaxial cyclic tensile strain on bone morphogenetic protein (BMP-2) mRNA expression. *Tissue Eng*. 2006;12(12):3459-3465. doi:10.1089/ten.2006.12.3459

96. Kearney EM, Farrell E, Prendergast PJ, Campbell VA. Tensile strain as a regulator of mesenchymal stem cell osteogenesis. *Ann Biomed Eng*. 2010;38(5):1767-1779. doi:10.1007/s10439-010-9979-4

97. Simmons CA, Matlis S, Thornton AJ, Chen S, Wang CY, Mooney DJ. Cyclic strain enhances matrix mineralization by adult human mesenchymal stem cells via the extracellular signal-regulated kinase (ERK1/2) signaling pathway. *J Biomech*. 2003;36(8):1087-1096. http://www.ncbi.nlm.nih.gov/pubmed/12831733. Accessed August 23, 2015.

98. Jang J-Y, Lee SW, Park SH, et al. Combined effects of surface morphology and mechanical straining magnitudes on the differentiation of mesenchymal stem cells without using biochemical reagents. *J Biomed Biotechnol*. 2011;2011:860652. doi:10.1155/2011/860652

99. Subramony SD, Dargis BR, Castillo M, et al. The guidance of stem cell differentiation by substrate alignment and mechanical stimulation. *Biomaterials*. 2013;34(8):1942-1953. doi:10.1016/j.biomaterials.2012.11.012

100. Chen Y-J, Huang C-H, Lee I-C, Lee Y-T, Chen M-H, Young T-H. Effects of cyclic mechanical stretching on the mRNA expression of tendon/ligament-related and osteoblast-specific genes in human mesenchymal stem cells. *Connect Tissue Res*. 2008;49(1):7-14. doi:10.1080/03008200701818561

101. Chen Y-J, Huang C-H, Lee I-C, Lee Y-T, Chen M-H, Young T-H. Effects of Cyclic Mechanical Stretching on the mRNA Expression of Tendon/Ligament-Related and Osteoblast-Specific Genes in Human Mesenchymal Stem Cells. *Connect Tissue Res*. May 2015. http://www.tandfonline.com/doi/abs/10.1080/03008200701818561?journalCode=icts20#.VdoPbflViko. Accessed August 23, 2015.

102. Michalopoulos E, Knight RL, Korossis S, Kearney JN, Fisher J, Ingham E. Development of methods for studying the differentiation of human mesenchymal stem cells under cyclic compressive strain. *Tissue Eng Part C Methods*. 2012;18(4):252-262. doi:10.1089/ten.TEC.2011.0347

103. Steward AJ, Kelly DJ. Mechanical regulation of mesenchymal stem cell differentiation. *J Anat*. 2014;(September):n/a-n/a. doi:10.1111/joa.12243

104. Huang C-YC, Hagar KL, Frost LE, Sun Y, Cheung HS. Effects of cyclic compressive loading on chondrogenesis of rabbit bone-marrow derived mesenchymal stem cells. *Stem Cells*. 2004;22(3):313-323. doi:10.1634/stemcells.22-3-313

105. Kisiday JD, Frisbie DD, McIlwraith CW, Grodzinsky AJ. Dynamic compression stimulates proteoglycan synthesis by mesenchymal stem cells in the absence of chondrogenic cytokines. *Tissue Eng Part A*. 2009;15(10):2817-2824. doi:10.1089/ten.TEA.2008.0357

106. Mauck RL, Byers BA, Yuan X, Tuan RS. Regulation of cartilaginous ECM gene transcription by chondrocytes and MSCs in 3D culture in response to dynamic loading. *Biomech Model Mechanobiol*. 2007;6(1-2):113-125. doi:10.1007/s10237-006-0042-1

107. Iqbal J, Zaidi M. Molecular regulation of mechanotransduction. *Biochem Biophys Res Commun*. 2005;328(3):751-755. doi:10.1016/j.bbrc.2004.12.087

108. Pelaez D, Arita N, Cheung HS. Extracellular signal-regulated kinase (ERK) dictates osteogenic and/or chondrogenic lineage commitment of mesenchymal stem cells under dynamic compression. *Biochem Biophys Res Commun*. 2012;417(4):1286-1291. doi:10.1016/j.bbrc.2011.12.131

109. Steward AJ, Wagner DR, Kelly DJ. Exploring the roles of integrin binding and cytoskeletal reorganization during mesenchymal stem cell mechanotransduction in soft and stiff hydrogels subjected to dynamic compression. *J Mech Behav Biomed Mater*. 2014;38:174-182. doi:10.1016/j.jmbbm.2013.07.020

110. Nerem RM. Hemodynamics and the vascular endothelium. *J Biomech Eng*. 1993;115(4B):510-514. http://www.ncbi.nlm.nih.gov/pubmed/8302033. Accessed August 24, 2015.

111. Zheng W, Christensen LP, Tomanek RJ. Stretch induces upregulation of key tyrosine kinase receptors in microvascular endothelial cells. *Am J Physiol Heart Circ Physiol*. 2004;287(6):H2739-45. doi:10.1152/ajpheart.00410.2004

112. Joung IS, Iwamoto MN, Shiu Y-T, Quam CT. Cyclic strain modulates tubulogenesis of endothelial cells in a 3D tissue culture model. *Microvasc Res*. 2006;71(1):1-11. doi:10.1016/j.mvr.2005.10.005

113. Wang JH, Grood ES. The strain magnitude and contact guidance determine orientation response of fibroblasts to cyclic substrate strains. *Connect Tissue Res*. 2000;41(1):29-36. http://www.ncbi.nlm.nih.gov/pubmed/10826706. Accessed August 24, 2015.

114. Meinel L, Karageorgiou V, Fajardo R, et al. Bone Tissue Engineering Using Human Mesenchymal Stem Cells: Effects of Scaffold Material and Medium Flow. *Ann Biomed Eng*. 2004;32(1):112-122. doi:10.1023/B:ABME.0000007796.48329.b4

115. Ando J, Nomura H, Kamiya A. The effect of fluid shear stress on the migration and proliferation of cultured endothelial cells. *Microvasc Res*. 1987;33(1):62-70. doi:10.1016/0026-2862(87)90007-0

116. Li Y-SJ, Haga JH, Chien S. Molecular basis of the effects of shear stress on vascular endothelial cells. *J Biomech*. 2005;38(10):1949-1971. doi:10.1016/j.jbiomech.2004.09.030

117. Gomes ME, Sikavitsas VI, Behravesh E, Reis RL, Mikos AG. Effect of flow perfusion on the osteogenic differentiation of bone marrow stromal cells cultured on starch-based three-dimensional scaffolds. *J Biomed Mater Res A*. 2003;67(1):87-95. doi:10.1002/jbm.a.10075

118. McCoy RJ, O'Brien FJ. Influence of shear stress in perfusion bioreactor cultures for the development of three-dimensional bone tissue constructs: a review. *Tissue Eng Part B Rev*. 2010;16(6):587-601. doi:10.1089/ten.TEB.2010.0370

119. Angele P, Yoo JU, Smith C, et al. Cyclic hydrostatic pressure enhances the chondrogenic phenotype of human mesenchymal progenitor cells differentiated in vitro. *J Orthop Res*. 2003;21(3):451-457. doi:10.1016/S0736-0266(02)00230-9

120. Miyanishi K, Trindade MCD, Lindsey DP, et al. Effects of hydrostatic pressure and transforming growth factor-beta 3 on adult human mesenchymal stem cell chondrogenesis in vitro. *Tissue Eng*. 2006;12(6):1419-1428. doi:10.1089/ten.2006.12.1419

121. Puetzer J, Williams J, Gillies A, Bernacki S, Loboa EG. The effects of cyclic hydrostatic pressure on chondrogenesis and viability of human adipose- and bone marrow-derived mesenchymal stem cells in three-dimensional agarose constructs. *Tissue Eng Part A*. 2013;19(1-2):299-306. doi:10.1089/ten.TEA.2012.0015

122. Wright MO, Stockwell RA, Nuki G. Response of plasma membrane to applied hydrostatic pressure in chondrocytes and fibroblasts. *Connect Tissue Res*. 1992;28(1-2):49-70. http://www.ncbi.nlm.nih.gov/pubmed/1628490. Accessed August 30, 2015.

123. Browning JA, Saunders K, Urban JPG, Wilkins RJ. The influence and interactions of hydrostatic and osmotic pressures on the intracellular milieu of chondrocytes. *Biorheology*. 2004;41(3-4):299-308. http://www.ncbi.nlm.nih.gov/pubmed/15299262. Accessed August 30, 2015.

124. Mizuno S. A novel method for assessing effects of hydrostatic fluid pressure on intracellular calcium: a study with bovine articular chondrocytes. *Am J Physiol Cell Physiol*. 2005;288(2):C329-37. doi:10.1152/ajpcell.00131.2004

125. Hui TH, Zhou ZL, Qian J, Lin Y, Ngan AHW, Gao H. Volumetric deformation of live cells induced by pressure-activated cross-membrane ion transport. *Phys Rev Lett*. 2014;113(11):118101. http://www.ncbi.nlm.nih.gov/pubmed/25260007.

Accessed August 30, 2015.

126. Betts DC, Müller R. Mechanical regulation of bone regeneration: theories, models, and experiments. *Front Endocrinol (Lausanne)*. 2014;5:211. doi:10.3389/fendo.2014.00211

127. Goodship AE, Kenwright J. The influence of induced micromovement upon the healing of experimental tibial fractures. *J Bone Joint Surg Br*. 1985;67(4):650-655. http://www.ncbi.nlm.nih.gov/pubmed/4030869. Accessed September 7, 2015.

128. Goodship AE, Cunningham JL, Kenwright J. Strain rate and timing of stimulation in mechanical modulation of fracture healing. *Clin Orthop Relat Res*. 1998;(355 Suppl):S105-15. http://www.ncbi.nlm.nih.gov/pubmed/9917631. Accessed February 17, 2015.

129. Claes LE, Wilke H-J, Augat P, Rübenacker S, Margevicius KJ. Effect of dynamization on gap healing of diaphyseal fractures under external fixation. *Clin Biomech (Bristol, Avon)*. 1995;10(5):227-234. http://www.ncbi.nlm.nih.gov/pubmed/11415558. Accessed January 20, 2015.

130. Perren SM. Physical and biological aspects of fracture healing with special reference to internal fixation. *Clin Orthop Relat Res*. 1979;(138):175-196. http://www.ncbi.nlm.nih.gov/pubmed/376198. Accessed January 20, 2017.

131. Gardner MJ, van der Meulen MCH, Demetrakopoulos D, Wright TM, Myers ER, Bostrom MP. In vivo cyclic axial compression affects bone healing in the mouse tibia. *J Orthop Res*. 2006;24(8):1679-1686. doi:10.1002/jor.20230

132. Willie BM, Blakytny R, Glöckelmann M, Ignatius A, Claes L. Temporal variation in fixation stiffness affects healing by differential cartilage formation in a rat osteotomy model. *Clin Orthop Relat Res*. 2011;469(11):3094-3101. doi:10.1007/s11999-011-1866-2

133. Glatt V, Miller M, Ivkovic A, et al. Improved healing of large segmental defects in the rat femur by reverse dynamization in the presence of bone morphogenetic protein-2. *J Bone Joint Surg Am*. 2012;94(22):2063-2073. doi:10.2106/JBJS.K.01604

134. Schwarz C, Wulsten D, Ellinghaus A, Lienau J, Willie BM, Duda GN. Mechanical Load Modulates the Stimulatory Effect of BMP2 in a Rat Nonunion Model. *Tissue Eng Part A*. 2013;19(1-2):247-254. doi:10.1089/ten.tea.2012.0265

135. Glatt V, Evans CH, Matthys R. Design, characterisation and in vivo testing of a new, adjustable stiffness, external fixator for the rat femur. *Eur Cell Mater*. 2012;23:289-298; discussion 299. http://www.ncbi.nlm.nih.gov/pubmed/22522283. Accessed January 20, 2015.

136. Hou T, Li Q, Luo F, et al. Controlled dynamization to enhance reconstruction

capacity of tissue-engineered bone in healing critically sized bone defects: an in vivo study in goats. *Tissue Eng Part A*. 2010;16(1):201-212. doi:10.1089/ten.TEA.2009.0291

137. Ilizarov GA. The tension-stress effect on the genesis and growth of tissues: Part II. The influence of the rate and frequency of distraction. *Clin Orthop Relat Res*. 1989;(239):263-285. http://www.ncbi.nlm.nih.gov/pubmed/2912628. Accessed January 12, 2016.

138. Mofid MM, Manson PN, Robertson BC, Tufaro AP, Elias JJ, Vander Kolk CA. Craniofacial Distraction Osteogenesis: A Review of 3278 Cases. *Plast Reconstr Surg*. 2001;108(5):1103-1114. doi:10.1097/00006534-200110000-00001

139. Alzahrani MM, Anam EA, Makhdom AM, Villemure I, Hamdy RC. The effect of altering the mechanical loading environment on the expression of bone regenerating molecules in cases of distraction osteogenesis. *Front Endocrinol (Lausanne)*. 2014;5:214. doi:10.3389/fendo.2014.00214

140. Morgan EF, Hussein AI, Al-Awadhi BA, et al. Vascular development during distraction osteogenesis proceeds by sequential intramuscular arteriogenesis followed by intraosteal angiogenesis. *Bone*. 2012;51(3):535-545. doi:10.1016/j.bone.2012.05.008

141. Matsubara H, Hogan DE, Morgan EF, Mortlock DP, Einhorn TA, Gerstenfeld LC. Vascular tissues are a primary source of BMP2 expression during bone formation induced by distraction osteogenesis. *Bone*. 2012;51(1):168-180. doi:10.1016/j.bone.2012.02.017

142. Natu SS, Ali I, Alam S, Giri KY, Agarwal A, Kulkarni VA. The biology of distraction osteogenesis for correction of mandibular and craniomaxillofacial defects: A review. *Dent Res J (Isfahan)*. 2014;11(1):16-26. http://www.pubmedcentral.nih.gov/articlerender.fcgi?artid=3955310&tool=pmcentrez&rendertype=abstract. Accessed November 25, 2015.

143. Nogueira MP, Paley D, Bhave A, Herbert A, Nocente C, Herzenberg JE. Nerve lesions associated with limb-lengthening. *J Bone Joint Surg Am*. 2003;85-A(8):1502-1510. http://www.ncbi.nlm.nih.gov/pubmed/12925630. Accessed January 12, 2016.

144. Claes L, Augat P, Schorlemmer S, Konrads C, Ignatius A, Ehrnthaller C. Temporary distraction and compression of a diaphyseal osteotomy accelerates bone healing. *J Orthop Res*. 2008;26(6):772-777. doi:10.1002/jor.20588

145. Makhdom AM, Cartaleanu AS, Rendon JS, Villemure I, Hamdy RC. The Accordion Maneuver: A Noninvasive Strategy for Absent or Delayed Callus Formation in Cases of Limb Lengthening. *Adv Orthop*. 2015;2015:912790. doi:10.1155/2015/912790

146. Augat P, Burger J, Schorlemmer S, Henke T, Peraus M, Claes L. Shear movement at the fracture site delays healing in a diaphyseal fracture model. *J Orthop Res*. 2003;21(6):1011-1017. doi:10.1016/S0736-0266(03)00098-6

147. Bishop NE, van Rhijn M, Tami I, Corveleijn R, Schneider E, Ito K. Shear does not necessarily inhibit bone healing. *Clin Orthop Relat Res*. 2006;443:307-314. doi:10.1097/01.blo.0000191272.34786.09

148. Gibney E. The inside story on wearable electronics. *Nature*. 2015;528(7580):26-28. doi:10.1038/528026a

149. McGilvray KC, Unal E, Troyer KL, et al. Implantable microelectromechanical sensors for diagnostic monitoring and post-surgical prediction of bone fracture healing. *J Orthop Res*. 2015;33(10):1439-1446. doi:10.1002/jor.22918

150. Wise KD. Integrated sensors, MEMS, and microsystems: Reflections on a fantastic voyage. *Sensors Actuators, A Phys*. 2007;136(1):39-50. doi:10.1016/j.sna.2007.02.013

151. Wachs RA, Ellstein D, Drazan J, et al. Elementary Implantable Force Sensor: For Smart Orthopaedic Implants. *Adv Biosens Bioelectron*. 2013;2(4). http://www.ncbi.nlm.nih.gov/pubmed/24883335. Accessed January 16, 2017.

152. Boutry CM, Beker L, Kaizawa Y, et al. Biodegradable and flexible arterial-pulse sensor for the wireless monitoring of blood flow. *Nat Biomed Eng*. 2019;3(1):47-57. doi:10.1038/s41551-018-0336-5

153. Nadeau P, El-Damak D, Glettig D, et al. Prolonged energy harvesting for ingestible devices. *Nat Biomed Eng*. 2017;1:0022. doi:10.1038/s41551-016-0022

154. Chew DJ, Zhu L, Delivopoulos E, et al. A Microchannel Neuroprosthesis for Bladder Control After Spinal Cord Injury in Rat. *Sci Transl Med*. 2013;5(210):210ra155-210ra155. doi:10.1126/scitranslmed.3007186

155. Chow EY, Chlebowski AL, Chakraborty S, Chappell WJ, Irazoqui PP. Fully wireless implantable cardiovascular pressure monitor integrated with a medical stent. *IEEE Trans Biomed Eng*. 2010;57(6):1487-1496. doi:10.1109/TBME.2010.2041058

156. Griss P, Enoksson P, Tolvanen-Laakso HK, Meriläinen P, Ollmar S, Stemme G. Micromachined electrodes for biopotential measurements. *J Microelectromechanical Syst*. 2001;10(1):10-16. doi:10.1109/84.911086

157. Cao H, Landge V, Tata U, et al. An implantable, batteryless, and wireless capsule with integrated impedance and pH sensors for gastroesophageal reflux monitoring. *IEEE Trans Biomed Eng*. 2012;59(12 PART2):3131-3139. doi:10.1109/TBME.2012.2214773

158. Troughton RW, Ritzema J, Eigler NL, et al. Direct left atrial pressure monitoring in severe heart failure: Long-term sensor performance. *J Cardiovasc Transl Res*. 2011;4(1):3-13. doi:10.1007/s12265-010-9229-z

159. Totsu K, Haga Y, Esashi M. Vacuum sealed ultra miniature fiber-optic pressure sensor using white light interferometry. *TRANSDUCERS 2003 - 12th Int Conf Solid-State Sensors, Actuators Microsystems, Dig Tech Pap*. 2003;1:931-934. doi:10.1109/SENSOR.2003.1215628

160. Lal A. Integrated pressure and flow sensor in silicon-based ultrasonic surgical actuator. In: *2001 IEEE Ultrasonics Symposium. Proceedings. An International Symposium (Cat. No.01CH37263)*. Vol 2. ; 2001:1373-1376. doi:10.1109/ULTSYM.2001.991976

161. Hong MK, Wong SC, Mintz GS, et al. Can coronary flow parameters after stent placement predict restenosis? *Cathet Cardiovasc Diagn*. 1995;36(3):278-282. doi:10.1002/ccd.1810360321

162. Umbrecht F, Wendlandt M, Juncker D, Hierold C, Neuenschwander J. A wireless implantable passive strain sensor system. In: *Proceedings of IEEE Sensors*. Vol 2005. ; 2005:20-23. doi:10.1109/ICSENS.2005.1597627

163. Mahutte CK. On-line arterial blood gas analysis with optodes: current status. *Clin Biochem*. 1998;31(3):119-130.

164. Kim YT, Kim Y-Y, Jun C-H. Needle-shaped glucose sensor with multi-cell electrode fabricated by surface micromachining. 1999;3680(II):924-930.

165. Mastrototaro JJ, Cooper KW, Soundararajan G, Sanders JB, Shah R V. Clinical experience with an integrated continuous glucose sensor/insulin pump platform: A feasibility study. *Adv Ther*. 2006;23(5):725-732. doi:10.1007/BF02850312

166. Ling Y, Pong T, Vassiliou CC, Huang PL, Cima MJ. Implantable magnetic relaxation sensors measure cumulative exposure to cardiac biomarkers. *Nat Biotechnol*. 2011;29(3):273-277. doi:10.1038/nbt.1780

167. Epari DR, Lienau J, Schell H, Witt F, Duda GN. Pressure, oxygen tension and temperature in the periosteal callus during bone healing--an in vivo study in sheep. *Bone*. 2008;43(4):734-739. doi:10.1016/j.bone.2008.06.007

168. Claes LE, Cunningham JL. Monitoring the mechanical properties of healing bone. *Clin Orthop Relat Res*. 2009;467(8):1964-1971. doi:10.1007/s11999-009-0752-7

169. Szivek JA, Ruth JT, Heden GJ, Martinez MA, Diggins NH, Wenger KH. Determination of joint loads using new sensate scaffolds for regenerating large cartilage defects in the knee. *J Biomed Mater Res Part B Appl Biomater*. 2016:1-13. doi:10.1002/jbm.b.33677

170. Klosterhoff BS, Tsang M, She D, et al. Implantable Sensors for Regenerative Medicine. *J Biomech Eng*. 2017;139(2):020806. doi:10.1115/1.4035436

171. Tarchala M, Harvey EJ, Barralet J. Biomaterial-Stabilized Soft Tissue Healing for Healing of Critical-Sized Bone Defects: the Masquelet Technique. *Adv Healthc Mater*. February 2016. doi:10.1002/adhm.201500793

172. Frost HM. From Wolff's law to the Utah paradigm: Insights about bone physiology and its clinical applications. *Anat Rec*. 2001;262(4):398-419. doi:10.1002/ar.1049

173. Rot C, Stern T, Blecher R, Friesem B, Zelzer E. A Mechanical Jack-like Mechanism Drives Spontaneous Fracture Healing in Neonatal Mice. *Dev Cell*. 2014;31(2):159-170. doi:10.1016/j.devcel.2014.08.026

174. Gerstenfeld LC, Cullinane DM, Barnes GL, Graves DT, Einhorn TA. Fracture healing as a post-natal developmental process: Molecular, spatial, and temporal aspects of its regulation. *J Cell Biochem*. 2003;88(5):873-884. doi:10.1002/jcb.10435

175. Claes L., Heigele C. Magnitudes of local stress and strain along bony surfaces predict the course and type of fracture healing. *J Biomech*. 1999;32(3):255-266. doi:10.1016/S0021-9290(98)00153-5

176. Miller GJ, Gerstenfeld LC, Morgan EF. Mechanical microenvironments and protein expression associated with formation of different skeletal tissues during bone healing. *Biomech Model Mechanobiol*. March 2015. doi:10.1007/s10237-015-0670-4

177. Histing T, Garcia P, Holstein JH, et al. Small animal bone healing models: standards, tips, and pitfalls results of a consensus meeting. *Bone*. 2011;49(4):591-599. doi:10.1016/j.bone.2011.07.007

178. Horner EA, Kirkham J, Wood D, et al. Long bone defect models for tissue engineering applications: criteria for choice. *Tissue Eng Part B Rev*. 2010;16(2):263-271. doi:10.1089/ten.TEB.2009.0224

179. Klosterhoff BS, Nagaraja S, Dedania JJ, Guldberg RE, Willett NJ. Material and Mechanobiological Considerations for Bone Regeneration. In: Bose S, Bandyopadhyay A, eds. *Materials and Devices for Bone Disorders*. 1st ed. Academic Press; 2017:197-264.

180. Wulsten D, Glatt V, Ellinghaus A, et al. Time kinetics of bone defect healing in response to BMP-2 and GDF-5 characterised by in vivo biomechanics. *Eur Cell Mater*. 2011;21:177-192. http://www.ncbi.nlm.nih.gov/pubmed/21312163. Accessed March 22, 2016.

181. Oest ME, Dupont KM, Kong H-J, Mooney DJ, Guldberg RE. Quantitative assessment of scaffold and growth factor-mediated repair of critically sized bone

defects. *J Orthop Res*. 2007;25(7):941-950. doi:10.1002/jor.20372

182. Kolambkar YM, Dupont KM, Boerckel JD, et al. An alginate-based hybrid system for growth factor delivery in the functional repair of large bone defects. *Biomaterials*. 2011;32(1):65-74. doi:10.1016/j.biomaterials.2010.08.074

183. Wehner T, Wolfram U, Henzler T, Niemeyer F, Claes L, Simon U. Internal forces and moments in the femur of the rat during gait. *J Biomech*. 2010;43(13):2473-2479. doi:10.1016/j.jbiomech.2010.05.028

184. Luo M, Martinez AW, Song C, Herrault F, Allen MG. A microfabricated wireless RF pressure sensor made completely of biodegradable materials. *J Microelectromechanical Syst*. 2014;23(1):4-13. doi:10.1109/JMEMS.2013.2290111

185. Oest ME, Dupont KM, Kong H-J, Mooney DJ, Guldberg RE. Quantitative assessment of scaffold and growth factor-mediated repair of critically sized bone defects. *J Orthop Res*. 2007;25(7):941-950. doi:10.1002/jor.20372

186. Bauman JM, Chang Y-H. High-speed X-ray video demonstrates significant skin movement errors with standard optical kinematics during rat locomotion. *J Neurosci Methods*. 2010;186(1):18-24. doi:10.1016/j.jneumeth.2009.10.017

187. Epari DR, Duda GN, Thompson MS. Mechanobiology of bone healing and regeneration: *in vivo* models. *Proc Inst Mech Eng Part H J Eng Med*. 2010;224(12):1543-1553. doi:10.1243/09544119JEIM808

188. Lane SW, Williams DA, Watt FM. Modulating the stem cell niche for tissue regeneration. *Nat Biotechnol*. 2014;32(8):795-803. doi:10.1038/nbt.2978

189. Vining KH, Mooney DJ. Mechanical forces direct stem cell behaviour in development and regeneration. *Nat Rev Mol Cell Biol*. 2017;18(12):728-742. doi:10.1038/nrm.2017.108

190. Pobloth A, Checa S, Razi H, et al. Mechanobiologically optimized 3D titanium-mesh scaffolds enhance bone regeneration in critical segmental defects in sheep. *Sci Transl Med*. 2018;8828(January).

191. Cilla M, Borgiani E, Martínez J, et al. Machine learning techniques for the optimization of joint replacements: Application to a short-stem hip implant. Tsuchiya H, ed. *PLoS One*. 2017;12(9):e0183755. doi:10.1371/journal.pone.0183755

192. Binder EF, Brown M, Steger-may K, Yarasheski KE, Schechtman KB. Effects of Extended Outpatient Rehabilitation After Hip Fracture. *JAMA*. 2004;292(7):837-846.

193. Quarta M, Cromie M, Chacon R, et al. Bioengineered constructs combined with

exercise enhance stem cell-mediated treatment of volumetric muscle loss. *Nat Commun*. 2017;8:1-17. doi:10.1038/ncomms15613

194. Rando TA, Ambrosio F. Forum Regenerative Rehabilitation : Applied Biophysics Meets Stem Cell Therapeutics. *Cell Stem Cell*. 2018;22(3):306-309. doi:10.1016/j.stem.2018.02.003

195. Abraham WT, Stevenson LW, Bourge RC, et al. Sustained efficacy of pulmonary artery pressure to guide adjustment of chronic heart failure therapy: complete follow-up results from the CHAMPION randomised trial. *Lancet*. 2016;387(10017):453-461. doi:10.1016/S0140-6736(15)00723-0

196. Klosterhoff BS, Ong KG, Krishnan L, et al. Wireless implantable sensor for noninvasive, longitudinal quantification of axial strain across rodent long bone defects. *J Biomech Eng*. 2017;139(11). doi:10.1115/1.4037937

197. Kolambkar YM, Bajin M, Wojtowicz A, Hutmacher DW, García AJ, Guldberg RE. Nanofiber orientation and surface functionalization modulate human mesenchymal stem cell behavior in vitro. *Tissue Eng Part A*. 2014;20(1-2):398-409. doi:10.1089/ten.TEA.2012.0426

198. Visser L De, Bos R Van Den. Novel approach to the behavioural characterization of inbred mice : automated home cage observations. *Genes, Brain Behav*. 2006;5:458-466. doi:10.1111/j.1601-183X.2005.00181.x

199. Maas SA, Ellis BJ, Ateshian GA, Weiss JA. FEBio: Finite Elements for Biomechanics. *J Biomech Eng*. 2012;134(1):011005. doi:10.1115/1.4005694

200. Boerckel JD, Kolambkar YM, Dupont KM, et al. Effects of protein dose and delivery system on BMP-mediated bone regeneration. *Biomaterials*. 2011;32(22):5241-5251. doi:10.1016/j.biomaterials.2011.03.063

201. Ozcivici E, Luu YK, Adler B, et al. Mechanical signals as anabolic agents in bone. *Nat Rev Rheumatol*. 2010;6(1):50-59. doi:10.1038/nrrheum.2009.239

202. Rubin CT, Lanyon LE. Regulation of bone mass by mechanical strain magnitude. *Calcif Tissue Int*. 1985;37(4):411-417. doi:10.1007/BF02553711

203. Razi H, Birkhold AI, Weinkamer R, Duda GN, Willie BM, Checa S. Aging Leads to a Dysregulation in Mechanically Driven Bone Formation and Resorption. *J Bone Miner Res*. 2015;30(10):1864-1873. doi:10.1002/jbmr.2528

204. Hoyt BW, Pavey GJ, Pasquina PF, Potter BK. Rehabilitation of Lower Extremity Trauma : a Review of Principles and Military Perspective on Future Directions. *Curr Trauma Reports*. 2015;1(1):50-60. doi:10.1007/s40719-014-0004-5

205. Miglioretti DL, Johnson E, Williams A, et al. The use of computed tomography in pediatrics and the associated radiation exposure and estimated cancer risk. *JAMA*

Pediatr. 2013;167(8):700-707. doi:10.1001/jamapediatrics.2013.311

206. Lin MC, Hu D, Marmor M, Herfat ST, Bahney CS, Maharbiz MM. Smart bone plates can monitor fracture healing. *Sci Rep*. 2019;(August 2018):1-15. doi:10.1038/s41598-018-37784-0

207. Labus KM, Sutherland C, Notaros BM, et al. Direct Electromagnetic Coupling for Non-Invasive Measurements of Stability in Simulated Fracture Healing. *J Orthop Res*. 2019;(August 2018):1-26. doi:10.1002/jor.24275

208. Dalise S, Cavalli L, Ghuman H, et al. Biological effects of dosing aerobic exercise and neuromuscular electrical stimulation in rats. *Sci Rep*. 2017;7:1-13. doi:10.1038/s41598-017-11260-7

209. Sebbag E, Felten R, Sagez F, Sibilia J, Devilliers H, Arnaud L. The world-wide burden of musculoskeletal diseases: a systematic analysis of the World Health Organization Burden of Diseases Database. *Ann Rheum Dis*. 2019:annrheumdis-2019-215142. doi:10.1136/annrheumdis-2019-215142

210. Schwartz AM, Schenker ML, Ahn J, Willett NJ. Building better bone: The weaving of biologic and engineering strategies for managing bone loss. *J Orthop Res*. 2017;35(9):1855-1864. doi:10.1002/jor.23592

211. Rubin CT, Lanyon LE. Regulation of bone formation by applied dynamic loads. *J Bone Jt Surg*. 1984;66(3):397-402. http://jbjs.org/content/66/3/397. Accessed December 15, 2014.

212. Schmidt-Bleek K, Kwee BJ, Mooney DJ, Duda GN. Boon and Bane of Inflammation in Bone Tissue Regeneration and Its Link with Angiogenesis. *Tissue Eng Part B Rev*. 2015;21(4):354-364. doi:10.1089/ten.TEB.2014.0677

213. Ogle ME, Segar CE, Sridhar S, Botchwey EA. Monocytes and macrophages in tissue repair: Implications for immunoregenerative biomaterial design. *Exp Biol Med*. 2016;241(10):1084-1097. doi:10.1177/1535370216650293

214. Alexander KA, Chang MK, Maylin ER, et al. Osteal macrophages promote in vivo intramembranous bone healing in a mouse tibial injury model. *J Bone Miner Res*. 2011;26(7):1517-1532. doi:10.1002/jbmr.354

215. Raggatt LJ, Wullschleger ME, Alexander KA, et al. Fracture Healing via Periosteal Callus Formation Requires Macrophages for Both Initiation and Progression of Early Endochondral Ossi fi cation. *AJPA*. 2014;184(12):3192-3204. doi:10.1016/j.ajpath.2014.08.017

216. Xie H, Cui Z, Wang L, et al. PDGF-BB secreted by preosteoclasts induces CD31hi Emcnhi vessel subtype in coupling osteogenesis. *Nat Med*. 2014;20(11):1270-1278. doi:10.1038/nm.3668.PDGF-BB

217. Champagne CM, Takebe J, Offenbacher S, Cooper LF. Macrophage Cell Lines Produce Osteoinductive Signals That Include Bone Morphogenetic Protein-2. *Bone*. 2002;30(1):26-31.

218. Herbert S, Stainier DYR. Molecular control of endothelial cell behaviour during blood vessel morphogenesis. *Nat Rev Mol Cell Biol*. 2012;12(9):551-564. doi:10.1038/nrm3176.Molecular

219. Owen JL, Mohamadzadeh M. Macrophages and chemokines as mediators of angiogenesis. *Front Physiol*. 2013;4(159):1-8. doi:10.3389/fphys.2013.00159

220. Schlundt C, El Khassawna T, Serra A, et al. Macrophages in bone fracture healing: Their essential role in endochondral ossification. *Bone*. 2018;106:78-89. doi:10.1016/j.bone.2015.10.019

221. Sivaraj KK, Adams RH, Abzhanov A, et al. Blood vessel formation and function in bone. *Development*. 2016;143(15):2706-2715. doi:10.1242/dev.136861

222. Ricard N, Simons M. When It Is Better to Regress : Dynamics of Vascular Pruning. *PLOS Biol*. 2015:1-6. doi:10.1371/journal.pbio.1002148

223. Cristofaro B, Shi Y, Faria M, et al. Dll4-Notch signaling determines the formation of native arterial collateral networks and arterial function in mouse ischemia models. *Development*. 2013;140:1720-1729. doi:10.1242/dev.092304

224. McWhorter FY, Wang T, Nguyen P, Chung T, Liu WF. Modulation of macrophage phenotype by cell shape. *Proc Natl Acad Sci U S A*. 2013;110(43):17253-17258. doi:10.1073/pnas.1308887110

225. Fahy N, Menzel U, Alini M, Stoddart MJ. Shear and Dynamic Compression Modulates the Inflammatory Phenotype of Human Monocytes in vitro. *Front Immunol*. 2019;10(March):1-12. doi:10.3389/fimmu.2019.00383

226. Lienau J, Schmidt-Bleek K, Peters A, et al. Differential regulation of blood vessel formation between standard and delayed bone healing. *J Orthop Res*. 2009;27(9):1133-1140. doi:10.1002/jor.20870

227. Ruehle MA, Li MA, Cheng A, Krishnan L, Willett NJ, Guldberg RE. Decorin-supplemented collagen hydrogels for the co-delivery of bone morphogenetic protein-2 and microvascular fragments to a composite bone-muscle injury model with impaired vascularization. *Acta Biomater*. 2019. doi:10.1016/j.actbio.2019.01.045

228. Duvall CL, Taylor WR, Weiss D, Guldberg RE. Quantitative microcomputed tomography analysis of collateral vessel development after ischemic injury. *Am J Physiol - Hear Circ Physiol*. 2004;287(1):H302-H310. doi:10.1152/ajpheart.00928.2003

229. Badylak SF, Valentin JE, Ravindra AK, McCabe GP, Stewart-Akers AM. Macrophage Phenotype as a Determinant of Biologic Scaffold Remodeling. *Tissue Eng Part A*. 2008;14(11):1835-1842. doi:10.1089/ten.tea.2007.0264

230. Tellier L, Krieger J, Brimeyer A, et al. Localized SDF-1α Delivery Increases Pro-Healing Bone Marrow- Derived Cells in the Supraspinatus Muscle Following Severe Rotator Cuff Injury. *Regen Eng Transl Med*. 2018;4(2). doi:10.1002/cncr.27633.Percutaneous

231. Schlundt C, Schell H, Goodman SB, Vunjak-Novakovic G, Duda GN, Schmidt-Bleek K. Immune modulation as a therapeutic strategy in bone regeneration. *J Exp Orthop*. 2015;2(1):1. doi:10.1186/s40634-014-0017-6

232. Leong PL, Morgan EF. Correlations between indentation modulus and mineral density in bone-fracture calluses. *Integr Comp Biol*. 2009;49(1):59-68. doi:10.1093/icb/icp024

233. Cheng A, Krishnan L, Pradhan P, Weinstock LD, Wood LB. Impaired Bone Healing Following Treatment of Established Nonunion Correlates With Serum Cytokine Expression. *J Orthop Res*. 2019;(February):299-307. doi:10.1002/jor.24186

234. Palomares KTS, Gleason RE, Mason ZD, et al. Mechanical stimulation alters tissue differentiation and molecular expression during bone healing. *J Orthop Res*. 2009;27(9):1123-1132. doi:10.1002/jor.20863

235. McDermott AM, Herberg S, Mason DE, et al. Recapitulating bone development for tissue regeneration through engineered mesenchymal condensations and mechanical cues. *Sci Transl Med*. 2019;11(June). doi:10.1101/157362

236. Lange J, Sapozhnikova A, Lu C, et al. Action of IL-1β during fracture healing. *J Orthop Res*. 2010;28(6):778-784. doi:10.1002/jor.21061

237. Mumme M, Scotti C, Papadimitropoulos A, et al. Interleukin-1β modulates endochondral ossification by human adult bone marrow stromal cells. *Eur Cells Mater*. 2016;24:224-236. doi:10.22203/ecm.v024a16

238. Carmi Y, Voronov E, Dotan S, et al. The Role of Macrophage-Derived IL-1 in Induction and Maintenance of Angiogenesis. *J Immunol*. 2009:4705-4714. doi:10.4049/jimmunol.0901511

239. Honorati MC, Cattini L, Facchini A. IL-17, IL-1β and TNF-α stimulate VEGF production by dedifferentiated chondrocytes. *Osteoarthr Cartil*. 2004;12(9):683-691. doi:10.1016/j.joca.2004.05.009

240. Chen C, Xu ZQ, Zong YP, et al. CXCL5 induces tumor angiogenesis via enhancing the expression of FOXD1 mediated by the AKT/NF-κB pathway in colorectal cancer. *Cell Death Dis*. 2019;10(3). doi:10.1038/s41419-019-1431-6

241. Liu W, Wang P, Xie Z, et al. Abnormal inhibition of osteoclastogenesis by mesenchymal stem cells through the miR-4284/CXCL5 axis in ankylosing spondylitis. *Cell Death Dis*. 2019;10(3). doi:10.1038/s41419-019-1448-x

242. Heilmann A, Schinke T, Bindl R, et al. The Wnt serpentine receptor frizzled-9 regulates new bone formation in fracture healing. *PLoS One*. 2013;8(12):1-10. doi:10.1371/journal.pone.0084232

243. Roca H, Jones JD, Purica MC, et al. Apoptosis-induced CXCL5 accelerates inflammation and growth of prostate tumor metastases in bone. *J Clin Invest*. 2018;128(1):248-266. doi:10.1172/JCI92466

244. Keophiphath M, Rouault C, Divoux A, Clément K, Lacasa D. CCL5 promotes macrophage recruitment and survival in human adipose tissue. *Arterioscler Thromb Vasc Biol*. 2010;30(1):39-45. doi:10.1161/ATVBAHA.109.197442

245. Suffee N, Richard B, Hlawaty H, Oudar O, Charnaux N, Sutton A. Angiogenic properties of the chemokine RANTES/CCL5. *Biochem Soc Trans*. 2011;39(6):1649-1653. doi:10.1042/bst20110651

246. Spiller KJKL, Anfang R, Spiller KJKL, et al. The Role of Macrophage Phenotype in Vascularization of Tissue Engineering Scaffolds. *Biomaterials*. 2014;35(15):4477-4488. doi:10.1016/j.biomaterials.2014.02.012.The

247. Bartneck M, Heffels KH, Pan Y, Bovi M, Zwadlo-Klarwasser G, Groll J. Inducing healing-like human primary macrophage phenotypes by 3D hydrogel coated nanofibres. *Biomaterials*. 2012;33(16):4136-4146. doi:10.1016/j.biomaterials.2012.02.050

248. Gerstenfeld LC, Thiede M, Seibert K, et al. Differential inhibition of fracture healing by non-selective and cyclooxygenase-2 selective non-steroidal anti-inflammatory drugs. *J Orthop Res*. 2003;21(4):670-675. doi:10.1016/S0736-0266(03)00003-2

249. Seide K, Aljudaibi M, Weinrich N, et al. Telemetric assessment of bone healing with an instrumented internal fixator: a preliminary study. *J Bone Joint Surg Br*. 2012;94(3):398-404. doi:10.1302/0301-620X.94B3.27550

250. Egan KR, Muchow RD, Peppler WW, Anderson PA. Theoretical breast cancer induction risk from thoracic spine CT in female pediatric trauma patients. *Pediatrics*. 2012;130(6):e1614-20. doi:10.1542/peds.2012-0272

251. Mulpuru SK, Madhavan M, McLeod CJ, Cha Y-M, Friedman PA. Cardiac Pacemakers : Function , Troubleshooting , and Management. *J Am Coll Cardiol*. 2017;69(2). doi:10.1016/j.jacc.2016.10.061

252. Yacoub MH, Mcleod C. The expanding role of implantable devices to monitor heart failure and pulmonary hypertension. *Nat Rev Cardiol*. 2018;15(December). doi:10.1038/s41569-018-0103-z

253. Hickey BA, Towriss C, Baxter G, et al. Early experience of MAGEC magnetic growing rods in the treatment of early onset scoliosis. *Eur Spine J*. 2014;23(SUPPL. 1):0-4. doi:10.1007/s00586-013-3163-0

254. Kellam JF, Meinberg EG, Agel J, Karam MD, Roberts CS. Fracture and Dislocation Classification Compendium — 2018. *J Orthop Trauma*. 2018;32(1):1-10. doi:10.1097/BOT.0000000000001063

255. Eming SA, Wynn TA, Martin P. Inflammation and metabolism in tissue repair and regeneration. *Science (80-).* 2017;356(6342). http://science.sciencemag.org/content/356/6342/1026.full. Accessed June 21, 2017.

256. Edgar LT, Hoying JB, Weiss JA. In Silico Investigation of Angiogenesis with Growth and Stress Generation Coupled to Local Extracellular Matrix Density. *Ann Biomed Eng*. 2015;43(7):1531-1542. doi:10.1007/s10439-015-1334-3

257. Ho JS, Yeh AJ, Neofytou E, et al. Wireless power transfer to deep-tissue microimplants. *Proc Natl Acad Sci*. 2014;111(22):7974-7979. doi:10.1073/pnas.1403002111

258. Agrawal DR, Tanabe Y, Weng D, et al. Conformal phased surfaces for wireless powering of bioelectronic microdevices. *Nat Biomed Eng*. 2017;1(3):0043. doi:10.1038/s41551-017-0043

259. Krishnan SR, Ray TR, Ayer AB, et al. Epidermal electronics for noninvasive , wireless , quantitative assessment of ventricular shunt function in patients with hydrocephalus. 2018;8437(October).

260. Feiner R, Engel L, Fleischer S, et al. Engineered hybrid cardiac patches with multifunctional electronics for online monitoring and regulation of tissue function. *Nat Mater*. 2016;15:679-686. doi:10.1038/NMAT4590

261. Someya T, Bao Z, Malliaras GG. The rise of plastic bioelectronics. *Nature*. 2016;540(7633):379-385. doi:10.1038/nature21004